Julian Grond

Optimal quantum control of trapped Bose-Einstein condensates

DISSERTATION

zur Erlangung des akademischen Grades
Doktor rerum naturalium (Dr. rer. nat.)
eingereicht an der

Naturwissenschaftlichen Fakultät der
Karl-Franzens-Universität Graz

Betreuer: Ao. Univ.-Prof. Dr. Ulrich Hohenester
Fachbereich Theoretische Physik
Institut für Physik
Karl-Franzens-Universität Graz

Begutachter: Univ.-Prof. Dr. Jörg Schmiedmayer
Atominstitut der Österreichischen Universitäten
Technische Universität Wien

Juni 2010

Abstract

Magnetic microtraps on atom chips enable precise and robust quantum control of Bose-Einstein condensates (BECs). These are macroscopic quantum objects which are very well isolated from the environment. A key application is an atom interferometer built with trapped BECs. The major goal of this thesis is the optimal quantum control of trapped BECs for atom interferometry applications, as well as a better understanding of the involved physical processes.

For control purposes and for non-adiabatic condensate dynamics, elaborate time dependent methods are necessary. We use the *Multi-configurational time-dependent Hartree for Bosons* (MCTDHB) method, which provides a hierarchy of efficient approximation schemes. Realization of atom interferometers will require elaborate control strategies. We implement thus *Optimal control theory* for MCTDHB and apply it to several problems. One application is number squeezing by splitting of BECs, which we achieve one order of magnitude faster as compared to quasi-adiabatic splitting.

The rapid condensate dynamics resulting from our OCT protocols poses the general question about condensate excitations and stability of the condensate during splitting. Simulations with more than two modes allow us to obtain insight into the many-body dynamics.

We analyse trapped BEC interferometers in presence of interactions, in particular the optimal input states and how they can be prepared using quantum control. We find that the MZ interferometer is particularly promising, if Bayesian phase estimation is used. We conclude that phase diffusion is not a substantial limitation for atom interferometry, which could have significant impact on the realization of atom interferometers.

Contents

1 Introduction **3**

2 Atom chips **6**

3 BEC in a double-well **9**
3.1 Exact Hamiltonian . . . 9
3.2 Gross-Pitaevskii equation . . . 10
3.2.1 Elongated condensates and 1D approximation . . . 11
3.2.2 Beyond mean field: Bogoliubov theory . . . 11
3.3 Generic two-mode (*Josephson*) model . . . 12
3.3.1 The MCTDHB method . . . 15

4 Atom interferometry with trapped BECs **18**
4.1 Basic principles . . . 18
4.2 Types of interferometers . . . 19
4.2.1 Time-of-flight (TOF) interferometer . . . 19
4.2.2 Mach-Zehnder (MZ) interferometer . . . 19
4.3 Quantum enhanced metrology . . . 21
4.3.1 Standard quantum limit . . . 21
4.3.2 Exploiting quantum correlations . . . 22
4.4 Phase sensitivity . . . 22
4.4.1 Lower bounds . . . 22
4.4.2 Phase estimation . . . 23
4.4.3 Enhanced phase sensitivity by squeezed states . . . 25

5 Optimal control theory **27**
5.1 Outline of the method . . . 27
5.2 Cost functional . . . 27
5.3 Lagrangian formulation . . . 29
5.4 Gradient: L^2 vs. H^1 formulation . . . 30
5.5 Optimization methods . . . 30
5.6 Line search . . . 31

6 Condensate splitting **32**
6.1 Quasi-adiabatic splitting . . . 32
6.2 Optimized splitting . . . 32
6.2.1 Generic model . . . 32
6.2.2 Optimizing number squeezing within a realistic model . . . 35
6.2.3 Trapping: GP vs MCTDHB . . . 36

7 Stability and fragmentation of non-equilibrium Bose-Einstein condensates 37
7.1 Comparison: GP-orbitals vs. MCTDHB-orbitals 37
7.2 MCTDHB(M) 38
7.2.1 Number squeezing operator 39
7.2.2 Number squeezing results 39
7.2.3 Localization 41
7.3 Consequences for quantum control and two-mode approximations 44
7.3.1 Criteria for breakdown of the two-mode approximation 44
7.3.2 Damping of excitations 44
7.3.3 Choice of the control 44

8 Atom interferometry in presence of interactions 46
8.1 Time-of-flight interferometer 46
8.1.1 Phase diffusion 46
8.1.2 Ideal input states 47
8.1.3 State preparation 49
8.2 Mach-Zehnder interferometer 49
8.2.1 Phase sensitivity 50
8.2.2 Realistic control 53

9 PAPER: Optimizing number squeezing when splitting a mesoscopic condensate: J. Grond, J. Schmiedmayer, and U. Hohenester, Phys. Rev. A 79, 021603(R) (2009). 57

10 PAPER: Optimizing atom interferometry on atom chips: U. Hohenester, J. Grond, and J. Schmiedmayer, In special issue of Fortschr. Phys. 57, 1121 (2009). 58

11 PAPER: Optimal control of number squeezing in trapped Bose-Einstein condensates: J. Grond, G. von Winckel, J. Schmiedmayer, and U. Hohenester, Phys. Rev. A 80, 053625 (2009). 59

12 PAPER: Atom interferometry with trapped Bose-Einstein condensates: impact of atom–atom interactions: J. Grond, U. Hohenester, I. Mazets, and J. Schmiedmayer, New. J. Phys. 12, 065036 (2010). 60

13 Summary and conclusions 61

A Derivation of the MCTDHB equations 68

B Numerical implementation 70
B.1 Time-stepping scheme for MCTDHB(2) 70
B.2 OCT of MCTDHB(2) 72
B.2.1 Gradient 72
B.2.2 Backward equations 72
B.3 Expressions for the involved matrices and vectors 74

Chapter 1

Introduction

The physical notion of *Bose-Einstein condensation* has been proposed by Einstein in 1924/25 [1, 2], soon after the realization of the indistuinguishability of quantum particles going back to Bose [3]. He realized, that in the ground state of a non-interacting gas all bosons must occupy the same state, and thus represent a macroscopic quantum object. Bose-Einstein condensation has been a purely theoretical subject for 70 years, since it occurs below a critical temperature which requires elaborate cooling techniques. Finally it has been experimentally achieved in 1995 [4, 5] when laser cooling, evaporative cooling, and trapping techniques were available. For this achievement the nobel prize has been awarded to E. A. Cornell, W. Ketterle, and C. E. Wieman in 2001.

Nowadays Bose-Einstein condensates (BECs) can be produced also on *atom chips* [6], which are micro fabricated objects of wire structures producing the magnetic and electromagnetic fields necessary for the trapping of neutral atoms. BECs in microtraps experience a very weak coupling to the environment and thus very long coherence times can be achieved. Together with the large degree of control of the external and internal states of neutral atoms, this makes them ideal laboratories for the study of quantum dynamics. For example, it is possible to design cold atom systems to simulate other, e.g., solid state systems.

Another key application of BECs is metrology and sensing [7]. In contrast to photons, atoms are sensitive to gravitational forces and accelerations, and a lot of effort is thus put into building *atom interferometers* for gravitational wave detection. While interferometry with thermal atoms is limited to shot noise sensitivity, this can be overcome by using BECs, and thus a much better sensitivity achieved with the same amount of atoms. *Quantum enhanced metrology* has been demonstrated first by Caves in 1981 [8] who fed an optical Mach-Zehnder interferometer by non classical states of light. Kitagawa and Wineland [9, 10] proposed to use atomic *squeezed* states in order to reduce quantum noise in interferometry up to the fundamental Heisenberg limit. Squeezed states in a double-well BEC have been recently demonstrated experimentally by Estève *et al.* [11]. A more general class of states gives rise to Heisenberg limited interferometry when more sophisticated phase estimation strategies are used, like Bayesian analysis [12]. An important ingredient of a trapped BEC atom interferometer is the coherent splitting of a condensate, which has been first achieved by Schumm *et al.* [13].

The theoretical framework for the description of condensate dynamics is due to Bogoliubov [14], who calculated the (linear) excitation spectrum of this complex many-body system. Time dependent calculations go back to the famous work of Gross and Pitaevskii, who derived a mean field equation [15, 16]. The Gross-Pitaevskii (GP) equation has successfully described many BEC experiments carried out in the last 15 years.

A double-well condensate has many properties similar to a Josephson junction [17], which leads to the very common two-mode Bose Hubbard model [18]. A more elaborate tool for describing *fragmented* condensates is the *Multi-configurational time-dependent Hartree for Bosons*

(MCTDHB) method [19], which relies on a self-consistent calculation of the spatial and the hopping dynamics. It allows for a very accurate description of the condensate dynamics as is required for quantum control purposes. Furthermore, it allows to gain a lot of insight into the many-body dynamics such as condensate excitations, depletion and fragmentation.

The major goal of this thesis is the quantum control and theoretical description of trapped atom interferometers with interacting BECs, as well as the understanding of the involved non-adiabatic condensate dynamics. Designing such interferometers will require elaborate control strategies. A very powerful tool is *Optimal control theory* (OCT) [20, 21]. This is a mathematical framework which allows to determine efficient control schemes even in complex and complicated situations. Most prominent applications can be found in quantum chemistry [22]. Due to the robustness and controllability of BECs in microtraps, it is very promising to apply optimal control in this context [23]. We can separate the work in three major parts.

Optimal control of MCTDHB

Squeezed states can be produced by condensate splitting. Unfortunately, quasi-adiabatic splitting is very ineffcient. Thus we employed optimal control theory to obtain more squeezing at faster time scales. We first showed that this works well within a generic two-mode model. This is however insufficient from the quantum control perspective, since it lacks an experimentally accessible control parameter. We therefore developed and implemented OCT for the more elaborate MCTDH equations. This posed quite some numerical challenges and was supported a lot by a collaboration with Greg von Winckel from the Mathematics department of the University of Graz. In particular, we found that his newly developed optimization approach for quantum systems plays a very important role in the optimization of MCTDHB. The code that we developed can be generally applied to achieve optimal quantum control of BECs trapped in double-well potentials. A very prominent example in this thesis is the splitting of a BEC such that the split condensates are in a highly squeezed state. This allowed to identify two control strategies which achieve number squeezing one order of magnitude faster than quasi-adiabatic splitting. Another example is the cold atom beam splitter, which transforms number into phase information and is an important building block of the Mach-Zehnder interferometer.

Many-body dynamics of splitting of non-equilibrium condensates

The rapid condensate dynamics resulting from our OCT protocols posed the general question about condensate excitations and stability of the condensate during splitting. Work performed in collaboration with A. Scrinzi (formerly Photonics Institute, TU Vienna, now Arnold Sommerfeld Center, LMU Munich) allowed us to obtain insight into the many-body dynamics. He evaluated our splittings ramps using MCTDHB with more than two modes. From this we could identify the role and the connection between condensate oscillations, quantum depletion and fragmentation. This has several consequences on quantum control and on approximation methods for condensate dynamics.

Phase sensitivity of atom interferometers with interacting BECs

In this thesis, we analyzed two types of trapped BEC interferometers in presence of interactions during the whole interferometer sequence: the time-of-flight (TOF) interferometer and the Mach-Zehnder (MZ). This has been an important task, since tuning to zero interactions by Feshbach resonances is not available in most atom chip setups, which constitute otherwise the most versatile tools for external state quantum control and thus ideal candidates for high precision gravitation sensors. For the TOF interferometer, we analyzed the optimal input states and how they can be prepared using quantum control. We then tackled the open problem of the phase sensitivity of a

MZ interferometer in presence of interactions during the interferometer sequence, a work which has been carried out mainly at the INO-CNR BEC center in Trento in the group of A. Smerzi. We found that that it is surprisingly stable against interactions, when using a Bayesian phase estimation strategy. Finally, we demonstrate quantum control of this type of interferometer, including controls which realize the cold atom beam splitter.

Structure of the thesis

In chapter 2 we first give a short introduction into magnetic microtraps on atom chips, and into the magnetic potentials we will use for our calculations . We next introduce in chapter 3 to the theoretical concepts of BEC dynamics, which are particularly relevant for double-well systems. We discuss first properties of the many-body Hamiltonian, then turn to the Gross-Pitaevskii equation, the properties of elongated condensates, Bogoliubov excitation spectra, and in more detail the two-mode model. In this context, we introduce the Bloch sphere visualization of a two-mode N-particle system used throughout this thesis. Finally, we present the general variational framework of MCTDHB. chapter 4 introduces the basic notions of atom interferometry with trapped BECs. After a general discussion we introduce two types of interferometers we deal with in this thesis: the Time-of-flight and Mach-Zehnder interferometers. We then illustrate the concepts of quantum metrology by means of two-level systems. Thereafter we describe theoretical concepts of statistics such as lower bounds to measurement sensitivity and estimators. Finally, these concepts are applied to ideal (non-interacting) atom interferometers, and the use of squeezed states is motivated. The framework of optimal control theory is described in chapter 5. We then turn to condensate splitting. In chapter 6 we first discuss quasi-adiabatic splitting, which gives us the motivation to consider more enhanced splitting protocols. These are devised using OCT and discussed first within a generic two-mode model, where the underlying physical mechanisms can be identified, and then within the more realistic MCTDHB framework. The many-body dynamics of the splitting process is the subject of chapter 7. From simulations of the splitting process using MCTDHB with more than two modes, we determine the contributions to number squeezing due to quantum depletion. Finally, in chapter 8 we turn to the question of interferometry with interacting condensates. We first discuss the optimal input states and the preparation of such for the TOF interferometer. Thereafter we analyse the phase sensitivity of the Mach-Zehnder interferometer.

Chapter 2

Atom chips

We first give an overview over magnetic microtraps on atom chips [6, 24], which are very versatile tools for the manipulation and control of BECs. We then discuss the double-well potentials used for the splitting of a BEC.

Magnetic trapping of neutral atoms is based on the Zeeman Hamiltonian for an external magnetic field $\mathbf{B}$

$$H_Z = -\boldsymbol{\mu} \cdot \mathbf{B}\,, \tag{2.1}$$

where the magnetic moment of the atom is $\boldsymbol{\mu} = -\frac{g_F \mu_B}{\hbar}\mathbf{S}$, where μ_B is the Bohr magneton. The spin $\mathbf{S}$ of the atom is due to hyperfine states, and g_F is the corresponding Landé g-factor, the sign of which distinguishes atomic states which are aligned parallel or anti parallel to $\mathbf{B}$, respectively. In an inhomogeneous magnetic field $\mathbf{B} = \mathbf{B}(\mathbf{r})$, the first ones prefer weak, the others strong fields, respectively (*weak* and *strong field seekers*). The basic mechanisms of trapping are sketched in Fig. 2.1 (a). A current carrying wire produces a magnetic field which loops around this wire. If a static magnetic field is added perpendicular to the wire, the two magnetic fields cancel along a line parallel to the wire. The potential surface for the atoms as sketched in Fig. 2.1 (a) shows up a potential minimum for the atoms along this line, with a force pushing the atoms into the minimum. The distance dependence of the force is proportional to R^{-2}, where R is the distance to the wire. For creating a 3D potential minimum, a more complicated setup has to be used, such as the the *Ioffe-Pritchard trap* [25], where 2D quadrupole fields are used.

The use of current carrying wires [26, 27] has proven to be very promising for miniaturizing magnetic trapping. In fact, by micro fabrication these wire structure can be mounted on an *atom chip* [6], see Fig. 2.1 (b). This allows for very complex surface-mounted structures and a very robust setup with appealing properties concerning dissipation of heat through the substrate. Tightly confining traps can be realized due to comparably high magnetic field gradients [28]. Bose-Einstein condensation has been successfully achieved on atom chips [29, 30, 31]. Nowadays they provide a toolbox for experiments with BECs and allow for a precise control.

Coherent splitting and interference of a condensate on an atom chip has been first achieved by Schumm *et al.* [13]. Best suited for such purposes are *adiabatic dressed state potentials* [32, 33]. Thereby, time dependent magnetic (rf) fields are used instead of static magnetic fields. For the latter, splitting or merging relies on higher multipole components which are weaker than the quadrupole component of a simple trap. Thus, during splitting the condensate experiences weak confinement, which leads to atom losses. This can be avoided by using AC currents. We now sketch how such rf potentials can be obtained. A double well can be realized using a static magnetic field (given in polar coordinates)

$$\mathbf{B}_S(\mathbf{r}) = G\boldsymbol{\rho}[\cos\phi\mathbf{e}_x - \sin\phi\mathbf{e}_y] + B_I\mathbf{e}_z\,, \tag{2.2}$$

where G is the gradient of the quadrupole field. B_I is related to the inhomogeneous Ioffe field

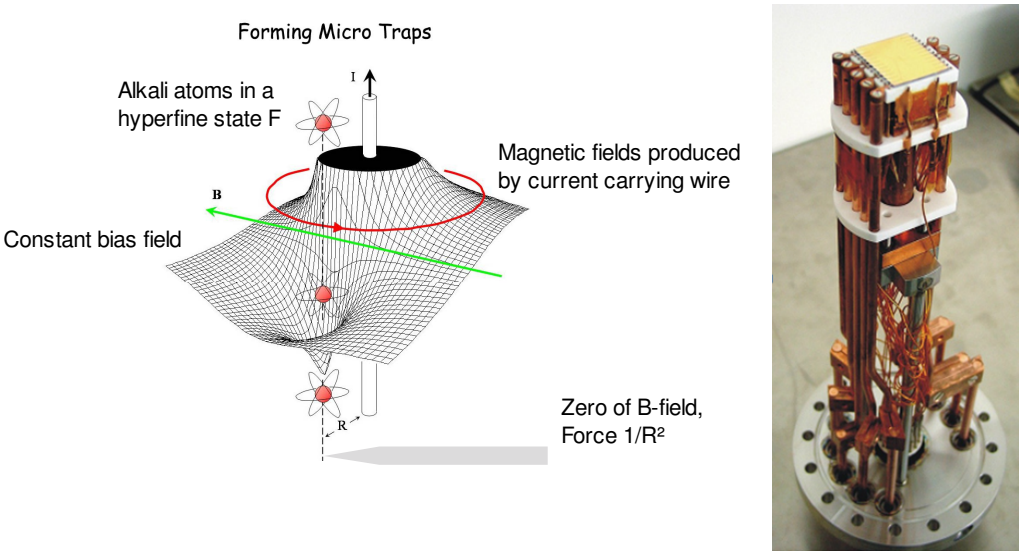

(a) (b)

Figure 2.1: (a) A simple example of magnetic trapping (from Schmiedmayer and Hinds). A potential minimum along a line can be achieved by a current carrying wire and perpendicular static magnetic fields. (b) Atom chip from the Schmiedmayer group. Current carrying wires mounted on the chip give rise to magnetic trapping potentials.

strength. The time-dependent field reads

$$\mathbf{B}_O(\mathbf{r},t) = B_{rf}\mathbf{e}_x \cos(\omega t)\,. \tag{2.3}$$

One next transforms the Zeeman Hamiltonian Eq. (2.1) to a time-independent frame of reference. In addition, a rotating wave approximation is used.[1] It results in a time-independent Hamiltonian, whose eigenvalues are the adiabatic potentials (along x)

$$V_\lambda(x) = m'_F g_F \mu_B \sqrt{\left[|\mathbf{B}_S(x)| - \frac{\hbar\omega}{g_F\mu_B}\right]^2 + \left[\frac{B_{rf}B_I}{2|\mathbf{B}_S(x)|}\right]^2}\,, \tag{2.4}$$

for the different hyperfine sub levels m'_F.

A typical experimental setup is sketched in Fig. 2.2 (a). The control parameter which determines the splitting is the rf-amplitude. It is convenient to introduce a control parameter λ with $B_{rf} = 0.5 + 0.3\lambda$ G. For increasing λ, a single well is continuously transformed into a double well, see Fig. 2.2 (b). This is the splitting scenario which will be used in this thesis, with $\omega_\perp = 2\pi \cdot 2$ kHz transverse confinement.

[1] We note that potentials of current experiments have to be calculated beyond this approximation [33].

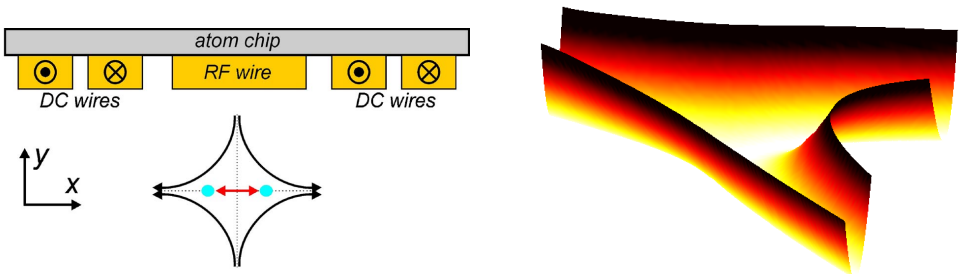

(a) (b)

Figure 2.2: (a) Experimental setup for adiabatic radio-frequency potentials, from [32]. DC and AC wires are mounted on a chip. Splitting of the trapped BEC is effected in the x-direction. (b) By changing the rf amplitude, a single well is continuously transformed into a double-well.

Chapter 3

BEC in a double-well

In this chapter the theoretical models of the dynamical condensate description [34, 35, 36], which are used throughout this thesis, are discussed. We start with a discussion of the exact Hamiltonian in Sec. 3.1, which is numerically intractable, but forms the starting point for approximation schemes. In this context, we introduce *reduced densities*, which are important for the definition of BEC and fragmentation, and are very important in this work. Next, the famous GP-equation is reviewed in Sec. 3.2, which provides a mean-field description of the condensate. We discuss the notion of elongated condensates and the physics of condensate excitations. Since we aim at condensate splitting, we need at least two modes. A simple two-mode model is discussed in Sec. 3.3, which contains a lot of the physics of condensate splitting. The visualization on the Bloch sphere will be introduced. In Sec. 3.3.1, we finally present a variational framework which provides a hierarchy of approximations: the *Multi-configurational time-dependent Hartree for Bosons* (MCTDHB) method allows to take into account the full spatial dynamics of a fragmented condensate. We specialize to the important case of two modes.

3.1 Exact Hamiltonian

We consider Bosons in a trapping potential at zero temperature. Typically, s-wave scattering dominates [34, 35], and thus we have a contact potential between the atoms $U_0^{3D}\delta(\mathbf{r}-\mathbf{r}')$. The condensate atoms are described by the many-body Schrödinger equation for N bosons, which reads

$$i\frac{\partial\Psi(\mathbf{r}_1,...,\mathbf{r}_N;t)}{\partial t}=\hat{H}(t)\Psi(\mathbf{r}_1,...,\mathbf{r}_N;t),\qquad \hat{H}(\mathbf{r}_1,...,\mathbf{r}_N;t)=\sum_{i=1}^{N}\hat{h}(\mathbf{r}_i,t)+U_0^{3D}\sum_{k<q}\delta(\mathbf{r}_k-\mathbf{r}_q)\ , \tag{3.1}$$

where $\Psi(\mathbf{r}_1,...,\mathbf{r}_N;t)$ is the many-boson wave function. Hereby, $\hat{h}(\mathbf{r},t)=-\frac{\hbar}{2m}\vec{\nabla}^2+V_\lambda(\mathbf{r})$ is the *bare* Hamiltonian which contains the confinement potential. m is the mass of ^{87}Rb. U_0^{3D} is an interaction parameter, which contains the s-wave scattering length $a_s=5.3\,\mathring{A}$ as $U_0^{3D}=\frac{4\pi\hbar^2a_s}{m}$.

Important quantities which we will need in the following are the r-particle reduced densities [37]

$$\rho^{(p)}(x_1,..,x_p|x_1',...,x_p';t)= \tag{3.2}$$
$$\frac{N!}{(N-p)!}\int\Psi(x_1,...,x_p,x_{p+1},...,x_N;t)\Psi^*(x_1',...,x_p',x_{p+1},...,x_N;t)dx_{p+1}...dx_N\ ,$$

the diagonals of which are proportional to the r-particle probability distributions. The one-body density is given by

$$\rho(\mathbf{r}|\mathbf{r}';t)=\langle\Psi(t)|\hat{\Psi}^\dagger(\mathbf{r}')\hat{\Psi}(\mathbf{r})|\Psi(t)\rangle\ . \tag{3.3}$$

In terms of eigenfunctions and eigenvalues

$$\rho(\mathbf{r}|\mathbf{r}';t) = \sum_i n_i(t)\phi_i^*(\mathbf{r}';t)\phi_i(\mathbf{r};t) \;, \tag{3.4}$$

we talk about *natural orbitals* ϕ_i and *natural occupations* n_i. According to the definition of Penrose and Onsager [38], we have *simple* BEC, if one eigenvalue is macroscopic [$\mathcal{O}(N)$], and *fragmented* BEC, if several eigenvalues are macroscopic. The intermediate case of small population of several orbitals is usually referred to as condensate *depletion*.

In the following we will use units where the mass is given in terms of the Rubidium mass, and $\hbar = 1$. We scale length and time according to an harmonic oscillator with confinement length $a_{ho} = \sqrt{\hbar/(m\omega_{ho})} = 1\ \mu m$. It follows that time is measured in units of $1/\omega_{ho} = 1.37$ ms and energy in units of $\hbar\omega_{ho} = 2\pi \cdot 116.26$ Hz. Magnetic fields are given in G.

Eq. (3.1) represents in practice a numerically intractable problem, since the Hilbert space for the state grows exponentially with N and we consider typically $N = 100 - 1000$ atoms. Therefore, we proceed with approximations.

3.2 Gross-Pitaevskii equation

For weakly interacting gases a *mean field* theory is a good description of the condensate. It is valid if on average there is less than one atom in a volume defined by the s-wave the scattering length $na_s^3 \ll 1$, where n is the atomic density [34]. For this purpose, we first rewrite the many-boson Hamiltonian Eq. (3.1) in second quantization

$$\hat{H}(t) = \int \left[\hat{\Psi}^\dagger(\mathbf{r})\hat{h}(\mathbf{r},t)\hat{\Psi}(\mathbf{r}) + \frac{U_0^{3D}}{2}\hat{\Psi}^\dagger(\mathbf{r})\hat{\Psi}^\dagger(\mathbf{r})\hat{\Psi}(\mathbf{r})\hat{\Psi}(\mathbf{r})\right] dx \,. \tag{3.5}$$

with the bosonic creation and annihilation operators $\hat{\Psi}(\mathbf{r})$ and $\hat{\Psi}^\dagger(\mathbf{r})$, respectively. The equation of motion for the field operator reads

$$i\hbar\frac{\partial}{\partial t}\hat{\Psi}(\mathbf{r},t) = [\hat{\Psi}, \hat{H}] = \left[\hat{h}(\mathbf{r},t) + U_0^{3D}\hat{\Psi}^\dagger(\mathbf{r},t)\hat{\Psi}(\mathbf{r},t)\right]\hat{\Psi}(\mathbf{r},t) \tag{3.6}$$

According to Bogoliubov, we decompose the wave function in a condensate and a non-condensate fraction, or *depletion* [14]

$$\hat{\Psi}(\mathbf{r},t) = \Phi(\mathbf{r},t)\hat{a} + \hat{\Psi}'(\mathbf{r},t). \tag{3.7}$$

$\Phi(\mathbf{r},t) = \langle\hat{\Psi}(\mathbf{r},t)\rangle$ is defined as the expectation value of the field operator in a reservoir of atoms, and $\hat{a}$ ($\hat{a}^\dagger$) creates (annihilates) a condensate atom. Therefore, since $\hat{\Psi}'(\mathbf{r},t)$ is considered as a small perturbation, $n_0(\mathbf{r}) = |\Phi(\mathbf{r},t)|^2$ describes the condensate density. We now replace in Eq. (3.6) $\Psi(\mathbf{r},t) \to \Phi(\mathbf{r},t)$, which is a good approximation for s-wave scattering. We then obtain the famous time-dependent *Gross-Pitaevskii* (GP) equation

$$i\dot{\Phi}(\mathbf{r},t) = \left(\hat{h}(\mathbf{r},t) + U_0^{3D}(N-1)|\Phi(\mathbf{r},t)|^2\right)\Phi(\mathbf{r},t) \;. \tag{3.8}$$

It contains a potential proportional to the density $n_0(\mathbf{r})$, and reduces to the one-body Schrödinger equation for $U_0^{3D} \to 0$. The normalization of the GP-wave function is $\int d\mathbf{r}|\Phi(\mathbf{r},t)|^2 = 1$. We obtain the time-independent GP-equation when making the ansatz $\Phi(\mathbf{r},t) = \phi(\mathbf{r})exp\big(-i\mu t/\hbar\big)$:

$$\left(\hat{h}(\mathbf{r}) + U_0^{3D}(N-1)|\phi(\mathbf{r})|^2\right)\phi(\mathbf{r}) = \mu\phi(\mathbf{r}) \;. \tag{3.9}$$

μ is the chemical potential, since it corresponds to the energy per particle. Repulsive interactions lead to broader ground state wave functions compared to the non-interacting case. A derivation of the GP by a variational principle will be discussed in Sec. 3.3.1 in context of a general variational framework.

3.2.1 Elongated condensates and 1D approximation

We consider cigar-shaped potentials which result in elongated condensates. If the aspect ratio $C_{1D} = \omega_\parallel/\omega_\perp$ is very small and the chemical potential much smaller than the transverse confinement $\mu \ll \omega_\perp$ [39], the transverse condensate dynamics becomes frozen out. This means that one can safely assume that in the transversal directions only the single-particle ground state is occupied. The physics governing such a system is then effectively one-dimensional (1D), and the longitudinal direction completely decouples from the transversal ones. This has a lot of consequences on the statistical properties as well as on the validity of mean field approximations. The systems considered in this work have not a 1D character, although they are very elongated, because they are in a crossover regime $\mu \sim \omega_\perp$. The weakly interacting regime in 1D is characterized by [39]

$$\gamma = \frac{mg}{\hbar^2 n^2}\,, \quad \text{with} \quad g = 2\hbar\omega_\perp a_s\,. \tag{3.10}$$

g is the 1D interaction strength [40] and γ determines the distance scale of the interactions, compared to their mean separation. For the parameters we consider, both the diluteness parameter $na_s^3 \ll 1$, as well as $\gamma \ll 1$. From this we conclude that a 3D mean-field description of the condensate is reasonable in our case.

We are interested in splitting condensates along one transverse direction x. Hence, the condensate dynamics is predominantly in that direction. Furthermore, the dynamics in the longitudinal direction is much slower than in the splitting direction. We assume to have a potential given by $V(\mathbf{r}) = V_x(x) + V_y(y) + V_z(z)$. This has the consequence that V_y and V_z stay constant, when V_x is modified. For a non-interacting problem, a 1D Schrödinger equation is sufficient to describe the dynamics, because the wave function can be written as $\phi(\mathbf{r}) = \phi_x(x)\phi_y(y)\phi_z(z)$ [41]. For the interacting system, this holds at least for the ground state of the GP-equation. In particular, we insert $V(\mathbf{r})$ and $\phi(\mathbf{r})$ into the time-independent GP Eq. (3.9) and integrate out two spatial degrees of freedom. From this we obtain three coupled equations, where the effective 1D interaction parameter U_0 is obtained as

$$U_0 = U_0^{3D} \int dy |\phi_y|^4 \int dz |\phi_z|^4\,. \tag{3.11}$$

For a time-dependent potential, the decoupling is not strictly valid anymore, since the interactions in principle couple all 3 directions. However, to a good approximation we can consider an effective 1D problem with interaction strength U_0, and assume that the main physics is captured by a 1D model. This approximation has certainly its limits and and will slightly perturbe the results obtained from the 1D approach. In a future work, we will perform full 3D calculations.

3.2.2 Beyond mean field: Bogoliubov theory

By linearizing the GP equation, the excitation spectrum of a BEC can be obtained [15]. We insert a wave function of the form

$$\Phi(\mathbf{r}, t) = e^{-i\mu t/\hbar}[\phi(\mathbf{r}) + u(\mathbf{r})e^{-i\omega t} + v^*(\mathbf{r})e^{i\omega t}]\,, \tag{3.12}$$

into Eq. (3.9) and retain terms which are linear in u and v. Two coupled equations result

$$\hbar\omega(\mathbf{r}) = [\hat{h}(\mathbf{r}) - \mu + 2g\phi^2(\mathbf{r})]u(\mathbf{r}) + g\phi^2(\mathbf{r})v(\mathbf{r})\,, \tag{3.13}$$

$$-\hbar\omega v(\mathbf{r}) = [\hat{h}(\mathbf{r}) - \mu + 2g\phi^2(\mathbf{r})]v(\mathbf{r}) + g\phi^2(\mathbf{r})u(\mathbf{r})\,, \tag{3.14}$$

where $\varepsilon = \hbar\omega$ corresponds to the energy of the excitations. u and v correspond to quasi-particle amplitudes. The non-condensed part of the wave function Eq. (3.7) can be expressed in terms of

them:

$$\hat{\Psi}'(\mathbf{r},t) = \sum_j [u_j(\mathbf{r})\alpha_j(t) + v_j^*(\mathbf{r})\alpha_j^\dagger(t)]\,, \tag{3.15}$$

where α_j and $\alpha_j^\dagger$ are quasi-particle annihilation and creation operators. For a uniform gas one obtains the dispersion relation

$$(\hbar\omega)^2 = \Big(\frac{\hbar^2 q^2}{2m}\Big)\Big(\frac{\hbar^2 q^2}{2m} + 2gn_0\Big)\,, \tag{3.16}$$

which is the famous Bogoliubov form [14]. From this we see that for small momenta $\mathbf{q}$ the excitation spectrum is phononlike and has single particle character for large momenta. Similarly, when analysing the amplitudes u and v, in the long wave length limit we obtain $u \sim v$ and the excitations are *collective*. For small wavelength v dominates and the excitations correspond to single atoms removed from the condensate. In fact, one can show that the number of particles out of the condensate (depletion) is given by $n_{out}(\mathbf{r}) = \sum_j |v_j(\mathbf{r})|^2$ [42]. Alternatively, these two types of excitations are referred to as *coherent* and *incoherent*.

3.3 Generic two-mode (*Josephson*) model

When considering a double-well potential, even for dilute condensates, the assumption of a single mode is fundamentally wrong in general. For example, the ground state of a double-well with very high barrier is two-fold fragmented. A simple description of two-mode physics is given in this section [18, 43]. From now on we consider 1D dynamics, as has been motivated in Sec. 3.2.1. We restrict the field operator to a *left* and a *right* mode

$$\hat{\Psi}(\mathbf{r}) = \hat{a}_L\phi_L(\mathbf{r}) + \hat{a}_R\phi_R(\mathbf{r})\,. \tag{3.17}$$

When inserted into the many-body Hamiltonian Eq. (3.5) we get

$$\hat{H} = -\frac{\Omega(t)}{2}\big(\hat{a}_L^\dagger\hat{a}_R + \hat{a}_L\hat{a}_R^\dagger\big) + \kappa\big(\hat{a}_L^\dagger\hat{a}_L^\dagger\hat{a}_L\hat{a}_L + \hat{a}_R^\dagger\hat{a}_R^\dagger\hat{a}_R\hat{a}_R\big)\,, \tag{3.18}$$

where terms proportional to the total particle number $\hat{N} = \hat{a}_L^\dagger\hat{a}_L + \hat{a}_R^\dagger\hat{a}_R$ have been neglected since they do not contribute to the dynamics. We label the basis states as $k \equiv |N/2+k\rangle_L|N/2-l\rangle_R$, such that k is the relative atom number between left and right wells. The Hamiltonian acts on a state vector $\mathbf{C}$, with the wave function given by $|\Psi(t)\rangle = \sum_{k=-N/2}^{N/2} C_k|k\rangle$. The first term in Eq. (3.18) accounts for hopping of the atoms between the left and the right well, whereas the second term penalizes an atom number imbalance. The corresponding parameters are the *tunnel coupling*

$$\Omega = -\int dx\phi_L^*(x)\hat{h}(x)\phi_R(x) + \text{h.c.}\,, \tag{3.19}$$

and the nonlinear interaction, or *charging energy*

$$\kappa = \frac{U_0}{2}\int dx|\phi_{L,R}(x)|^4\,. \tag{3.20}$$

We did not specify the shape of the orbitals $\phi_L(x)$ and $\phi_R(x)$. Instead, we take Ω as a generic parameter which characterizes the splitting, and choose a constant κ (typically, we have $\kappa = U_0/2$ [41]).

We proceed to study the ground states of this Hamiltonian. $\Omega \gg \kappa$ corresponds to the case of an unsplit trap, where tunneling dominates over the nonlinear interactions. We rewrite Eq. (3.18) in this case in terms of *gerade* and *ungerade* orbitals $\phi_{g,e} = (\phi_L \pm \phi_R)/\sqrt{2}$

$$\hat{H} = \frac{\Omega(t)}{2}(\hat{a}_e^\dagger\hat{a}_e - \hat{a}_g^\dagger\hat{a}_g)\,, \tag{3.21}$$

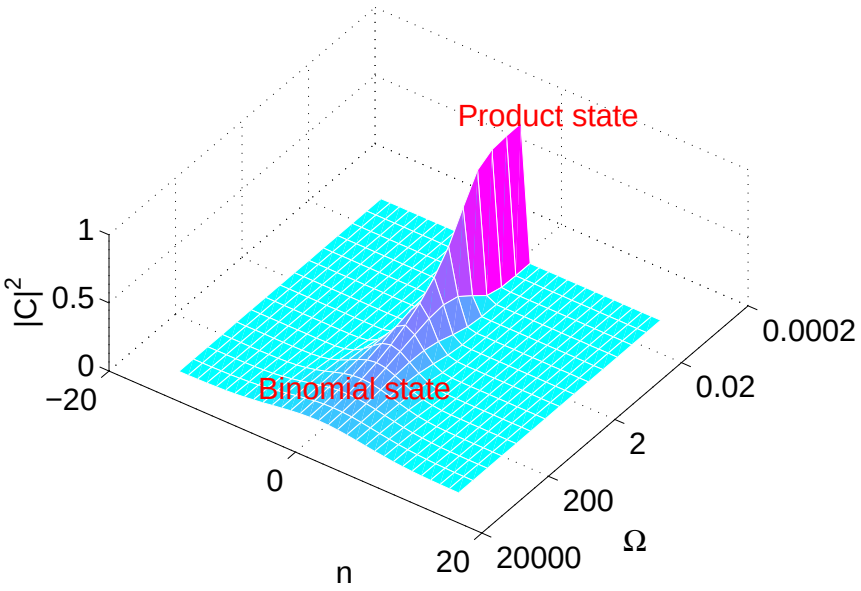

Figure 3.1: Transition from delocalized to localized number states in the generic model. The two-mode probability distribution $|\mathbf{C}|^2$ is plotted versus relative atom number n and the tunnel coupling Ω.

where $\hat{a}_g$ ($\hat{a}_g^\dagger$) and $\hat{a}_e$ ($\hat{a}_e^\dagger$) are the corresponding annihilation (creation) operators. Since Eq. (3.21) is diagonal in in this basis, we immediately see that the ground state is given by

$$|\Psi_0\rangle = \frac{1}{\sqrt{N!}}(a_g^\dagger)^N|0\rangle = \frac{1}{\sqrt{N!}}\left(\frac{\hat{a}_L^\dagger + \hat{a}_R^\dagger}{\sqrt{2}}\right)^N|0\rangle = \frac{1}{2^{N/2}}\sum_{k=-N/2}^{N/2}\sqrt{\binom{N}{N/2+k}}|k\rangle\,. \tag{3.22}$$

This state has binomial number fluctuations $\Delta n := \sqrt{\langle \hat{J}_z^2\rangle} = \sqrt{N}/2$, and thus the atoms are delocalized over the two wells. When $\kappa \gg \Omega$, the ground state is simply $|N/2\rangle_L|N/2\rangle_R$, since interactions penalize atom number fluctuations. The transition between those two extreme cases is shown in Fig. 3.1. The intermediate states are referred to as *number squeezed* states, since $\Delta n < \sqrt{N}/2$.

In the transition the system undergoes the following regimes, which characterize the physical behaviour [35]: In the **Rabi** regime ($\Omega/\kappa \gg N$), we have strong tunneling and interactions are negligible, in the **Josephson** regime ($1/N \ll \Omega/\kappa \ll N$) there is a competition between tunneling and interactions (Josephson physics [17]) , and finally in the **Fock** regime ($\Omega/\kappa \ll 1/N$) interactions dominate over tunneling and the atoms are localized in the wells.

It is very comfortable to rewrite Eq. (3.18) in terms of pseudospin operators [18]. Since we deal with N atoms which are allowed to occupy two states, we treat it as spin $N/2$-system. The operators read

$$\hat{J}_x = \frac{1}{2}(\hat{a}_L^\dagger\hat{a}_R + \hat{a}_R^\dagger\hat{a}_L), \quad \hat{J}_y = \frac{i}{2}(\hat{a}_L^\dagger\hat{a}_R - \hat{a}_R^\dagger\hat{a}_L), \quad \hat{J}_z = \frac{1}{2}(\hat{a}_L^\dagger\hat{a}_L - \hat{a}_R^\dagger\hat{a}_R)\,. \tag{3.23}$$

$\hat{J}_x$ exchanges one atom between left and right well, and $\hat{J}_z$ measures the atom number imbalance. We get

$$\hat{H} = -\Omega(t)\hat{J}_x + 2\kappa\hat{J}_z^2\,. \tag{3.24}$$

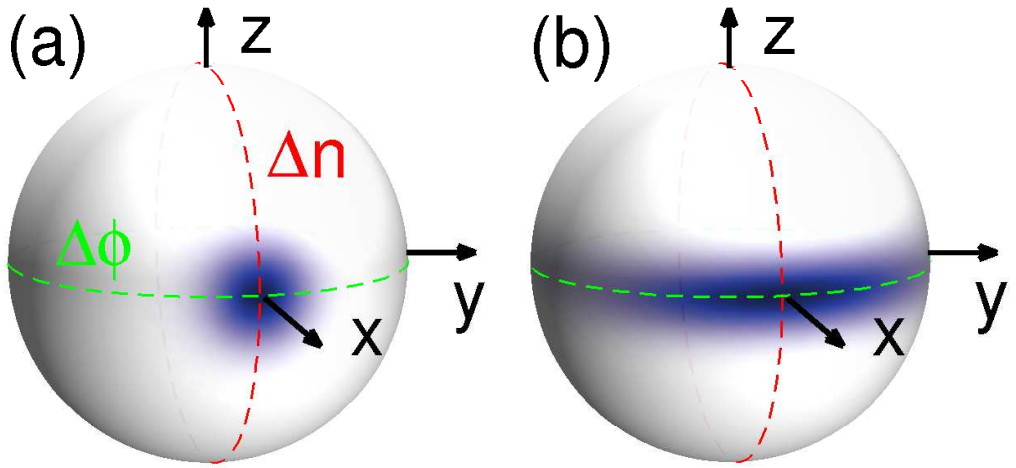

Figure 3.2: Bloch sphere of (a) a binomial, and (b) a number squeezed state. Number difference is plotted on the z-axis, the phase on the equator. Number fluctuations Δn and phase fluctuations $\Delta\phi$ are visualized by the width in z and y directions, respectively.

A phase representation can be obtained by Fourier transforming the atom number vector $\mathbf{C}$ [44]:

$$\Phi(\phi) = \frac{1}{\sqrt{2\pi}} \sum_{k=-N/2}^{N/2} C_k e^{ik\phi} \,, \tag{3.25}$$

where the phase eigenstates read $\langle\phi|k\rangle = e^{ik\phi}$. The phase operator $\hat{\phi}$ is the conjugate variable to $\hat{J}_z$ with $[\hat{\phi}, \hat{J}_z] = i$. We can calculate the mean and variance of $\hat{\phi}$ from this continuous phase representation

$$\langle\hat{\phi}\rangle = \int_{-\pi}^{\pi} d\phi\, \phi |\Phi(\phi)|^2 \,, \quad \Delta\phi^2 = \int_{-\pi}^{\pi} d\phi\, \phi^2 |\Phi(\phi)|^2 - \langle\hat{\phi}\rangle^2 \,. \tag{3.26}$$

For $\langle\hat{\phi}\rangle = 0$, the phase width $\Delta\phi$ is proportional to the width of $\hat{J}_y$, ΔJ_y.

Visualization on the Bloch sphere

A very helpful visualization of these pseudospin states can be achieved on the Bloch sphere [45]. This works as follows: An over-complete basis for the states of the $N/2$-spin system is provided by the *atomic coherent states* which can be obtained by rotations of the state where all atoms are in one well, $|-N/2\rangle$, as:

$$|\theta, \phi\rangle = R_{\theta,\phi}|-N/2\rangle \,. \tag{3.27}$$

The rotation matrix is given as $R_{\theta,\phi} = e^{-i\theta(\hat{J}_x \sin\phi - \hat{J}_y \cos\phi)}$. In this way a probability distribution for a given state vector $|\mathbf{C}\rangle$ can be obtained as

$$C(\theta, \phi) = |\langle\theta, \phi|\mathbf{C}\rangle|^2 \,. \tag{3.28}$$

For instance, if $|\mathbf{C}\rangle$ is a coherent state with zero phase, it has a distribution with respect to ϕ like

$$|\langle\pi/2, \phi|\pi/2, 0\rangle|^2 = \left(\frac{3 + \cos(\phi)}{4}\right)^N \,, \tag{3.29}$$

which corresponds approximately to a Gaussian. In Fig. 3.2 we show examples where $C(\theta, \phi)$ is plotted on a sphere for a coherent and a number squeezed state.

3.3.1 The MCTDHB method

As has already been pointed out, the generic two-mode model neglects the details about the orbitals ϕ_L and ϕ_R. For very slow (quasi-adiabatic) deformations of the trapping potential and weak interaction strength, one can approximately determine Ω as a function of the splitting parameter λ from the ground and excited states of the single-particle Schrödinger equation for each λ. However, as soon as there are slight condensate oscillations, this does not work anymore.

We will thus employ a general variational framework for many-body systems that has been developed in the Theoretical Chemistry group of L. S. Cederbaum in Heidelberg over the last years [46]. In particular, the *Multi-configurational time-dependent Hartree* (MCTDH) method has been introduced in 1990 by H.-D. Meyer *et al.* [47]. This method is in many situations a very efficient tool for treating systems of distinguishable particles with many degrees of freedom. The *Multi-configurational time-dependent Hartree for bosons* (MCTDHB) method has been introduced in 2008 by Alon *et al.* [48, 19], and takes explicitly into account the bosonic symmetry. We will discuss this model now.

MCTDHB is based on an ansatz for the field operator which goes as

$$\hat{\Psi}(\mathbf{r}) = \sum_{i=1}^{M} \hat{a}_i(t)\phi_i(x,t)\,, \tag{3.30}$$

where now both the modes ϕ_i and the occupations (described by the annihilation operator $\hat{a}_i$) are time-dependent. For $M \to \infty$ this is just a general expansion of a state and no approximation has been introduced so far. We aim at describing Bose-condensed systems. For example, we discussed that GP might work well in the case that only a single orbital is relevant. Generally, if we have M-fold *fragmented* systems, i.e., M eigenvalues of the one-body reduced density Eq. (3.3) are "macroscopic" [38], M orbitals might very well capture the physics. In addition, however, a "quantum depletion", i.e., some small, but finite eigenvalues, can also have effects and might require more orbitals, see Chap. 7. Summarizing, bosonic systems exhibit a collective behaviour of the particles, which allows us to reduce the basis of the state space enormously. This can in practice be achieved by cutting the sum of Eq. (3.30) to finite M terms. Since the computational effort grows exponentially with the number of modes M, this is a very effective approximation.

We then write a general state as a superposition of symmetrized states, which are usually called *permanents*. A general permanent made up of M different one-particle functions can be written as

$$|\vec{n};t\rangle = \frac{1}{\sqrt{n_1!n_2!...n_M!}}\left(\hat{a}_1^\dagger(t)\right)^{n_1}\left(\hat{a}_2^\dagger(t)\right)^{n_2}...\left(\hat{a}_M^\dagger(t)\right)^{n_M}|0\rangle\,, \tag{3.31}$$

where the vector $\vec{n} = (n_1, n_2, ..., n_M)$ describes the configuration. A general state is then given as

$$|\Psi(t)\rangle = \sum_{\vec{n}} C_{\vec{n}}(t)|\vec{n};t\rangle\,. \tag{3.32}$$

We are now left with a set of independent parameters, comprised of the coefficients $\{C_{\vec{n}}\}$ and orbitals $\{\phi_k(x,t\}$, which we have to determine. In order to find their time dependence, a variational calculus is used. In particular, within Lagrange formalism one formulates an action

$$S[\{C_{\vec{n}}(t)\},\{\phi_k(x,t)\}] = \int dt\left\{\langle\Psi|\big(\hat{H} - i\frac{\partial}{\partial t}\big)|\Psi\rangle - \sum_{i,j=1}^{M}\mu_{kj}(t)[\langle\phi_k|\phi_j\rangle - \delta_{kj}]\right\}. \tag{3.33}$$

Variation of S guarantees that the expectation value of the Schrödinger equation is minimized, and the orbitals are orthonormal. The variations are carried out with respect to the coefficients and orbitals. They are given in the App. A, as well as the general MCTDHB equations for an

arbitrary number of orbitals. We demonstrate here first that for $M = 1$, variation of Eq. (3.33) yields the GP equation, and then discuss the MCTDHB equations for two orbitals ($M = 2$). Variation of S with respect to ϕ yields for $M = 1$

$$i\frac{\partial}{\partial t}|\phi\rangle = \frac{\partial E[\phi]}{\partial \phi^*}\,, \tag{3.34}$$

where $E[\phi]$ is an energy functional

$$E[\phi] = \int dx\Big[\frac{1}{2}|\nabla\phi|^2 + V_\lambda(x)|\phi|^2 + \frac{U_0^{3D}}{2}|\phi|^4\Big]\,. \tag{3.35}$$

We obtain the GP equation, which can be regarded as the variational wave function for one mode. The corresponding many-body wave function is $\Psi(x_1, ..., x_N, t) = \prod_{i=1}^{N}\phi(x_i)$, i.e., a product of single-particle wave functions. In general, time-adaptive modes account for a lot of excitations and are thus very powerful. Compared to that, a huge amount of time-independent modes would be necessary to describe the same physics.

For the $M = 2$ case, we use gerade and ungerade orbitals [1]:

$$\begin{aligned} i\dot{\phi}_g &= \hat{\mathbf{P}}\Big[\hat{h}\phi_g + (f_g^g|\phi_g|^2 + f_g^e|\phi_e|^2)\phi_g + \tilde{f}_g\phi_g^*\phi_e^2\Big]\,, \\ i\dot{\phi}_e &= \hat{\mathbf{P}}\Big[\hat{h}\phi_e + (f_e^g|\phi_g|^2 + f_e^e|\phi_e|^2)\phi_e + \tilde{f}_e\phi_e^*\phi_g^2\Big]\,, \end{aligned} \tag{3.36}$$

where the coefficients are given by the elements of the one- and two-body reduced densities (Eq. (3.2)),

$$f_k^k = U_0\{\rho\}_{kk}^{-1}\rho_{kkkk}\,, \quad f_k^q = 2U_0\{\rho\}_{kk}^{-1}\rho_{kqkq}\,, \quad \tilde{f}_k = U_0\{\rho\}_{kk}^{-1}\rho_{kkqq}\,, \tag{3.37}$$

with k either g or e, and q the opposite. Since the orbitals have different parity, the one-body density is always diagonal and those orbitals are natural orbitals. In the orbitals equations a projector $\hat{\mathbf{P}} = 1 - |\phi_g\rangle\langle\phi_g| - |\phi_e\rangle\langle\phi_e|$ appears, which guarantees orthonormality of the orbitals. The inner product is defined as $\langle u|v\rangle = \int dx u^* v$. For the number distribution we have

$$i\frac{\partial \mathbf{C}(t)}{\partial t} = \mathcal{H}\mathbf{C}\,, \tag{3.38}$$

which is very similar to Eq. (3.18), except that more general matrix elements are involved:

$$\mathcal{H} = -\Omega\hat{J}_x + \frac{1}{2}{\sum_{k,q,l,m}}'\,\hat{a}_k^\dagger\hat{a}_q^\dagger\hat{a}_l\hat{a}_m W_{kqlm}\,. \tag{3.39}$$

The prime indicates that the sum only runs over even combinations of indices. Rewritten for gerade and ungerade orbitals, we have $\hat{J}_x = \frac{1}{2}(\hat{a}_g^\dagger\hat{a}_g - \hat{a}_e^\dagger\hat{a}_e)$ and $\Omega = \langle\phi_e|\hat{h}|\phi_e\rangle - \langle\phi_g|\hat{h}|\phi_g\rangle$. The two-body matrix elements are given by

$$W_{kqlm} = U_0\int dx\phi_k^*(x)\phi_q^*(x)\phi_l(x)\phi_m(x)\,. \tag{3.40}$$

In Fig. 3.3 we give a sketch of the method: Eqs. (3.36) and (3.38) are nonlinear, coupled equations, such that both the state vector, as well as the orbitals are calculated self-consistently.

We briefly discuss ground state properties. For the unsplit trap, more than 99% of the atoms occupy ϕ_g. Then, the GP-like nonlinearities f_k^k and f_k^q are such that a GP equation for ϕ_g with N atoms is recovered. $\tilde{f}_e$ is instead very large for ϕ_e, which gives it a Bogoliubov like structure. For the split trap, the orbitals $\phi_g \pm \phi_e$ resemble GP orbitals with N/2 atoms localized in each well.

[1] We note that the basis is not uniquely defined but allows for unitary transformations (gauge freedom). [19]

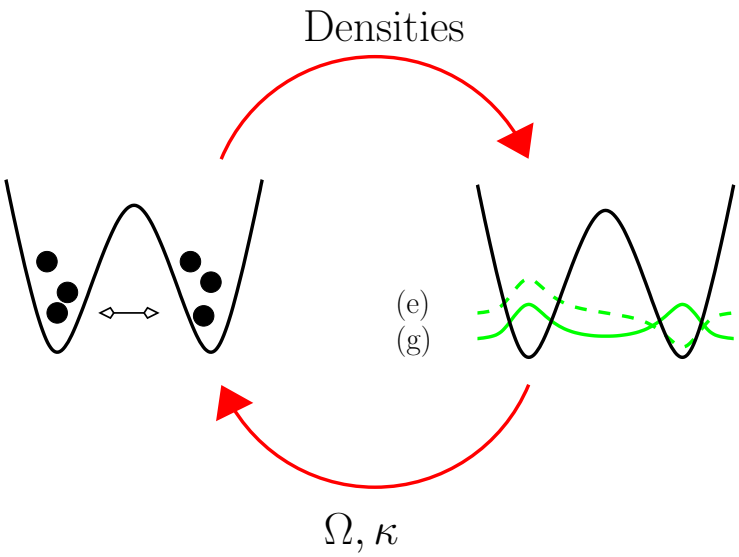

Figure 3.3: Sketch of MCTDHB(2) in a double-well: the gerade-ungerade orbitals are coupled to a two-mode Hamiltonian by the densities, and the latter depends on the tunnel coupling Ω and interactions κ, which are determined from the orbitals.

Chapter 4

Atom interferometry with trapped BECs

In this chapter we introduce trapped BEC interferometry. We give a general introduction into this field in Sec. 4.1. We then describe the basic principles of two types of interferometers which are investigated in this thesis: the Time-of-flight (TOF) interferometer, and the Mach-Zehnder (MZ) interferometer. We discuss the necessary steps in the interferometer performance. In Sec. 4.3 we introduce the *standard quantum limit* and the *Heisenberg limit*, which are very important concepts in quantum measurement theory. In particular, we demonstrate for the example of two-level systems how quantum correlations can enhance the measurement sensitivity. We then turn to the theory of lower quantum bounds and phase estimation in Sec. 4.4, which is important to calculate the phase sensitivity of a given interferometer and read-out method. We finally discuss the phase sensitivity of the TOF and MZ interferometer and motivate the importance of squeezed states.

4.1 Basic principles

Atom interferometry is a very promising and rapidly developing field, since interferometry performed with atoms offers manifold advantages compared to photons or electrons [7]. Atoms are highly sensitive to inertial and electromagnetic forces. The de-Broglie wavelength of thermal atoms is 30000 larger than the optical wavelength, which helps to detect much smaller signals. A broad variety of atomic properties can be chosen, such as the mass, the electric polarizability, or magnetic moment. Further, atoms can be controlled using lasers very precisely. The most prominent application of atom interferometers could be the detection of gravitational waves.

An essential step in an atom interferometer is the creation of two paths, which then can interact independently with external potentials. Very often this is achieved in momentum space. A different approach, which is the one considered in this thesis, is a *confined interferometer using a BEC*. Thereby, a BEC is split into two parts when the trapping potential is transformed from a single to a double well. Thus, the splitting is in position space, which is particularly important for measuring the Casimir force, spatially varying fields, or small objects coupled trough evanescent fields. The advantage of the confinement lies in the protection of the atom against the gravitation. Whenever the atoms are trapped, and do not fall down as in other atom interferometers, the hold time can be made very long. This can be very important for precision measurements. The confinement allows for large scale quantum coherence, which can be exploited to work with a smaller number of atoms. Finally, confined atom interferometers can be realized on atom chips [13], which can be in principle made portable due to miniaturization.

The key stages of a general interferometer are

1. **Preparation** of a well characterized **initial state**,
2. **splitting** of the state such that two states result with well defined phase (**"coherent"**),
3. independent evolution of the split parts, where a relative **phase** due to an external potential is **accumulated**, and
4. a **readout** stage, where a measurement is performed (e.g., atom or density measurement).

4.2 Types of interferometers

We now introduce two types of trapped BEC interferometers, which we will investigate in this thesis.

4.2.1 Time-of-flight (TOF) interferometer

Here, a condensate is split into two halves and a relative phase is imprinted due to an external potential $\hat{H}_{ext} = \Delta E \hat{J}_z$. The transformation from the initial to the final state is thus given by

$$|\psi_{OUT}\rangle = e^{-i\theta \hat{J}_z} |\psi_{\mathrm{IN}}\rangle \,, \tag{4.1}$$

where $\theta = \Delta E T_{\mathrm{p}hase}$ is the accumulated phase for the phase accumulation time $T_{\mathrm{p}hase}$. Thereafter, the condensates are released from the trap and expand in time-of-flight for a time $T_{\mathrm{t}of}$, as schematically shown in Fig. 4.1 (upper panel). The interference fringes are then recorded. The phase information is encoded in the interference fringes [49]. We consider a field operator of the two expanding clouds

$$\hat{\Psi}(x) = \hat{a}_L \, \phi_L(x) + \hat{a}_R \, e^{-i\theta} \phi_R(x) \,. \tag{4.2}$$

$\phi_L(x)$ and $\phi_R(x)$ are two Gaussians with a variance σ^2 which increases with time $T_{\mathrm{t}of}$ due to the wave function expansion. The density reads

$$\rho(x) = \frac{N}{2} \Big(n_L(x) + n_R(x) \Big) + 2\sqrt{n_L(x) n_R(x)} \cos(kx + \theta) \left\langle \hat{J}_x \right\rangle \,. \tag{4.3}$$

Hereby, $n_{L,R}$ denote the probability distributions for the condensates, and $k = 2\hbar t d / m\sigma (T_{\mathrm{t}of})^2 \sigma^2$ determines the fringe separation. Obviously, fringes appear in the density which depend on the phase shift θ. The contrast of the fringes is determined by $\alpha := \langle \hat{J}_x \rangle / (N/2)$, which is called the *coherence factor*. It is $\alpha = 1$ for a coherent state, and $\alpha = 0$ for a Fock state (winds around the equator of the Bloch sphere). For number squeezed states, $0 < \alpha < 1$.

At this point we remark that $\alpha = 0$ does not imply that there are no interference fringes at all [50]. In a single experiment, interference fringes might appear. However, for many experimental realizations they average out and the interference is given by the mean density Eq. (4.3).

4.2.2 Mach-Zehnder (MZ) interferometer

The MZ interferometer with trapped BECs [see Fig. 4.1 (lower panel)] works analogous to an optical MZ, where an incoming laser beam is split at a beam splitter, and a phase is accumulated in one of the split beams. Thereafter, at a second beam splitter the two beams are recombined and the phase difference transformed into a number difference, which is detected at each output port. The basic notion of this type of interferometer is to transform number into phase information by use of beam splitters. An analogous operation for trapped BECs consists in the *cold atom beam splitter* [51], which is effected by the Hamiltonian $\hat{H}_{\mathrm{BS}} = -\Omega(t) \hat{J}_x$. It can be realized by two condensates in a double-well with a finite barrier, such that they are allowed to tunnel for some

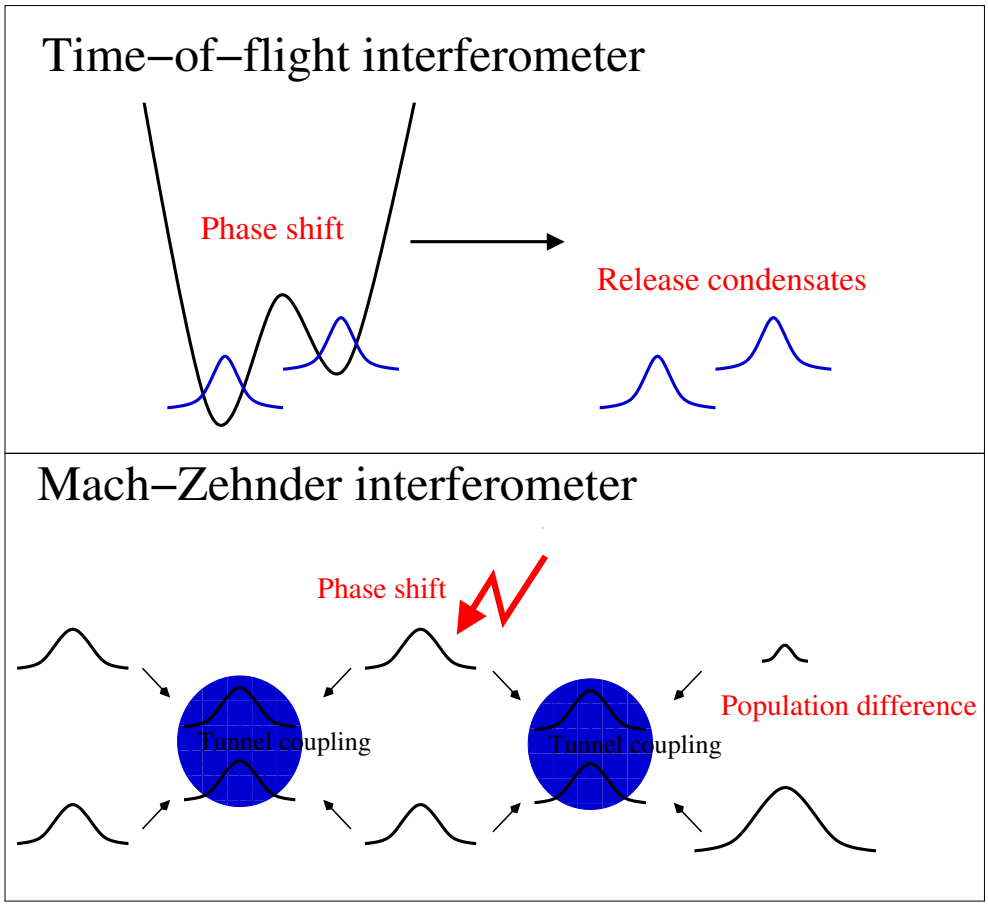

Figure 4.1: Upper panel: Key stages of a TOF interferometer. A relative phase is imprinted in two trapped condensates, which are thereafter expanded in TOF and the fringe pattern recorded. Lower panel: Key stages of a MZ interferometer. Two condensates are trapped in a double-well. The barrier height is reduced for some time such that the atoms are allowed to tunnel. This realizes a "cold atom beam splitter", where an initially number squeezed state is transformed to a phase squeezed state. Next, a phase is imprinted, and at a second beam splitter, phase information is transformed into number information. The relative atom number is measured.

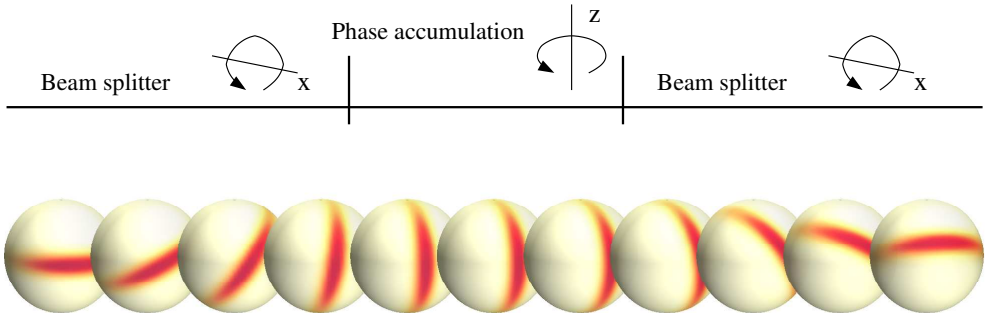

Figure 4.2: Mach-Zehnder interferometer sequence without interactions on the Bloch sphere for an initially number squeezed state. The first beam splitter transforms number into phase squeezing, an external force rotates the state around the polar axes, and finally the second beam splitter rotates the state such that the phase information is now encoded in the mean relative atom number.

time, such that $\int_0^T dt\Omega(t)dt = \pi/2$. On the Bloch sphere, this corresponds to a $\pi/2$ rotation of the state around the x-axis, see Fig. 4.2. The first beam splitter is only effective for squeezed initial states, since a coherent state is an eigenstate of $\hat{H}_{\mathrm{BS}}$. The particular advantage of squeezed states will be discussed later in this chapter in context of the phase sensitivity. In the second stage, a relative phase is imprinted due to an external potential $\hat{H}_{ext}$, which corresponds to a rotation about the polar axis on the Bloch sphere. The final beam splitter is crucial as it transforms the phase information into number information. The total interferometer transformation is then given as

$$|\psi_{OUT}\rangle = e^{i\pi/2\hat{J}_x} e^{-i\theta\hat{J}_z} e^{i\pi/2\hat{J}_x} |\psi_{\mathrm{IN}}\rangle = e^{-i\theta\hat{J}_y} |\psi_{\mathrm{IN}}\rangle\,, \tag{4.4}$$

For the read-out, the relative number of atoms has to be measured in-situ.

4.3 Quantum enhanced metrology

In this section, we discuss the basic notions of quantum enhanced metrology using the example of N two-level systems (TLS) with states $|0\rangle_i$ and $|1\rangle_i$ $(i = 1, ..., N)$. In particular, by following Ref. [52] we demonstrate how quantum correlations can be used to beat the shot noise limit.

4.3.1 Standard quantum limit

It describes the phase sensitivity of uncorrelated particles. Consider an N-fold product state of a superposition of two-level systems

$$|\psi\rangle = \prod_{j=1}^{N} (|0\rangle_j + |1\rangle_j)/\sqrt{2}\,. \tag{4.5}$$

Then the variance of an N-particle state is given by the average of the variance of each particle. This is a consequence of the central limit theorem relevant for uncorrelated measurement results. If we measure the population of the levels we find the result x_j for the j-th particle, where x_j is either 0 or 1 depending on where it has been detected. The mean value is given by $\sum_{j=1}^{N} x_j/N$, and the variance is

$$\Delta(\sum_{j=1}^{N} x_j/N) = \sqrt{\sum_{j=1}^{N} \Delta^2 x_j}/N = 1/\sqrt{N}\,. \tag{4.6}$$

The last equality holds because of *quantum projection noise*, which means that for $|0\rangle_j + |1\rangle_j$ the variance is $\Delta x_j = 1$. A similar behaviour can be found also for coherent light, which consists of uncorrelated photons, and the fluctuations of the photon number show Poissonian statistics (shot noise).

4.3.2 Exploiting quantum correlations

How can we exploit quantum mechanics to improve the phase sensitivity? In particular, beating the $1/\sqrt{N}$ scaling in a measurement using N particles is desired. Therefore we need a correlated state of the N particles, as well as a collective or "nonlocal" measurement. For this we consider a fictitious interferometer, similar to the Ramsey method . A state of a two-level system $|\psi_{IN}\rangle$ becomes a phase imprinted ($|\psi_{OUT}(\theta)\rangle$) and is projected onto the input state $p(\theta) = |\langle\psi_{IN}|\psi_{OUT}(\theta)\rangle|^2$. For one atom we have

$$|\psi_{IN}\rangle = (|0\rangle + |1\rangle)/\sqrt{2}\,, \quad |\psi_{OUT}\rangle = (|0\rangle + e^{i\theta}|1\rangle)/\sqrt{2}\,, \tag{4.7}$$

and thus $p(\theta) = \cos^2(\theta/2)$. One can use error propagation to determine the phase sensitivity $\Delta\theta = \Delta p/|\frac{\partial p(\theta)}{\partial\theta}|$, where it is easy to see that $(\Delta p)^2 = p(\theta) - p(\theta)^2$. In this case we obtain $\Delta\theta = 1$, or $\Delta\theta = 1/\sqrt{N}$ if N independent measurements are carried out. We turn to an *entangled state*:

$$|\psi_{IN}\rangle = \Big(\prod_{j=1}^{N}|0\rangle_j + \prod_{j=1}^{N}|1\rangle_j\Big)/\sqrt{2} \quad \rightarrow |\psi_{OUT}\rangle = \Big(\prod_{j=1}^{N}|0\rangle_j + e^{iN\theta}\prod_{j=1}^{N}|1\rangle_j\Big)/\sqrt{2}\,. \tag{4.8}$$

The measurement probability becomes $p(\theta) = \cos^2(N\theta/2)$, which in turn leads to a so-called *Heisenberg* limited measurement $\Delta\theta = 1/N$, since the error Δp remains the same, while the change rate of $p(\theta)$ with θ increases by N. We will show in the next section, that this is a fundamental quantum limit.

4.4 Phase sensitivity

4.4.1 Lower bounds

In this section we discuss the lower quantum bounds of the phase sensitivity for the example of an interferometer with transformation

$$|\psi_{OUT}\rangle = e^{-i\theta\hat{J}_{\vec{n}}}|\psi_{\mathrm{IN}}\rangle\,, \tag{4.9}$$

where $\hat{J}_{\vec{n}_i} = \hat{\vec{J}}\cdot\vec{n}_i$ are the generators of the interferometer, and $\vec{n}_1 = \vec{x}$, $\vec{n}_2 = \vec{y}$, $\vec{n}_3 = \vec{z}$. We closely follow [53, 54] and the lecture notes of A. Smerzi. In order to calculate the lower bound for the MZ, we consider a general estimator for the phase shift

$$\theta_{\mathrm{est}}(n_1, ..., n_p) = f(n_1, ..., n_p)\,. \tag{4.10}$$

It is a function of the sample $\{n_j\}$, which stands for any kind of measurement, for example the relative atom number. Specific estimators will be considered in the next section. Here, we assume that it is unbiased $\langle\theta_{est}\rangle = \theta$, i.e., its expectation value gives the true phase shift. Given the conditional probability distribution $P(n_1, ..., n_m|\theta)$, one can write this relation as (we assume continuous n_i, but it works similar for discrete measurement outcomes)

$$\int P(n_1, ..., n_p|\theta) \times \Big[\theta_{\mathrm{est}}(n_1, ..., n_p) - \theta\Big] dn_1 ... dn_p = 0\,. \tag{4.11}$$

Taking the partial derivative of this equation with respect to $\frac{\partial}{\partial\theta}$, we obtain

$$\int \left[\frac{1}{\sqrt{P}}\frac{\partial P}{\partial\theta}\right]\left[\sqrt{P}(\theta_{\rm est}-\theta)\right] dn_1...dn_p = 1\,, \tag{4.12}$$

where it is used that θ_{est} does not depend on θ, and factors of $\frac{1}{\sqrt{P}}$ and $\sqrt{P}$ have been inserted such that they cancel. By applying the Schwarz inequality $|\int A(x)B(x)dx|^2 \leq \int |A(x)|^2dx \int |B(x)|^2dx$ to the left hand side with $A = \frac{1}{\sqrt{P}}\frac{\partial P}{\partial\theta}$ and $B = \sqrt{P}(\theta_{\rm est}-\theta)$, we obtain

$$\int \frac{1}{P}\Big(\frac{\partial P}{\partial\theta}\Big)^2 dn_1...dn_p \cdot \int P(\theta_{\rm est}-\theta)^2 dn_1...dn_p \geq 1\,. \tag{4.13}$$

Obviously, the second factor on the left hand side is equal to the variance of the estimator, $\Delta\theta^2_{est}$. Hence we can write

$$\Delta\theta_{\rm est} \geq 1/\sqrt{pF(\theta)}\,, \tag{4.14}$$

where

$$F(\theta) = \int dn \frac{1}{P(n|\theta)}\Big(\frac{\partial P(n|\theta)}{\partial\theta}\Big)^2 \tag{4.15}$$

is the *classical Fisher information* (CFI). Hereby, it has been assumed that the measurement results are independent and the probability distributions equal in each measurement, i.e.,

$$P(n_1,...,n_m|\theta) = \prod_{j=1}^{p} P(n_j|\theta)\,. \tag{4.16}$$

Thus, the phase sensitivity Eq. (4.14) is the best we can get for the specific measurement we considered. It is more lengthy to show that the upper bound to the CFI is given by the *quantum Fisher information* (QFI) [55]

$$F(\theta) \leq F_Q[|\psi\rangle_{\rm in}, \hat{J}_{\vec{n}}] = [dl(\theta)/d\theta]^2 = 4(\Delta\hat{J}_{\vec{n}})^2\,. \tag{4.17}$$

For the class of interferometers we consider here, Eq. (4.9), the QFI is given by four times the variance of the generator of the transformation. It has an interpretation as a "quantum statistical speed": assume $l(\theta)$ is the statistical distance between states in Hilbert space. It is defined as

$$l(\theta) = \lim_{p\to\infty} \frac{1}{2\sqrt{p}} \times (\text{number of distinguishable states})\,. \tag{4.18}$$

and is independent of the kind of measurement since it is defined in the limit of $n \to \infty$ (central limit theorem). A measurement for which the classical Fisher information is equal to the quantum Fisher information, is called an "optimal" measurement. The ultimate sensitivity is then called *Cramer-Rao lower bound* (CRLB) [55, 56]

$$\Delta\theta_{QCR} = \frac{1}{\sqrt{pF_Q[|\psi\rangle_{\rm in}, \hat{J}_{\vec{n}}]}}\,, \tag{4.19}$$

and depends only on the given input state and the interferometer characterized by its generator. The QFI is bounded by $F_Q[|\psi\rangle_{\rm in}, \hat{J}_{\vec{n}}] < N^2$ and thus, the fundamental limit of phase sensitivity is the Heisenberg limit $\Delta\theta_{\rm HB} = 1/\sqrt{p}N$.

4.4.2 Phase estimation

In this section we consider several estimators of interest for atom interferometry.

Maximum likelihood estimator (MLE)

It can be shown, that the *maximum likelihood* estimator

$$\theta_{\mathrm{ML}} = \max_\theta P(n_1, ..., n_p|\theta)\,, \tag{4.20}$$

satisfies the CRLB in the limit of large p (central limit). However, the joined conditional probability distributions $P(n_1, ..., n_p|\theta)$ are usually not known, and thus the MLE not very useful in practice.

Mean value

A very common estimator is a function of the mean value of the sample

$$\bar{\theta} = f(\bar{N})\,, \qquad \bar{N} = \frac{1}{p}\sum_{i=1}^{p} n_i\,. \tag{4.21}$$

In the central limit it gives rise to a sensitivity

$$\Delta\theta = \frac{\sigma}{\sqrt{p}\left|\frac{\partial\langle\hat{N}\rangle}{\partial\theta}\right|}\,, \tag{4.22}$$

where $\sigma^2 = \frac{1}{p}\sum_{i=1}^{p}(n_i - \bar{N})^2$ and $\hat{N}$ is the measurement operator. This formula is sometimes also referred to as *error propagation formula*. It is not optimal as it does not satisfy the CRLB, but can give sub-shot noise sensitivity.

Bayesian estimation

The MLE and the mean value are useful in general only for large p. But what can we learn from the single shot measurement ($p = 1$)? For example the mean value $\bar{\theta}$ satisfies Eq. (4.22) for small p only if the underlying probability distribution is already Gaussian, or it is a linear function. A more general phase estimation scheme is provided by the following. Starting from the Bayes formula

$$P(A|B) = \frac{P(B|A)P(A)}{P(B)}\,, \tag{4.23}$$

we obtain

$$P(\theta|\{n_j\}) = \prod_{j=1}^{p} P(n_j|\theta)/\mathcal{N}\,, \tag{4.24}$$

up to a normalization $\mathcal{N}$, which provides a rule how to relate a sequence of measurement results $\{n_j\}$ to the probability that the actual phase has a certain value $P(\theta|\{n_j\})$. In this fashion, we get information on the phase even for small p. This is usually called "inversion of the probability". The actual phase is obtained as the maximum of the probability distribution, and the phase sensitivity typically as the 68 % confidence interval around it.

In practice, the conditional probabilities $P(n|\theta)$ have to be first measured. This corresponds to the "calibration" of the interferometer, where possible experimental errors can be taken into account [57].

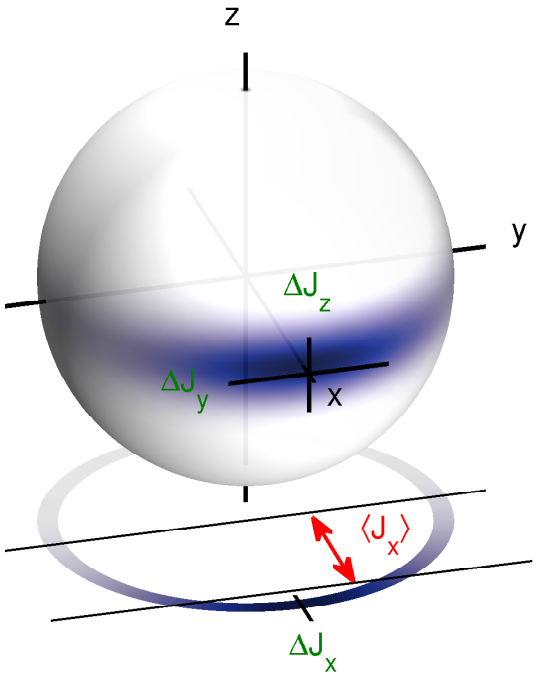

Figure 4.3: Number squeezed state on the Bloch sphere. Number fluctuations are suppressed, while phase fluctuations are enhanced. The coherence factor α, which determines fringe visibility in experiments, corresponds to polarization of the state on the x-axis.

4.4.3 Enhanced phase sensitivity by squeezed states

We discuss now the phase sensitivity and phase estimation schemes for the two types of interferometers we introduced in Sec. 4.2. Thereby we find that squeezed states are very useful for interferometry. For this purpose, we introduce now squeezing factors [9] which will be important in the following. A state which has reduced fluctuations in the operator $\hat{J}_\phi = \cos\phi\hat{J}_z + \sin\phi\hat{J}_y$, is referred to as *squeezed* state. Important examples are hereby *number squeezed* states ($\phi = 0$) and phase squeezed states ($\phi = \pi/2$). The reduced fluctuations in one direction are accompanied by enhanced fluctuations along the orthogonal direction. For example, in Fig. 4.3 we show a number squeezed state. Fluctuations according to $\hat{J}_y$ (phase fluctuations) are thus enhanced. We denote the corresponding squeezing factors as

$$\xi_N = \Delta J_z/(\sqrt{N}/2) \quad \text{and} \quad \xi_{\text{phase}} = \Delta J_y/(\sqrt{N}/2)\,. \tag{4.25}$$

Another important notion is *coherent spin squeezing*. It is generally given by

$$\xi^R = \frac{\sqrt{N}\Delta J_\phi}{\langle \hat{J}_x\rangle} = \frac{\Delta J_\phi}{\alpha\sqrt{N}/2}\,. \tag{4.26}$$

It takes into account that for interferometry based on mean values (see Sec. 4.4.2), the phase coherence α must be large. Thus, it is sometimes referred to as *useful squeezing* for interferometry [10, 11]. Squeezed states have in general a smaller phase coherence, which corresponds to a reduced polarization of the state on the x-axis of the Bloch sphere, see Fig. 4.3.

Time-of-flight interferometer

In the literature [58], it has been claimed that the phase sensitivity is related to density fluctuations, which are proportional to ΔJ_y. Employing the error propagation formula Eq. (4.22) and

using $\partial n/\partial\theta = \langle \hat{J}_x \rangle$ [see Eq. (4.3))], we obtain (at the optimal working point $\theta = 0$)

$$\Delta\theta = \frac{\Delta J_y}{\langle \hat{J}_x \rangle} = \xi_R/\sqrt{N}\,, \tag{4.27}$$

which requires coherent phase squeezing. The common approach for the read-out procedure is to fit the data to histograms of finite bins. However, this approach has major problems [59].

According to the CRLB $\Delta\theta = 1/(2\sqrt{p}\Delta J_z)$ (cf. Eq. (4.19)), phase squeezed states give sub-shot noise phase sensitivity. A suitable read out method is discussed in [59]. The CRLB allows for a more general class of states to give sub-shot noise or Heisenberg limited interferometry. However, coherently phase squeezed states are found to be most stable against particle loss [59].

Mach-Zehnder interferometer

If the estimator is based on the mean value of the sample $\bar{N}$, we obtain for the error propagation formula (at the optimal working point $\theta = 0$)

$$\Delta\theta = \frac{\Delta J_z}{|\langle \hat{J}_x \rangle|}\,. \tag{4.28}$$

Thereby we used

$$\langle \hat{J}_z{}^{out} \rangle = -\sin\theta \langle \hat{J}_x \rangle + \cos\theta \langle \hat{J}_y \rangle\,, \tag{4.29}$$

from which the error propagation $|\partial\langle \hat{J}_z^{out} \rangle/\partial\theta|$ follows. In Fig. 4.2 we show the whole interferometer sequence. The first beam splitter transforms number squeezing into phase squeezing, and the second one the other way around. Obviously, coherently number squeezed states give better phase sensitivity than the coherent state due to the reduced fluctuations. A finite coherence factor α is necessary, since otherwise, the mean value $\langle \hat{J}_z{}^{out} \rangle$ becomes independent of the phase.

The CRLB allowes for a more general class of states to give sub-shot noise or Heisenberg limited interferometry [57, 54], for example, a Fock state $|N/2\rangle_L|N/2\rangle_R$. The sensitivity due to the error propagation formula Eq. (4.29), however, diverges then. Thus, a Bayesian phase estimation strategy has to be employed, and for $p \approx 20$, Heisenberg scaling can be achieved.

Chapter 5

Optimal control theory

In this thesis, an important goal is the preparation of squeezed states. Therefore we will employ *optimal control theory* (OCT) [20] in order to determine the time variation trapping potential. OCT allows for devising control strategies which satisfy predefined control goals in an optimal way. It has found numerous applications in various fields of physics. Most successful experimental realizations have been achieved in quantum chemistry applied in the context of pulse shaping [60] and for molecules [21, 22]. A very useful tool in this context is feedback control. OCT has also been applied to atoms [61, 62] or semiconductors [63]. For BECs, optimal state trapping within the Gross-Pitaevskii equation has been demonstrated [23]. We outline in this chapter the important ingredients for the OCT approach we use. It is based on a Lagrangian framework, and we explain and derive the corresponding optimality system. We describe also the newly developed H^1 based OCT approach [64], which plays an important role in this thesis. Furthermore, we briefly discuss optimization and line search methods.

5.1 Outline of the method

OCT is sketched in Fig. 5.1. The main goal is the minimization of a cost functional, where as a constraint the equations of motion must be fulfilled. The ingredients are *forward*, *backward*, and *control* equations derived within a Lagrangian framework. Given a trial control, from this essentially follows a gradient of the cost functional in control space. This could be used as a search direction for an improved control (*steepest descent*). However, much better methods exist to determine a new search direction, such as *nonlinear conjugate gradient* (NCG) or *quasi-Newton* (BFGS) schemes. In particular we discuss that the actual gradient depends on the function space where the control lives in. In this thesis, we experienced a striking dependence on this feature. Thereafter, it is important to employ a line search algorithm, which determines how far one has to go along the search direction. After all, a new control is found and iteration proceeds. In the following we describe in detail all the steps and methods involved [65, 66, 64].

5.2 Cost functional

Lets call ψ a state vector, and λ a control parameter. We consider a control problem with the following cost functional:

$$J(\psi,\lambda) = J_0(\psi,\lambda) + \frac{\gamma}{2}\int_0^T \left(\dot{\lambda}(t)\right)^2 dt \,, \tag{5.1}$$

where $J_0(\psi,\lambda)$ is the quantity which we want to be small. The second term is a regularization, weighted by a factor γ, which penalizes rapid variations. This is a formal requirement to have

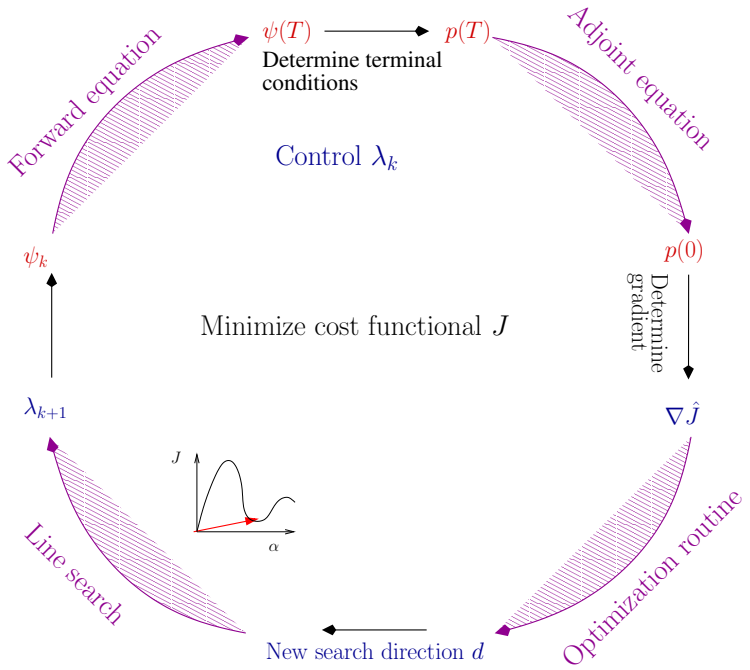

Figure 5.1: Given a trial control λ_0, evaluating the forward and backward (or adjoint) equations (obtained from the Lagrangian formulation) yield a gradient of the cost functional ∇J in control space. This could be used as a search direction d for an improved control λ_1 (*steepest descent*). However, much better methods exist to determine a new search direction d, such as *nonlinear conjugate gradient* (NCG) or *quasi-Newton* (BFGS) schemes. Thereafter, it is important to employ a line search algorithm, which determines how far one has to go along the search direction (αd). Then, a new control is found and iteration proceeds.

a well-posed optimal control system. Another choice would be $\int_0^T \Big(\lambda(t)\Big)^2 dt$, which penalizes, e.g., large laser fields. However, this is not reasonable for our purposes, and the first type of regularization is best suited.

5.3 Lagrangian formulation

The next step is the inclusion of dynamical constraints ("time evolution") using a Lagrange functional. If we have general equations of motion, $i\dot{\psi} = f(\psi, \lambda)$, which depend on a time-dependent control parameter λ, the Lagrange functional reads

$$L(\psi, \tilde{\psi}, \lambda) = J(\psi, \lambda) + Re\langle \tilde{\psi}, i\dot{\psi} - f(\psi, \lambda)\rangle \,. \tag{5.2}$$

Here we introduced a Lagrange multiplier $\tilde{\psi}$, which is usually called the *adjoint* state. The bracket $\langle u, v\rangle = \int_0^T \langle u(t)|v(t)\rangle dt$ denotes integration over time. Further, we have an initial condition for the state, and hold the control fixed between two points:

$$\psi(0) = \psi_0, \qquad \lambda(0) = \lambda_0,\ \lambda(T) = \lambda_T. \tag{5.3}$$

$L(\psi, \tilde{\psi}, \lambda)$ is minimized if the Fréchet (or functional) derivatives with respect to ψ^*, $\tilde{\psi}^*$, and λ^* are zero. The Fréchet derivative can be obtained as follows:

$$\delta L_\psi[\psi, \tilde{\psi}, \lambda; \delta\psi, \tilde{\psi}, \lambda] := \frac{\partial}{\partial\epsilon} L[\psi + \epsilon\delta\psi, \tilde{\psi}, \lambda]\Big|_{\epsilon=0}, \tag{5.4}$$

and similar for the other variables. Here, $\delta\psi$ is a "test function", which must be compatible with the initial condition for ψ, i.e., $\delta\psi(0) = 0$. We decompose our cost functional in a part depending only on $\psi(T)$, and one depending on $\psi(t)$, such that it reads $J = J_T(\psi(T)) + \int dt \tilde{J}(\psi)$. Furthermore, $\tilde{L} = Re\langle\tilde{\psi}|i\dot{\psi} - f(\psi, \lambda)\rangle$, and using integration by parts, we obtain

$$\delta L_\psi[\psi, \tilde{\psi}, \lambda; \delta\psi, \tilde{\psi}, \lambda] = \left\langle \delta\psi, \frac{\partial(\tilde{J} + \tilde{L})}{\partial\psi^*} - \frac{d}{dt}\frac{\partial\tilde{L}}{\partial\dot{\psi}^*} \right\rangle + \left\langle \delta\psi, \frac{\partial\tilde{L}}{\partial\dot{\psi}^*} + \frac{\partial J_T}{\partial\psi^*} \right\rangle\Bigg|_{t=T} + \text{c.c.} = 0\,. \tag{5.5}$$

This yields Euler-Lagrange equations for the variables to be solved backward in time,

$$\frac{\partial(\tilde{J} + \tilde{L})}{\partial\psi^*} - \frac{d}{dt}\frac{\partial\tilde{L}}{\partial\dot{\psi}^*} = 0\,, \tag{5.6}$$

as well as boundary terms which give rise to the *terminal condition* for Eq. (5.6)

$$\frac{\partial\tilde{L}}{\partial\dot{\psi}^*} + \frac{\partial J_T}{\partial\psi^*}\Bigg|_{t=T} = 0\,. \tag{5.7}$$

The variation with respect to the adjoint state yields the equations of motion for ψ by construction:

$$\delta L_p[\psi, \tilde{\psi}, \lambda; \psi, \delta\tilde{\psi}, \lambda] = \frac{1}{2}\big\langle \delta\tilde{\psi}, i\dot{\psi} - f(\psi, \lambda)\big\rangle + \text{h.c.} = 0\,. \tag{5.8}$$

Finally, the so-called *control equation* is obtained by equating to zero the Fréchet derivative with respect to the control parameter λ:

$$\delta L_\lambda[\psi, \tilde{\psi}, \lambda; \psi, \tilde{\psi}, \delta\lambda] = -\int_0^T dt \left(\gamma\ddot{\lambda} + \Re\Big\langle\tilde{\psi}\Big|\frac{\partial f(\psi, \lambda)}{\partial\lambda}\Big\rangle\right)\delta\lambda + \text{c.c.} = 0\,, \tag{5.9}$$

where $\delta\lambda(0) = \delta\lambda(T) = 0$, in order to be compatible with the boundary conditions for λ, Eqs. (5.3).

5.4 Gradient: L^2 vs. H^1 formulation

If equal to zero, Eqs. (5.5), (5.8), and (5.9) characterize the *optimal* control. Since those equations are in most cases not solvable analytically by direct inversion, one has to rely on numerical schemes for determining the optimal control. Hence, one starts with an initial *guess* λ_{guess} and employs an iterative scheme to improve the control in successive steps. This comprises the evaluation of the *forward* equation for the state ψ with the initial condition $\psi(0) = \psi_0$, and the *backward* equation for the adjoint state $\tilde{\psi}$ with the appropriate terminal condition. For any non-optimal control, Eq. (5.9) is not equal to zero. The equation then has another meaning: If for given λ, ψ and $\tilde{\psi}$ fulfill their respective equations, we can define uniquely a *reduced* cost functional:

$$\hat{J}(\lambda) = J(\psi(\lambda), \lambda). \tag{5.10}$$

The actual form of the gradient of $\hat{J}$, which tells us how to get an improved control, depends on the function space of $\lambda(t)$ [64]. In particular, the gradient is defined as

$$\delta_\lambda \hat{J}[\lambda; \delta\lambda] = \left(\nabla \hat{J}_X, \delta\lambda\right)_X, \tag{5.11}$$

where X denotes the function space. Note that $\delta_\lambda \hat{J}[\lambda; \delta\lambda] = \delta_\lambda \hat{L}[\psi, \tilde{\psi}, \lambda; \psi, \tilde{\psi}, \delta\lambda]$ because ψ obeys the equations of motion. The usual choice is $\lambda \epsilon L^2(0, T; \mathbb{R})$, with the L^2 inner product, which we denote as $(\lambda, \lambda')_{L^2} = \int_0^T dt\, \lambda^* \lambda'$. We then obtain an explicit expression for the gradient of the cost functional by comparing Eqs. (5.9) and (5.11):

$$\nabla \hat{J}_{L^2}(\lambda) = -\gamma \ddot{\lambda} - \Re\Big\langle \tilde{\psi} \Big| \frac{\partial f(\psi, \lambda)}{\partial \lambda} \Big\rangle. \tag{5.12}$$

Another choice is $\lambda \epsilon H^1(0, T; \mathbb{R})$, where H^1 is the space of L^2 functions with weak derivatives again in L^2. The corresponding inner product is $(\lambda, \lambda')_{H^1} = (\dot{\lambda}, \dot{\lambda}')_{L^2}$. This is a more natural choice n our case, since we have a regularization term which corresponds to an H^1 inner product, see Eq. (5.1). For the inner products we have

$$\left(\nabla \hat{J}_{H^1}(\lambda), \delta\lambda\right)_{H_1} = \left(\nabla \hat{J}_{L^2}(\lambda), \delta\lambda\right)_{L^2}. \tag{5.13}$$

Using integration by parts we find the H^1 gradient as

$$\frac{d^2}{dt^2}[\nabla \hat{J}_{L^2}(\lambda)] = \gamma \ddot{\lambda} + Re\Big\langle \tilde{\psi} \Big| \frac{\partial f(\psi, \lambda)}{\partial \lambda} \Big\rangle, \tag{5.14}$$

which is a Poisson equation for $-\nabla \hat{J}_{L^2}(\lambda)$ with the same right hand side as Eq. (5.12).

Although the L^2 gradient is the standard choice in literature, the H^1 gradient is the more stable one whenever $\int dt \dot{\lambda}^2$ is penalized. For example, the degree of smoothness is the same between the gradient and λ. Thus, the gradient will always be a smooth function. In contrast, in Eq. (5.12) it might happen that $\gamma \ddot{\lambda}$ is not smooth and so the gradient, and in turn λ is not in L^2 anymore. Another important property is that we can impose Dirichlet boundary conditions $[\nabla \hat{J}(\lambda)](0) = 0$ and $[\nabla \hat{J}(\lambda)](T) = 0$. In contrast, the L^2 gradient is finite at $t = T$, although the control is kept constant at the boundaries.

5.5 Optimization methods

Having at hand the gradient $g := \nabla \hat{J}(\lambda)$, how can one find a search direction? The simplest way is to employ the method of **steepest descent**. Thereby, one takes a step along the direction of the gradient $d_{k+1} = -g_{k+1}$. The convergence is rather slow for this method, since steps are

frequently taken successively along the same direction. If the curvature in control space is similar to a half-pipe, it is searched in a zigzag-like behaviour, moving up and down the half-pipe, and only slowly approaching the minimum. A strongly improved convergence is achieved by employing the **conjugate gradient** method. The basic idea is that at each step, the direction should be different compared to the old direction. For instance, taking one step along each basis vector of control space with the right step size leads to the solution. This can be easily done in a Euclidean space. However, in general the eigenvectors of the system are not known. Therefore one tries to make steps along a *conjugate* direction, which is in the linear case $Ax = b$ defined as $d_i A d_j = 0$. The generalization to nonlinear problems is called *nonlinear conjugate gradient* (NCG) [65]. Generally, the new search direction will recursively depend on the old one as

$$d_{k+1} = -g_{k+1} + \beta_k d_k, \tag{5.15}$$

where the choice of β_k is somewhat heuristic, and one can choose between several schemes. Another methods use the second derivative instead of the first one, which are called **Newton** methods. Since the computation of the Hessian matrix can be quite expensive, there are **quasi-Newton** (BFGS) [65, 66] schemes which approximate the true Hessian. Convergence is faster in BFGS compared to NCG, but more computations are needed in each iteration.

5.6 Line search

If we have calculated the search direction with the help of one of the methods mentioned above, we still have to determine how far we should go along this direction,

$$\lambda_{k+1} = \lambda_k + \alpha_k d_k. \tag{5.16}$$

Thus, one has to determine α_k. This is achieved with a *line search algorithm*. Among the methods we mention *Armijo-Goldstein*, *Wolf-Powell*, and *bisectional* approaches [65].

Chapter 6

Condensate splitting

In this chapter, number squeezing created during condensate splitting is discussed . We start by reviewing quasi-adiabatic splitting in Sec. 6.1, which is found to be a very inefficient process. We therefore employ OCT to find optimized splitting controls, which yield more number squeezing for the same splitting time. We first discuss optimized splitting within the generic two-mode model, in order to understand the underlying physical mechanisms. Realistic control sequences for the trap variations can be obtained when OCT is applied to MCTDHB.

6.1 Quasi-adiabatic splitting

For a double-well potential with large enough barrier height the interactions favor well defined atom numbers, as discussed in Sec. 3.3. Therefore, if a dynamical splitting can be done sufficiently slowly, such that the state vector $\mathbf{C}$ can follow the ground state, the split condensates end up in a squeezed state [43, 11]. In order to analyse the dependence on the time scale of the ramp process, we consider an exponential turning-off of the tunnel coupling $\Omega(t) = \Omega_0 e^{-\tau/t_c}$. Results for different t_c are shown in Fig. 6.1 by the grey lines. For short times the number fluctuations decrease, but become frozen at some point. Thus, at a time scale $\tau_\kappa = 1/\kappa N$ one obtains always some amount of squeezing, but quasi-adiabatic splitting is a very inefficient process. In order to get highly number squeezed states, very long splitting times would be required.

6.2 Optimized splitting

We thus turn to optimized splitting sequences in order to obtain number squeezing more efficiently [67, 41, 68]. We start by applying OCT to the generic two-mode model of Eq. (3.24). From this model we learn about the general physical mechanisms which allow for more squeezing at a given splitting time. However, this model lacks an experimentally accessible control parameter as soon as the condensates start to oscillate. In contrast, for MCTDHB the control parameter is the splitting distance of the double-well potential. Therefore, we apply OCT also to this model.

6.2.1 Generic model

The cost functional for the optimization reads

$$J(\mathbf{C}, \Omega) = \langle \mathbf{C}(T) | \hat{J}_z^2 | \mathbf{C}(T) \rangle + \frac{\gamma}{2} \int_0^T (\dot{\Omega})^2 dt \,, \tag{6.1}$$

The first term is proportional to the number squeezing at the final time T, which we want to be small. Two control strategies could be identified using OCT [41], which we name after the relevant regime of the ratio Ω/κ, see Sec. 3.3.

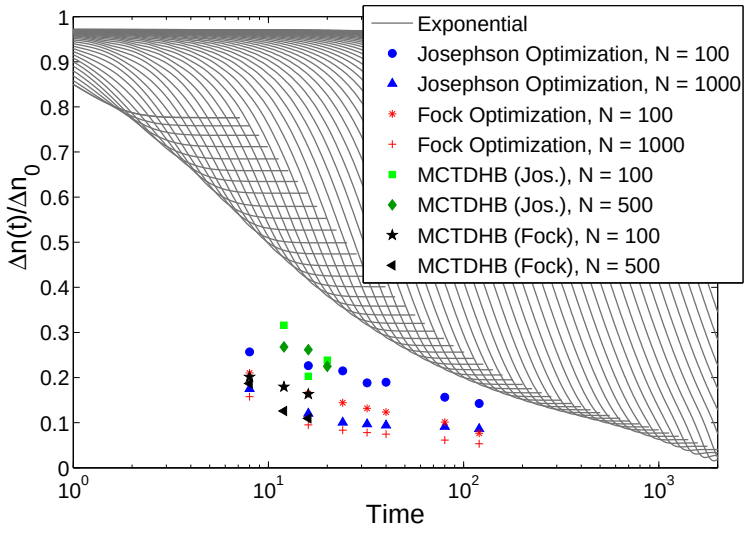

Figure 6.1: Comparison of quasi-adiabatic exponential (grey lines) and optimized splitting (symbols) for the generic model as well as for MCTDHB. OCT outperforms adiabatic splitting by 1-2 orders of magnitude in time. Interactions are such that $U_0 N = 1$.

Josephson solutions

For this type of solutions an oscillatory tunnel coupling, which is on the same size as the nonlinear interactions $\Omega \sim \kappa$, induces rotations of the state around the x axis of the Bloch sphere [67, 41], see Fig. 6.2 (a). While rotating, the state becomes squeezed. This rotation lasts for several periods and leads to oscillations in the number fluctuations, which finally become very small such that the system ends up in a highly squeezed state, see Fig. 6.2 (c). The underlying physical control mechanism can be ascribed to *parametric amplification*, which is a nonlinear driven process [69]. From a simple model, that we describe in more detail in [41], we can find the resonance condition $\omega_{res} = \kappa N + \Omega_0$ determining the oscillation period and the decrease of the envelope of the number fluctuations,

$$(\Delta n)_{envelope} \sim \Delta n_0 \exp\left[-\frac{\kappa N \Omega_1}{2(\Omega_0 + \kappa N)} t\right] , \tag{6.2}$$

shown by the bright lines. Compared to quasi-adiabatic exponential splitting, it is approximately one order of magnitude faster such that the same squeezing can be obtained on much shorter time scales (blue symbols in Fig. 6.1).

Fock solutions

For this case, the control is very small most of the time $\Omega \ll \kappa$, and has sometimes bumps, see Fig. 6.2 (d) (lower panel) [41]. It can be understood by means of the *constant control* scheme of Law *et al.* [70]. They proposed to complement the *one-axis twisting* model of Kitagawa and Ueda [9] by a constant tunnel coupling, see Fig. 6.2 (b): A condensate in a coherent state which is subject to phase diffusion is twisted around the z-axis on the Bloch sphere as indicated by the arrows. After some time, spin squeezing is created along a slant direction with respect to the equator. If tunnel coupling is finite, it manages to turn the state back to the equator such that the squeezing is transformed into number squeezing. In fact, we have shown in [41] that a *two-parameter model* can give rise to high squeezing. Thereby, we parametrize the control as

$$\Omega(t) = \Omega_0 \left(1 - \frac{\Omega_c}{\Omega_0}\right) e^{-t/t_c} + \Omega_c \, . \tag{6.3}$$

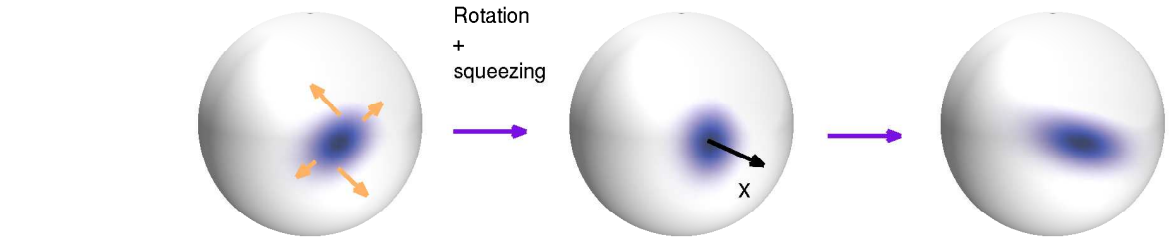

(a)

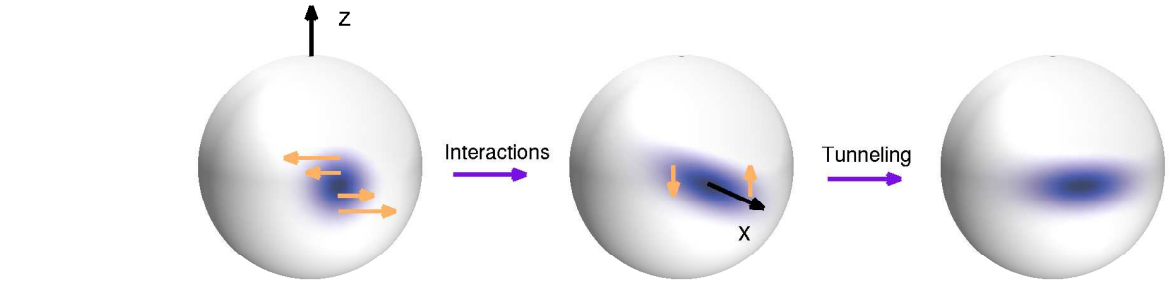

(b)

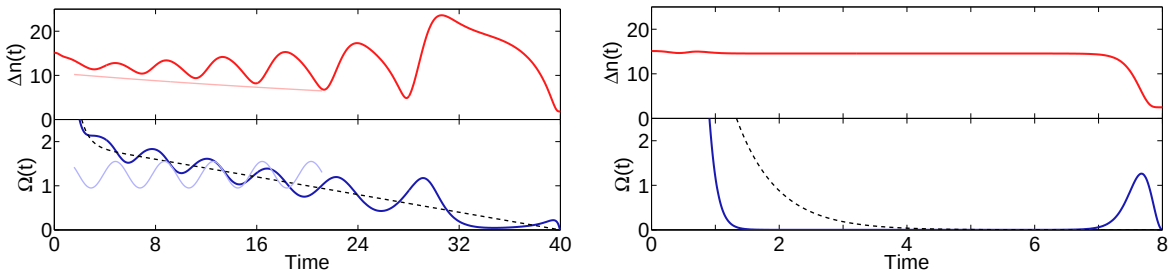

(c) (d)

Figure 6.2: (a) Demonstration of the control mechanism of *Josephson* type. A tunnel coupling which oscillates at a definite resonance frequency makes the state rotate around the Bloch sphere such that it becomes squeezed. (b) Demonstration of the control mechanism of *Fock* type. According to the one-axis twisting model a coherent state becomes squeezed due to interactions along a given direction. By allowing for tunneling, the state can be rotated a bit around the x axis such that it is number squeezed. (c) Typical example for Josephson OCT. Upper panel: Number fluctuations of the OCT control. Lower Panel: Optimized time variation of the tunnel coupling (solid line) and initial guess (dashed line). The bright lines show estimates from a simple model. (d) Same as (c) but for Fock OCT. Parameters are $U_0 N = 1$ and $N = 100$.

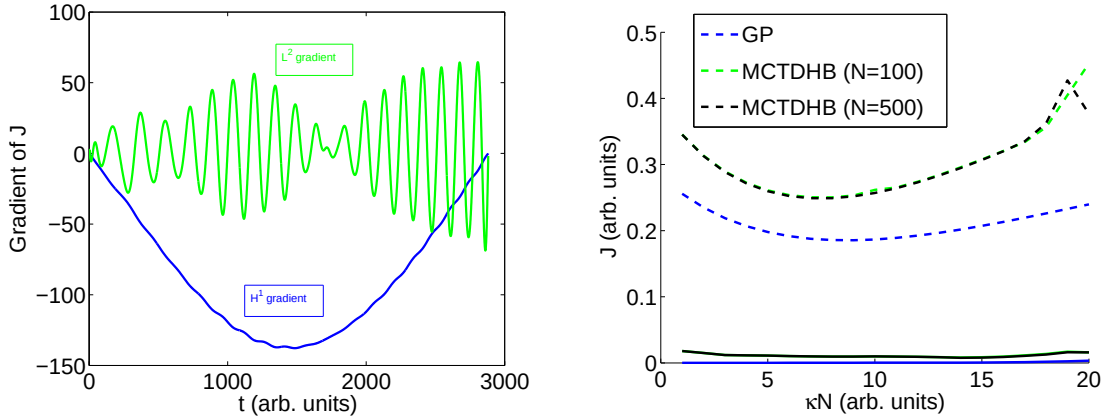

(a) (b)

Figure 6.3: Details for OCT. (a) Comparison of L^2 gradient $\nabla \hat{J}_{L^2}$ and H^1 gradient $\nabla \hat{J}_{H^1}$ for a typical OCT splitting example within MCTDHB. (b) Comparison of trapping controls for splitting a BEC within GP and MCTDHB. OCT is applied to the GP equation and evaluated for both GP and MCTDHB (solid lines), and compared to linear splitting (dashed lines). The cost functional J is plotted versus interaction strength.

By applying a simple parameter optimization method, we can determine the best possible values of the constant tunnel coupling Ω_c and the time scale of the splitting t_c. Fock OCT can be regarded as a generalization of this model, and performs somewhat better.

6.2.2 Optimizing number squeezing within a realistic model

We now turn to optimization of MCTDHB, which allows to determine optimal time variations of the trapping potential. It is parametrized by the control parameter λ directly accessible in experiment. For this we combine the optimization of the generic model with the trapping of the condensates in stationary states at the final time, which has already been carried out by Hohenester *et al.* [23] in context of the GP equation. The latter is important in order to avoid condensate oscillations at the end of the control interval, which will be analyzed more deeply in chap. 7. The cost functional containing both control goals reads

$$\begin{aligned} J(\phi_g, \phi_e, \mathbf{C}, \lambda) &= \frac{\gamma_1}{2}\langle \mathbf{C}(T)|\frac{\Delta\hat{N}^2}{4}|\mathbf{C}(T)\rangle + \frac{\gamma_2}{2}[2 - |\langle\phi_g(T)|\phi_g^d\rangle|^2 - |\langle\phi_e(T)|\phi_e^d\rangle|^2] \\ &\quad + \frac{\gamma}{2}\int_0^T \left[\dot{\lambda}(t)\right]^2 dt\,, \end{aligned} \tag{6.4}$$

where ϕ_g^d and ϕ_e^d are the desired stationary orbitals in which we want to trap our orbitals. $\Delta\hat{N}$ is the number difference operator for MCTDHB, see Chap. 7. The details of the derivation and implementation of the control system are given in [41] and in App. B.

When optimizing, we experienced a very different behaviour for the usual L^2 based optimization approach, and the newly developed H^1 based optimization [64]. We compared these two approaches in Chap. 5 and found for the H^1 approach, that local variations in the state are distributed globally onto the gradient. This is very relevant for MCTDHB since the orbitals depend sensitively on small trap variations. A comparison in Fig. 6.3 (a) shows very clearly that within L^2 only small oscillations are added to the control, whereas it is modified globally within H^1.

Josephson type controls are obtained from the usual L^2 based optimization approach, see Fig. 6.4 (a) [67, 41]. The control as well as the number fluctuations show an oscillatory behaviour

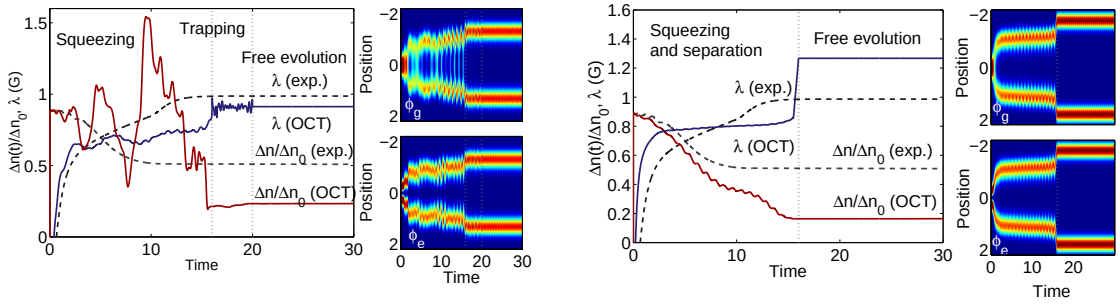

(a) (b)

Figure 6.4: Typical OCT splitting results for MCTDHB. Left panels: OCT tunnel coupling and number fluctuations (solid lines), compared to exponential splitting (dashed lines). Right panels: Corresponding orbitals. (a) The *Josephson* control oscillates, as well as the number fluctuations. (b) The *Fock* control is smoother, and the orbitals oscillate less than for the Josephson control. Parameters are $U_0 N = 1$ and $N = 100$.

typical for parametric amplification. An additional control sequence, where exclusively trapping is applied ($\gamma_1 = 0$), is necessary here. The final squeezing is similar to that from the generic model, see Fig. 6.1.

Fock type controls are obtained when employing the H^1 based optimization approach, see Fig. 6.4 (b) [41]. We compare optimization results in Fig. 6.1. While Fock-OCT produces better squeezing results than Josephson-OCT, the useful squeezing ξ_R is very similar for both methods (not shown). Whereas the control is very noisy within the L^2 based approach, the controls are smoother for the H^1 approach. Within MCTDHB, a *two-parameter* optimization, which worked quite well for the generic model, is not possible in general, since condensate oscillations limit the time scale of the splitting t_c, and it is very difficult to decouple and separate condensates after a "constant" control sequence.

6.2.3 Trapping: GP vs MCTDHB

At the end we investigate whether trapping controls for splitting a BEC evaluated within GP by Hohenester *et al.* [23] are valid also for the more exact MCTDHB(2). We take typical splitting ramps and evaluate the time dynamics associated with a non-optimized control, and a control which has been optimized within GP. This is done for both GP and MCTDHB(2). Results for the final cost are shown in Fig. 6.3 (b). We find that deviations between the models are smaller for optimized than for non-optimized solutions. The final cost for OCT and MCTDHB is worse than that for GP, however, still quite small. The effects of the condensate fragmentation, properly described within MCTDHB, are not very big for the optimal control.

Chapter 7

Stability and fragmentation of non-equilibrium Bose-Einstein condensates

We now turn our attention to the oscillations in our OCT control fields [71], see Fig. 6.4. What is the role of self-consistent orbitals? How wildly can a condensate oscillate before it fragments? And what is the appropriate theoretical description of a non-equilibrium condensate? Our splitting scenarios constitute prototypical examples for bosonic Josephson physics, as they rely on a condensate dynamics which is (moderately) out of equilibrium. We expect similar physics for other situations like the Shapiro effect [72]. Furthermore, number squeezing is a prototypical observable which depends on higher correlations. To investigate this, we started a collaboration with A. Scrinzi (formerly Photonics Institute, TU Vienna, now Arnold-Sommerfeld Center for Theoretical physics, LMU Munich), who performed MCTDHB simulations with more than two modes. We choose as examples our Josephson OCT solutions from Chap. 6 [67, 41], as well as another splitting with a smooth, but fast ramp such that condensate oscillations are present.

In this chapter we first demonstrate in Sec. 7.1 that the full self-consistency of MCTDHB is needed for the splitting scenario. In Sec. 7.2 we first discuss the number squeezing operator for an arbitrary number of modes, then give the results from the $M > 2$ simulations, the behaviour of which we try to understand in the rest of this section. We then present the insight we have gained about the many-body dynamics. Finally, in Sec. 7.3 we discuss the consequences of the results on quantum control and two-mode approximations.

7.1 Comparison: GP-orbitals vs. MCTDHB-orbitals

In our simulations in Chap. 6 we have chosen a relatively small nonlinearity $U_0 N = 1$, where U_0 is the 1D interaction parameter. Naively, one might expect that the shape of the orbitals is thus mainly determined by the bare hamiltonian $\hat{h}$, and the nonlinearity only plays a role for the atom number distribution. To check this we performed additional simulations where we artificially neglect in Eq. (3.36) certain nonlinear contributions, namely the Gross-Pitaevskii-type terms of the gerade and ungerade orbital, and the cross terms (see Fig. 7.1). We find that both the nonlinearity due to the gerade orbital f_g^g and the cross term $\tilde{f}^e$ strongly alter the dynamics of the orbitals and of the number fluctuations. More specifically, the neglect of the cross terms leads from the very beginning to a totally different time evolution. For the unsplit trap, initially only the gerade orbital is significantly populated, and Eq. (3.36) approximately reduces to a Gross-Pitaevskii equation for ϕ_1 (corresponding to the lowest, gerade orbital) and a Bogoliubov-de Gennes type equation for ϕ_2 (corresponding to the second, ungerade orbital). In particular

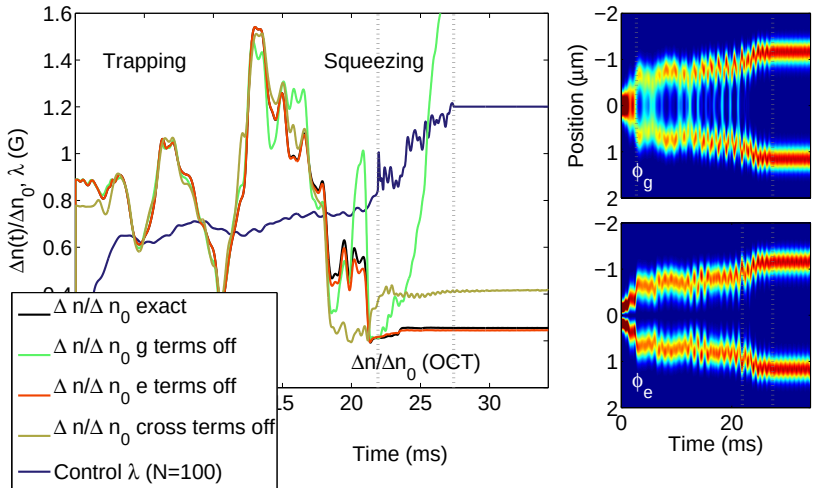

Figure 7.1: Results of our MCTDHB(2) simulations for two orbitals and for $N = 100$ atoms. We consider the situation where the condensate is split by transforming a single-well potential to a double-well potential. The control parameter $\lambda(t)$ determines the well separation. Oscillations of $\lambda(t)$ induce through parametric amplification oscillations in the number fluctuation $\Delta n(t)$ [67, 41], and the system becomes finally frozen in a state with a strongly reduced Δn. The main panel reports the time evolution of $\Delta n(t)$ for the control parameter $\lambda(t)$, and investigates the different contributions of Eq. (3.36) (for details see text). The panels on the left-hand side show the time evolution of the *gerade* and *ungerade* orbitals ϕ_1 and ϕ_2 for the full MCTDHB(2) simulations.

for the latter one, the cross term plays an important role, since it establishes a phase link to the condensate wavefunction. Without this contribution, ϕ_2 feels the condensate only through the density but the phase is not matched, which leads to fatal deviations once ϕ_2 becomes populated. Similar conclusions would hold for the bare orbitals (results not shown).

The neglect of the Gross-Pitaevskii type contribution for ϕ_g is less severe. We infer from the figure that the time evolution is initially very similar to that of the full simulation, and only at later times the $\Delta n(t)$ transients somewhat deviate. A striking feature is the *increase* of the number fluctuations at later times. In fact, at later time the two wells are spatially far separated, and one thus would not expect atom tunneling in this regime. We will return to this point later.

7.2 MCTDHB(M)

The above scheme can be readily generalized to more orbitals (see App. A), and, in the limit of many orbitals, provides the link to an exact description. The sensitivity to the coupling between the two orbitals raises the question, whether coupling to further orbitals could again change the results. Qualitatively, two orbitals are needed to capture the physics of number squeezing, as for a perfectly number squeezed state our representation must admit two independent wave BEC functions without any definite phase relation between them. However, the 2-orbital description might fail, if the dynamics of the separation of the condensate may involve excitations and condensate fragmentation.

In MCTDHB, the set of coefficients $\{C_{\vec{n}}\}$ and orbitals $\{\phi_k\}$ is not uniquely defined, but allows for unitary transformations (gauge freedom) [19]. For the special case of $M = 2$ calculations in symmetric traps, our orbitals are always natural orbitals due to the gerade - ungerade parity, but in general this is not true. However, we can always transform to natural orbitals by diagonalizing the one-body density ρ. In the following discussions we will always refer to natural orbitals, such

that the population of those orbitals corresponds automatically to the degree of fragmentation in the system [38].

7.2.1 Number squeezing operator

From the MCTDHB operator for number squeezing we learn about the contributions given by each orbital. Similar as we did for two orbitals in [41], we calculate the operator for detecting an atom on the left side as

$$\hat{N}_l = \int_{-\infty}^{0} dx \hat{\Psi}^\dagger(x,t)\hat{\Psi}(x,t) = N/2 + \sum_{i\neq j, i<j} \left(d_{ij}\hat{a}_i^\dagger \hat{a}_j + h.c. \right), \tag{7.1}$$

where i, j take values from 1 to M (and similar for $\hat{N}_r$). $\hat{\Psi}(x,t)$ is the standard boson field operator expanded in an arbitrary amount of modes, see Eq. (3.30). We used that the total atom number is constant, i.e., $\hat{N} = \sum_{i=1}^{M} \hat{a}_i^\dagger \hat{a}_i$. This expression depends on the off-diagonal operators $\hat{a}_i^\dagger \hat{a}_j$ acting on the state vector, as well as on the half-side overlap integrals of the orbitals

$$d_{ij} = \int_{-\infty}^{0} \phi_i^*(x)\phi_j(x)\, dx \, . \tag{7.2}$$

Taking into account the symmetry of the orbitals, our number difference operator is given by

$$\Delta\hat{N}/2 := (\hat{N}_l - \hat{N}_r)/2 = \sum_{i\neq j, i<j} \Delta\hat{n}_{ij} \, , \tag{7.3}$$

where we defined $\Delta\hat{n}_{ij} := d_{ij}^* \hat{a}_i^\dagger \hat{a}_j + h.c.$ This holds for a state which is symmetric around $x = 0$. The number fluctuations are then given by $\Delta n := \sqrt{\langle \left(\Delta\hat{N}/2\right)^2 \rangle} = \sum_{i\neq j, i<j} \Delta n_{ij}$, where Δn_{ij} are the contributions originating from each pair of orbitals.

We next discuss number squeezing for the ground state of a double-well. For typical interaction strengths, only the lowest gerade and ungerade orbitals are populated. All atoms in the lowest gerade orbital means $\Delta n_{12} = \sqrt{N}/2$. In terms of strictly localized modes $\phi_{l,r} = (\phi_1 \pm \phi_2)/\sqrt{2}$ ($\hat{a}_{l,r} = (\hat{a}_1 \pm \hat{a}_2)/\sqrt{2}$), it can be rewritten as

$$\Delta n_{12} = \frac{1}{2}\sqrt{\langle (\hat{N}_l - \hat{N}_r)^2 \rangle} = \frac{1}{2}\sqrt{\langle \hat{N}_r^2 + \hat{N}_l^2 - 2\hat{N}_r\hat{N}_l \rangle} \, . \tag{7.4}$$

This quantity essentially corresponds to the second order correlations between the two orbitals, i.e., correlations between number operators [69]. They change strongly when the ungerade orbital becomes slightly populated, since second order correlations are very sensitive to changes in the population difference. Similar statements hold for the second order correlations involving the higher orbitals. However, in this case it is important also to consider the factor d_{ij} in Eq. (7.1), which depends on the shape of the orbitals. For the ground state of a double-well, pairs of orbitals are approximately degenerate in shape, e.g., $|\phi_1| = |\phi_2|$. They are different only by a π-phase between the left and right parts. Since all the orbitals must be orthogonal, orbitals belonging to different gerade-ungerade pairs are orthogonal also within one well. Thus, whereas we have $|d_{12}| \approx 0.5$, $|d_{ij}|$ vanish for, e.g., $i = 1, 2$ and $j = 3, 4$ (and with it Δn_{ij}). This means that Δn_{12} is the only relevant contribution. Pairwise contributions of the higher orbitals as, e.g., Δn_{34}, are negligible, because the corresponding orbitals are not appreciably populated.

7.2.2 Number squeezing results

To check possible limitations of MCTDHB(2), we performed MCTDHB(M) calculations with up to M=6 orbitals. Because of the rather unfavorable scaling of MCTDHB(M) with M and with

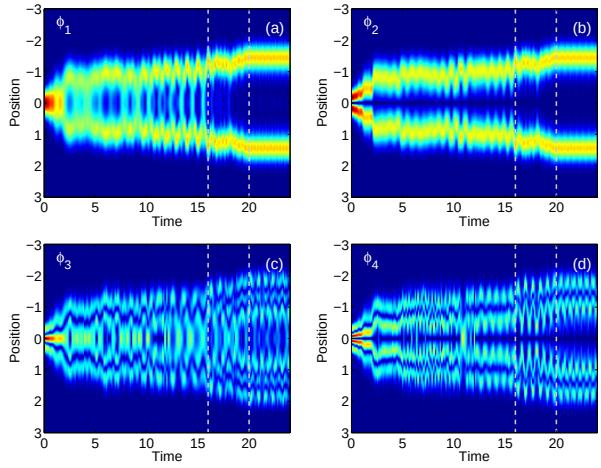

Figure 7.2: Natural orbitals (moduli) for the OCT control field for $M = 4$. The modes 1 and 3 have gerade, 2 and 3 ungerade symmetry. Higher modes have usually a more complex node structure, see (c) and (d). Parameters are $N = 50$ and $U_0 N = 1$.

the particle number N, we were limited to $N = 50$ particles for $M = 3, 4$, and $N = 30$ for $M = 6$ (not shown). Number squeezing is little affected by the exact particle number, if we keep only the non-linearity $U_0 N = 1$ constant. We therefore limit our discussion to particle number $N = 50$. The moduli of the natural orbitals of the OCT control field are shown in Fig. 7.2 for $M = 4$. We find that the importance of extra orbitals depends on the control field. For the OCT control [see Fig. 7.3 (a)] we see an interesting behaviour: during the control sequence, the exact number fluctuations Δn deviate temporarily quite appreciably from those of the two orbital calculations ($M = 2$), see Fig. 7.3 (c)). However, finally after the trapping OCT sequence, $M = 2$ yields the correct Δn as well. Thus, our squeezing results prevail. We compare to a different control field, see Fig. 7.3 (b)), which essentially induces oscillations in the condensates at the resonance frequency of parametric amplification, such that the number fluctuations also decrease. Then the further oscillating condensates are separated. We call this splitting scenario *oscillatory*. In contrast to the OCT case, for this control we find very different behaviour for $M = 2$ and $M = 4$. In fact, the number squeezing is much less for the more exact calculation, see Fig. 7.3 (d).

The question at hand is now, what discerns the two cases and why the number squeezing shows up such a nontrivial behaviour. The oscillations of the density, see Fig. 7.3 (a) and (b), seem to have a similar amplitude. The number of excitations which occur during splitting are shown in Fig. 7.3 (e) and (f). The populations of the third and fourth natural orbitals rise a bit, but stay overall two orders of magnitude smaller than the population of the second orbital. Moreover, these populations are comparable for the two cases. *Therefore we cannot draw any conclusions from the actual amount of excitations.*

More insight is obtained from the different contributions to the number squeezing operator as described in Sec. 7.2.1. We show in Fig. 7.3 (g) and (h) the half-sided overlap integrals from Eq. (7.2). We find that due to the dynamics, they appreciably deviate from the ground states. In particular, $|d_{12}|$ becomes smaller than one, whereas $|d_{14}|$ and $|d_{23}|$ become finite ($|d_{13}|$ and $|d_{24}|$ vanish due to parity). Hence, the reduced overlap $|d_{12}|$ diminishes Δn. However, this is compensated by the other contributions involving higher orbitals. This leads us to a very important findings: *Number squeezing might be underestimated if higher orbitals are neglected.* This does not depend so much on the total population of these orbitals, but much more on their specific shape. This becomes very clear when one compares the number squeezing in Fig. 7.3 (c), (d) with $|d_{14}|$ and $|d_{23}|$ in (g), (h). The $M = 2$ calculation (solid lines) deviates from the

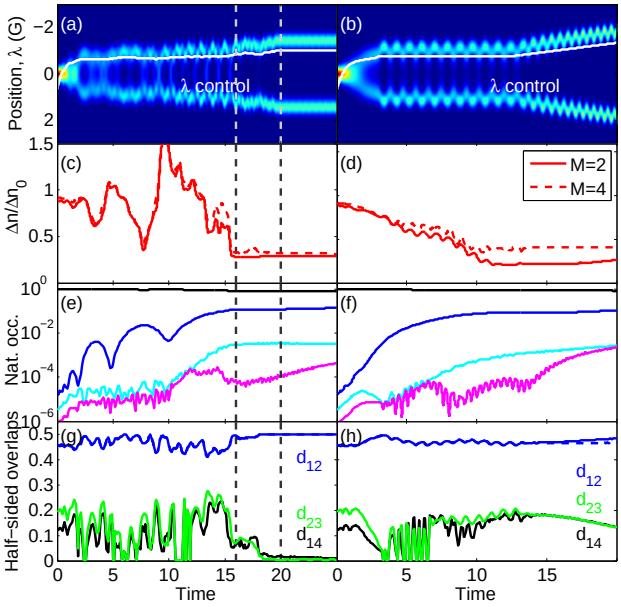

Figure 7.3: Two different splitting scenarios are shown: (left panels) *OCT* splitting, (right panel) *oscillatory* splitting. (a), (b) show the density and the corresponding controls. (c), (d) Number fluctuations for $M = 2$ and $M = 4$ are compared. (e), (f) The populations of the natural orbitals for $M = 4$. (g), (h) half sided overlap integrals from Eq. (7.2). Solid lines show results for $M = 4$, the dashed lines for $M = 2$. The horizontal dashed lines in the left panels separate the splitting, trapping, and free evolution stages of the OCT control. Parameters are $N = 50$ and $U_0 N = 1$.

$M = 4$ one (dashed lines) exactly at those times, where $|d_{14}|$ and $|d_{23}|$ are large. For instance, the OCT case has a deviation between $M = 2$ and $M = 4$ around $T = 20$, which corresponds to a maximum of $|d_{14}|$ and $|d_{23}|$. As soon as the orbitals are brought back to the ground states, $M = 2$ is more or less exact again. For the parametric case, deviations start at $T = 5$ (note that at very small times, i.e., for an unsplit trap, the density is finite at $x = 0$ and the finite $|d_{14}|$ and $|d_{23}|$ are rather an artifact from cutting the system into two parts). The deviations have a minimum at $T \approx 12$, and are very distinct after $T = 10$ again.

We note that the $M = 2$ calculation quite well describes the two lower modes. For example, $|d_{12}|$ from $M = 2$ [dashed lines in Fig. 7.3 (g) and (h)] is for a long time identical to the $M = 4$ one, and deviates only slightly towards the end in (b). Thus, the time evolution of the natural orbitals seems to be quite independent. We will come back to this point in context of OCT.

7.2.3 Localization

In order to understand how barely populated orbitals can contribute, it is very instructive to investigate number squeezing also in a strictly localized basis. This has the advantage, that the by far dominant contribution to number squeezing is due to the most populated localized orbitals, which are usually the lowest ones. This can be explained by using sets of localized orbitals $\{\phi_{l_i}\}$ and $\{\phi_{r_i}\}$, which are all mutually orthogonal. The transformation from natural orbitals to localized ones is schematically shown in Fig. 7.4. The atom number operator for measuring an atom on the left side is then simply given by $\hat{N}_l = \sum_i \hat{a}^\dagger_{l_i} \hat{a}_{l_i}$. When calculating expectation values, we can clearly neglect the small contributions of sparsely populated orbitals. Similar conclusions hold for the variance of this operator. Therefore, we have for the number squeezing

$$\Delta n = \sum_i \Delta n^{(i)}_{lr} \approx \Delta n^{(1)}_{lr} \ , \tag{7.5}$$

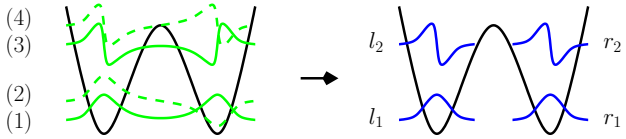

Figure 7.4: Schematics showing transformation from natural (left) to localized orbitals (right), for $M = 4$. The natural orbitals are labeled by $1, 2, 3, 4$, the localized ones are labeled by l_1, l_2, r_1, r_2.

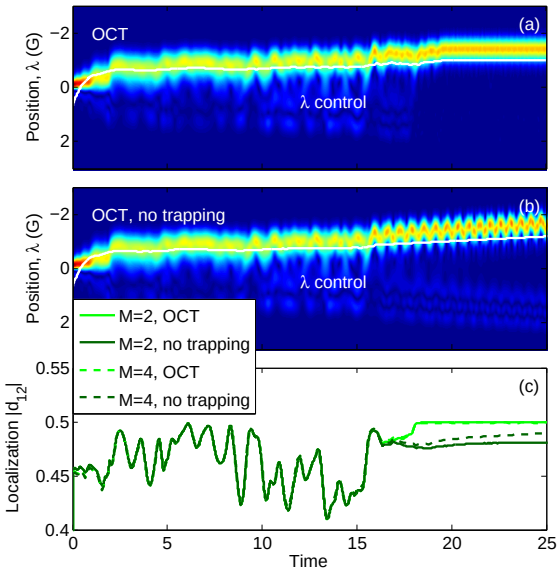

Figure 7.5: Best localized orbitals for $M = 2$ according to the transformation of Eq. (7.6) for the (a) OCT control, and (b) the OCT squeezing control where instead of the trapping sequence, the orbitals are separated by a linear ramp. (c) Comparison of $|d_{12}|$ for the OCT control with and without trapping, and for $M = 2$ and $M = 4$. Parameters are $N = 50$ and $U_0 N = 1$.

where $\Delta n_{lr}^{(i)}$ is the contribution due to each pair of localized orbitals.

We now turn to the explicit construction of the localized orbitals. We start with $M = 2$ and transform the orbitals according to

$$\phi_{l,r}^{loc} = (\phi_1 + e^{i\alpha}\phi_2)/\sqrt{2}\,, \tag{7.6}$$

We find that while localization can be achieved for the OCT case (see Fig. 7.5), this does not work for the oscillatory case (see Fig. 7.6). Note that the two lowest orbitals for the higher mode calculations are only slightly better in this respect, but overall very similar to the ones from $M = 2$ [see also Fig. 7.3 (h)]. Now the question is, if more modes could restore localization. Indeed, transforming four orbitals instead of two according to

$$\phi_{l_1,l_2,r_1,r_2} = (\phi_1 + e^{i\alpha_1}\phi_2 + e^{i\alpha_2}\phi_3 + e^{i\alpha_3}\phi_4)/\sqrt{4}\,, \tag{7.7}$$

yields for optimal α_i $(i = 1, 2, 3)$ two well localized modes for each side, see Figs. 7.6 (b) and (c). The localized mode ϕ_{l_1} in (b) is the dominant one, ϕ_{l_2} in (c) is only scarcely populated. From this we learn that the system needs enough degrees of freedom (modes), in order to describe the localized modes.

It is easy to understand why there must be corrections to number squeezing if the modes do not localize: As we have learned, more modes are needed for a proper local description, and transformed among themselves to yield localized orbitals. Hence, also the two lowest, predominately occupied localized modes depend on the higher natural orbitals, and therefore also the

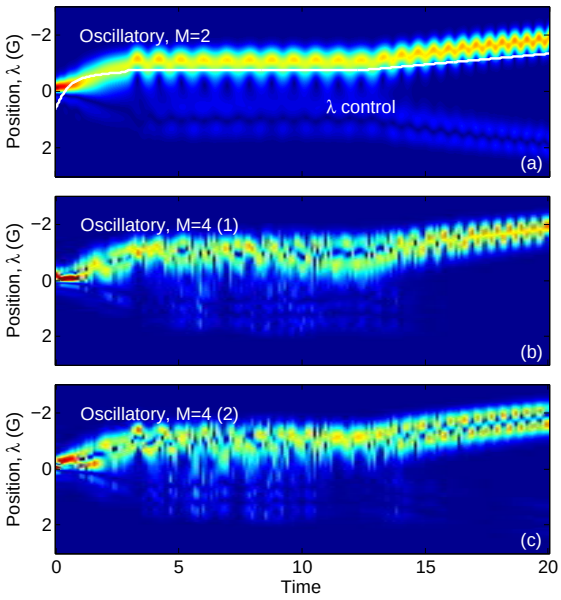

Figure 7.6: Best localized orbitals for *oscillatory* control for (a) $M = 2$ according to the transformation of Eq. (7.6), and (b), (c) $M = 4$ according to the transformation of Eq. (7.7). (b) corresponds to the strongly populated, (c) to the weakly populated localized orbital. Parameters are $N = 50$ and $U_0 N = 1$.

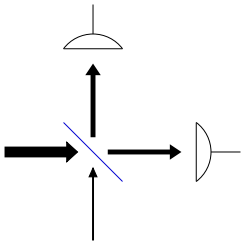

Figure 7.7: Sketch of homodyne detection: a strong field *local oscillator* is mixed with a weak signal. At the output ports, the phase or coherence properties of the signal can be detected.

number squeezing operator. In contrast, if the two lowest natural orbitals can be transformed into localized ones, this proves that two modes are enough to calculate number squeezing, even if there is small fragmentation. Hence, when localization is achieved, more modes are unimportant for number squeezing.

The contributions of the excitations to number squeezing can be viewed also in another way: Reconsidering the contributions to number fluctuations originating from each pair of localized orbitals

$$\Delta n_{ij} := \sqrt{\langle (d_{ij}^* \hat{a}_i^\dagger \hat{a}_j + h.c.)^2 \rangle} \,, \tag{7.8}$$

we can interpret this as the mixing of strong and weak components. This is analogous for example to homodyne detection in quantum optics [69], where a strong local oscillator is mixed using beam splitters with a weak signal, see Fig. 7.7. This allows to readout the phase or coherence properties of the weak signal. Number squeezing is a property between a left and a right system, which is connected to the localized orbitals in a similar fashion through a unitary ('beam splitter") transformation, see Eqs. (7.6) and (7.7), which makes it very sensitive to second order coherences.

7.3 Consequences for quantum control and two-mode approximations

7.3.1 Criteria for breakdown of the two-mode approximation

From the above reasoning we can conclude that a two-mode model based on the two lowest natural orbitals does not properly reproduce number squeezing, if they do not localize. In this case, more orbitals are needed. The localizability of the orbitals could be used as a signature to check if two modes are enough. Moreover, we find that, whenever the orbitals do not become localized, the continuity equation for particles is violated. We experience in fact that the number squeezing does not stay constant (see Fig. 7.3 (d), solid line), although the condensates are far separated and the density is zero for $x = 0$. However, when using more modes, this feature indeed disappears (dashed line). This unphysical behaviour can also be used as a criterion to check if the model is reasonable, and if it is probable that two modes are sufficient. *Thus, we have even within a two-mode approximation hints if the two-mode description is valid or not.*

7.3.2 Damping of excitations

For our OCT control field, we achieved complete trapping of the condensate in a stationary state, see Fig. 7.3 (g) [23, 67, 41]. This was due to a special control sequence between $T = 16$ and $T = 20$, which transfered the orbitals to their ground state shapes at the final time. What if we leave this out and choose a constant control? Best localized orbitals (Eq. (7.6)) from the cases with and without trapping are shown in Fig. 7.5 (a) and (b). As can be expected, without trapping the orbitals continue to oscillate and do not become localized. When considering number squeezing, we observe very bad convergence with the number of modes (not shown). The difference between the two cases is best represented by the amount of localization of the two lowest modes $|d_{12}|$, see Fig. 7.5 (c). During the whole splitting sequence, localization is bad due to the rapid condensate oscillations, which can be considered as coherent (spatial) excitations. We found this also to be accompanied by slight fragmentation (or depletion) of the condensates in the wells, i.e., incoherent excitations into higher modes. As a combined effect of both types of excitations, additional number squeezing was been found temporarily. From this we conclude that, if we bring the orbitals to stationary states, we practically erase the effect of the excitations. Of course the fraction of excited atoms, which is here quite small, still exists, but does not contribute to number fluctuations anymore.

Although the trapping optimization was performed within $M = 2$, it still works within $M = 4$. This is explained by the observation, which we already indicated above, that the two lower lying orbitals of a converged calculation and the corresponding orbitals for $M = 2$ are identical for a long time. Thus, the excitations behave *linear response* like, i.e., they do not affect the condensates. Only after a long time (here $T > 20$), the condensates start to feel the excitations. *Thus, excitation-induced number squeezing is reversible and can be suppressed, in many cases, by trapping.*

7.3.3 Choice of the control

What have we learned about possible controls of the system? Considering the *oscillatory* control field from above, we made the experience that it is quite hard to apply trapping in this case. This is not only because there are stronger oscillations, but because the splitting is larger during the control sequence. It turned out that far split condensates are much harder to trap. This is because the densities of the split condensates behave each as a single condensate with a first excited (ungerade) state admixture (see Fig. 7.3 (b), upper panels). However, trapping of an ungerade state into the (gerade) ground state works only at a much longer time than the trapping

of excitations with equal parity, which is predominantly the case for less split traps. Therefore, controls with less splitting are desirable.

We have seen that the coherent (mean field) excitations lead after some period of time to a depletion of the condensates. After $\sim$ 10 ms the incoherent excitations start to disturb the condensates, which leads to a complete breakdown of the two-mode approximation. Hence, the control should be such that the amount of time the density is allowed to oscillate is limited.

Chapter 8

Atom interferometry in presence of interactions

It is an important task to take nonlinear atom-atom interactions into account during the whole interferometer sequence [73]. In many trapped BEC experiments, Feshbach resonances [74] are not available. For example, Rubidium condensates on atom chips are on one hand the most promising tools in terms of controllability and miniaturization, however, the Feshbach resonances in Rubidium are very narrow, and it is also difficult to apply additional magnetic fields in magnetic traps.

For two types of interferometers, we discuss in the following [73, 75]

1. the phase sensitivity for the case of interactions present, as well as the
2. ideal input states and the
3. state preparation using our tools from OCT applied to MCTDHB.

8.1 Time-of-flight interferometer

8.1.1 Phase diffusion

In presence of interactions, the interferometer transformation reads

$$|\psi_{OUT}\rangle = e^{-i\theta \hat{J}_z} e^{-iU_0 T_{\mathrm{p}hase} \hat{J}_z^2} |\psi_{1N}\rangle \,, \tag{8.1}$$

where $T_{\mathrm{p}hase}$ is the phase accumulation time. Generally, interactions have the effect of twisting the state around the z axis of the Bloch sphere, which increases the phase fluctuations of a given state, as well as decreases its phase coherence. For example, a coherent state with phase θ obtains extra phase factors, which depend on the relative atom number of the state:

$$|\phi\rangle = \frac{1}{2^{N/2}} \sum_k \binom{N}{k} e^{i\phi k} |k\rangle \rightarrow |\phi(t)\rangle = \frac{1}{2^{N/2}} \sum_k \binom{N}{k} e^{i(\phi k - U_0/4k^2 t)} |k\rangle \,. \tag{8.2}$$

This diffuses the phase, the rate of this broadening is proportional to the number fluctuations of the state [76]

$$R = 8U_0 \Delta n = 8U_0 \xi_N(\sqrt{N}/2) \,. \tag{8.3}$$

Thus, phase diffusion has very different effects on different initial states as shown in Fig. 8.1. Therefore, one encounters a trade-off: number squeezed states are very robust against phase diffusion, while at the same time they are accompanied by large phase fluctuations. In contrast,

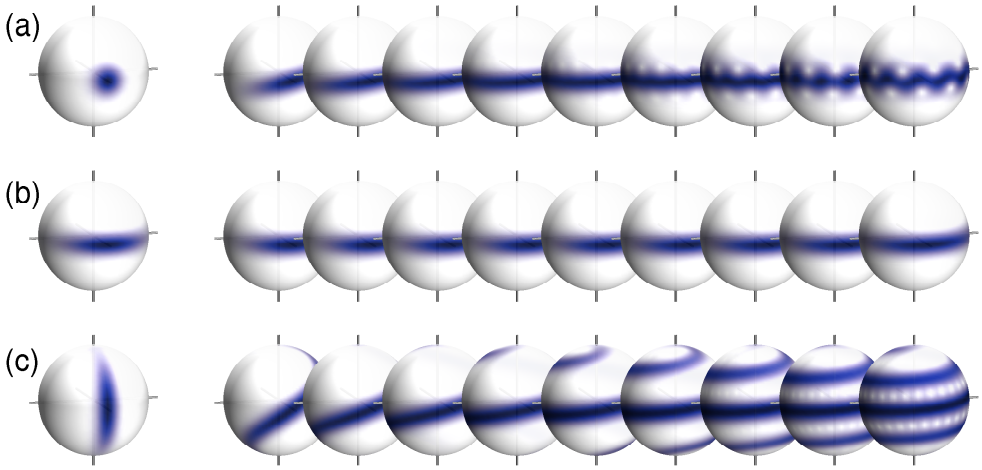

Figure 8.1: Phase diffusion for a coherent, a number and a phase squeezed state.

	Coherent	Number squeezed	Phase squeezed
Phase diffusion	average	slow	fast
Phase sensitivity	shot noise	above shot noise	below shot noise

Table 8.1: Comparison of the properties of coherent, number and phase squeezed states. The phase sensitivity refers to the non-interacting (ideal) interferometer.

phase squeezed states have large Δn and experience thus a very rapid phase diffusion. Therefore, it is very difficult to exploit their appealing notion of high phase sensitivity. Neither of the desired properties possesses the coherent state, which has equal number and phase fluctuations. We summarize the properties of coherent, number and phase squeezed states in Table 8.1.

8.1.2 Ideal input states

Optimal number squeezing

When asking which input state is best [73], it will depend on the given phase accumulation time. We plot ξ_R, which corresponds to the phase sensitivity, versus time for the three kinds of states in Fig. 8.2. While at very short times the phase squeezed state gives best sensitivity, the most stable state is the number squeezed one. We first ask for the ideal degree of number squeezing of the initial state. The longer the phase accumulation time T_{phase}, the more number squeezing is

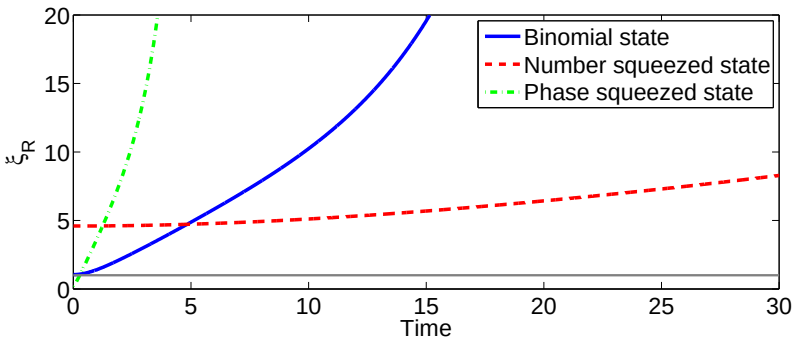

Figure 8.2: Phase sensitivity versus time for a coherent, a number and a phase squeezed state.

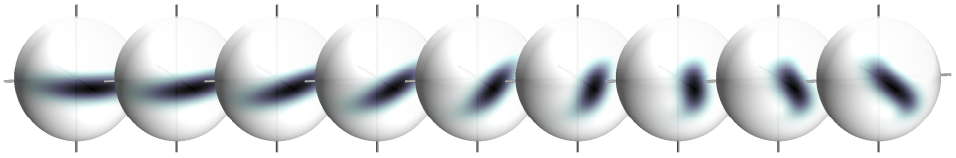

Figure 8.3: Example for a *refocusing* sequence on the Bloch sphere. An initially number squeezed state is rotated such that it refocuses after a given time into a phase squeezed state.

required. Approximately, we obtain

$$\xi_N^{min} = 1/(2\sqrt{U_0 N T_{\mathrm{p}hase}})\,, \tag{8.4}$$

and for the phase sensitivity

$$\xi_R = 2\sqrt{2U_0 T_{\mathrm{p}hase}}\,. \tag{8.5}$$

When measuring a potential gradient ΔE, which is related to the phase as $\theta = \Delta E T_{\mathrm{p}hase}$, the smallest detectable potential scales as $\Delta E^{\mathrm{m}in} \sim 1/\sqrt{T_{\mathrm{p}hase}}$ such that one can enhance sensitivity to the potential ΔE by increasing the phase accumulation time.

Refocusing

In order to reach also a sub-shot noise phase sensitivity, we allow for more general input states: In particular, it is very helpful to choose a squeezing along a direction parametrized by an angle ϕ_{tilt} and given by $\hat{J}_{\phi_{tilt}} = \cos\phi_{tilt}\hat{J}_z + \sin\phi_{tilt}\hat{J}_y$. We refer to this strategy, where an initially number squeezed state becomes tilted by a given angle, as *refocusing*. The tilt can be achieved by rotating a number squeezed state by a *tunnel pulse*. This is, achieved by a finite tunnel coupling for a given amount of time: $\phi_{tilt} = \Omega_{tilt} T_{pulse}$. A typical control sequence, consisting of a (i) tunnel pulse and (ii) refocusing, is shown in Fig. 8.3 on the Bloch sphere. A systematic analysis consists in optimizing the two parameters of (i) initial number squeezing ξ_N and (ii) tilt angle ϕ_{tilt}. This strategy works best for higher atom number (with $U_0 N$ constant), and results in an order of magnitude longer phase accumulation times at the same sensitivity compared to not using the refocusing strategy.

Optimizing trapping potential and atom number

The phase diffusion rate is approximately proportional to a mean confinement length $\omega_0 = \sqrt{\omega_x\omega_y\omega_z}$. We can reduce it by choosing asymmetric configurations like *elongated* (1D) or *pancake shaped* (2D) configurations with confinement ratios $C_{1D} = \frac{\omega_z}{\omega_\perp}$ and $C_{2d} = \frac{\omega_{plane}}{\omega_\perp}$, respectively. Therefore, small aspect ratios $C_{1D}, C_{2D} \sim 1/1000$ will reduce the effective interactions strength in the direction of strong confinement to values of $U_0 N = 0.1$ and $U_0 N = 0.01$, respectively. In combination with our refocusing strategy, this allows for distinctly sub-shot noise interferometry far below the standard quantum limit.

The dependence on the atom number N is analyzed taking into account the confinement ratio. We find that $\xi_R \sim N^{1/5}$, which yields a decrease of sensitivity by a factor of 3 when the atom number increases from 1000 to 10000. When using refocusing, however, the increase becomes insignificant, such that large atom numbers work as well. For the absolute signal sensitivity we find improvement with N and $T_{\mathrm{p}hase}$,

$$\Delta E^{\mathrm{m}in} \sim N^{-1/3} T_{\mathrm{p}hase}^{-1/2}\,. \tag{8.6}$$

The gain in $\Delta E^{\mathrm{m}in}$ when using refocusing is an order of magnitude.

Concerning additional quantum decoherence introduced by the asymmetric geometries, we conclude that this is no problem at our time scales for small enough temperatures.

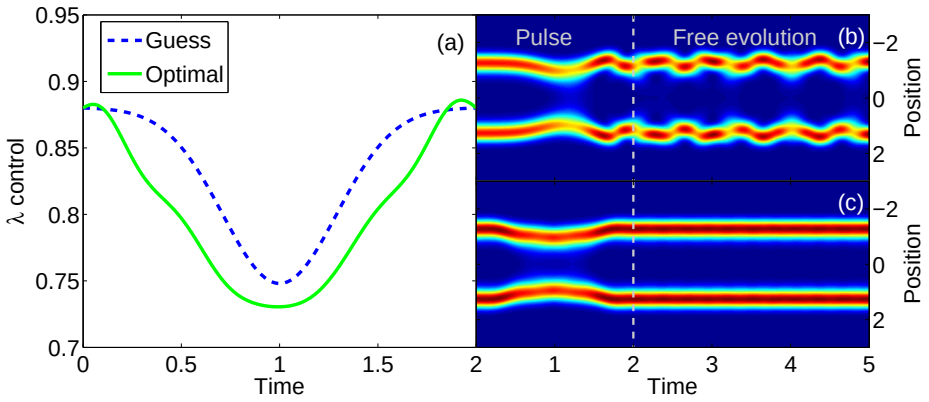

Figure 8.4: Typical control for refocusing for $U_0N = 0.1$ and $N = 100$. We compare an initial guess with an OCT solution. The (a) controls, (b) non-optimized and (c) optimized densities are shown (the corresponding phase squeezing is not shown, we refer to [73]). The control is to achieve a tunnel pulse and in addition stationary orbitals at the final time.

8.1.3 State preparation

The preparation of number squeezed states by splitting a condensate within realistic confinement potentials has been subject to the first part of this thesis. We note that very small interactions, as is desirable for reducing phase diffusion, results in very long splitting times to achieve the desired amount of number squeezing.

For the preparation of tilted states we considered to produce them from number squeezed states and to apply a finite amount of tunnel coupling [73]. This operation gradually transforms number- into phase squeezing. For $\pi/2$-tunnel pulses, this process is referred to as 'cold-atom beam splitter' [51]. In real space, initially separate condensates have to be brought together to some extent, such that atoms are allowed to tunnel. We have to achieve the desired pulses as fast as possible, since the interactions degrade the quality of the prepared states. This is difficult, because the condensates may start to oscillate and excitations created. We employ OCT of MCTDHB to find controls for a achieving giving tunnel pulses. In the optimization we require a fixed amount of phase squeezing ΔJ_y^d at the final time T. The cost functional reads

$$\begin{aligned} J(\phi_g, \phi_e, \mathbf{C}, \lambda) &= \frac{\gamma_1}{2}\left(\Delta J_y^d - \langle \mathbf{C}(T)|\hat{\tilde{J}}_y^2|\mathbf{C}(T)\rangle\right)^2 \\ &\quad + \frac{\gamma_2}{2}[2 - |\langle\phi_g(T)|\phi_g^d\rangle|^2 - |\langle\phi_e(T)|\phi_e^d\rangle|^2] + \frac{\gamma}{2}\int_0^T \left[\dot{\lambda}(t)\right]^2 dt\,, \end{aligned} \tag{8.7}$$

where $\hat{\tilde{J}}_y$ is the phase squeezing operator for MCTDHB, see App. B.2. Shortest pulses have been achieved for relatively weak interactions $U_0N = 0.1$ for $T_{\text{pulse}} = 2$. Optimization is more difficult for stronger interactions $U_0N = 1$ for $T_{\text{pulse}} = 4$. A typical result is shown in Fig. 8.4.

8.2 Mach-Zehnder interferometer

The ideal Mach-Zehnder interferometer has been introduced in Sec. 4. The error propagation formula suggests that coherently number squeezed states ($\xi_R = \xi_N/\alpha < 1$) give sub-shot noise Heisenberg interferometry. More generally, the Cramer-Rao lower bound (Eq. (4.19)) tells us that the ideal input state is a Fock state $|N/2\rangle_L|N/2\rangle_R$ [77, 53, 54]. Thus, depending on the experimental possibilities or circumstances, one could prepare highly squeezed number states using our OCT protocols, or take independent condensates as input states. Two cold atom

beam splitting operations are necessary for the MZ. Without atom-atom interactions during the interferometer performance, this seems to be rather unproblematic if performed sufficiently slowly.

In the following work, which has been performed during research stays at the INO-CNR BEC center in Trento in the group of A. Smerzi, we aim at including the interactions during the whole interferometer sequence [75]. We visualize a typical interferometer on the Bloch sphere in Fig. 8.5. The state becomes distorted and spoils the argument of enhanced sensitivity by reduced number fluctuations of the final state. Thus, the interactions have to be tuned to far below $U_0 N = 0.1$,

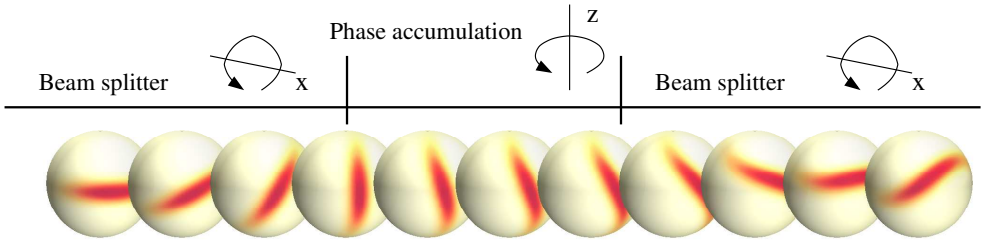

Figure 8.5: Mach-Zehnder interferometer sequence on Bloch sphere in presence of interactions. Even very small interactions $U_0 N = 0.1$ spoil the MZ.

which is very hard to achieve without employing Feshbach resonances (at least in 1D geometries or for large N, see Sec. 8.1.2).

8.2.1 Phase sensitivity

We proceed now with a more profound analysis of the phase sensitivity of the MZ in presence of interactions. The interferometer sequence reads

$$|\psi_{OUT}\rangle = e^{-iU_0 T_{pulse}\hat{J}_z^2 + i\pi/2\hat{J}_x} e^{-i\theta T_{phase}\hat{J}_z - iU_0 T_{pulse}\hat{J}_z^2} e^{-iU_0 T_{pulse}\hat{J}_z^2 + i\pi/2\hat{J}_x} |\psi_{IN}\rangle \,. \tag{8.8}$$

Because we do not have a simple $e^{i\hat{J}_{\vec{n}}\theta}$ interferometer anymore, where analytical quantum bounds are known, we proceed with numerical methods.

Bayesian analysis—For a numerical simulation of Bayesian phase estimation we need to calculate first the conditional probabilities $P(n|\theta) = |\langle n|\mathbf{C}_\theta\rangle|^2$, where $\mathbf{C}_\theta$ is the final state vector. It is plotted in Figs. 8.6 (d-i), for a coherent, a number and a phase squeezed state. The Bayes formula Eq. (4.24) requires inverting the conditional probabilities - we use our knowledge gained from a measurement, n, and assign the probability $P(\theta|n)$ to each value of θ. Whereas $P(n|\theta)$ corresponds for given n to a vertical cut in Figs. 8.6 (d-i), for a fixed θ, $P(\theta|n)$ corresponds to a horizontal cut (apart from a normalization). We find that for the coherent and moderately number squeezed states, the probability distributions have a Gaussian shape. For the squeezed state, it is narrower, which leads to the sub-shot noise sensitivity in case of the ideal MZ. However, when interactions are present, the Gaussians become very broad. This holds even more for the squeezed state. When looking at the Fock state, it has a single peak at the center ($n = 0$, $\theta = 0$), and some other regular structure. The effect of interactions is to induce a very complex structure. Therefore, while for the coherent and number squeezed states the conditional probability distributions become strongly washed out, a new structure emerges for the Fock state.

By simulating measurement outcomes for $\theta = 0$, we can find the Bayesian probability. This is shown in Figs. 8.7 (a-f). After $p \sim 20$ the result converges to $\Delta\theta = 1/\sqrt{p}N$ [see Fig. 8.7 (g)], which implies a Heisenberg scaling with the total number of atoms $N_T = pN$, with constant prefactor $\sqrt{p}$. Indeed, the complex structure present in Fig. 8.6 (i) gives, for a large enough number of measurements p Heisenberg limited interferometry.

Now we proceed with the calculation of the phase sensitivity by means of the classical Fisher information Eq. (4.15). We evaluate $F(\theta)$ for different interactions strengths $U_0 N$ and number

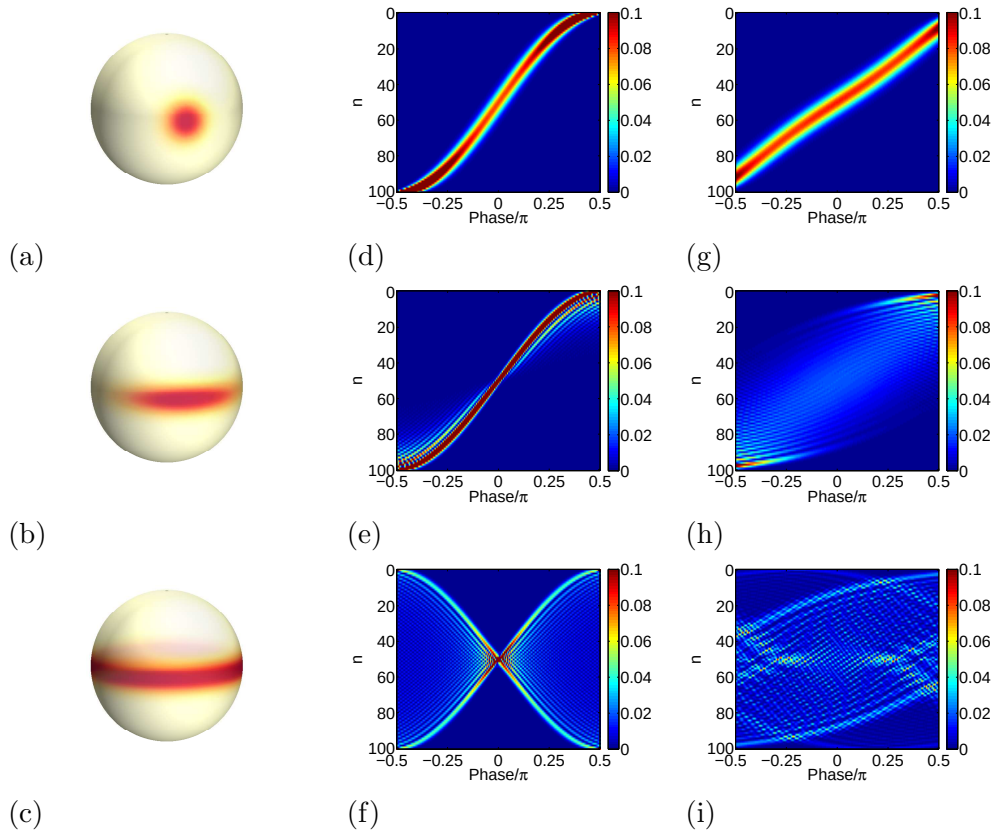

Figure 8.6: Numerical evaluation of the probabilities $P(n|\theta)$ for (a) a coherent, (b) a moderately number squeezed and (c) a Fock state. The ideal case (no interactions) is shown in (d-f). Interactions in (g-i) are $U_0N = 1$ and $N = 100$. For the coherent and number squeezed states, the probability distributions are Gaussian and become much wider whenever interactions are present. The more complicated structure in the probability distribution of the Fock state becomes modified due to interactions, but is not washed out, in contrast to the coherent and number squezzed states.

squeezing factors ξ_N, and plot the phase sensitivity $\Delta\theta = \frac{1}{\sqrt{F(\theta)}}$ in Fig. 8.8 (a). For the ideal case, we find a monotonous decrease of $\Delta\theta$ with the number squeezing. For the Fock $|N/2\rangle|N/2\rangle$ state where half of the atoms occupy the left well, and the other half the right well, we find a sensitivity of approximately $\Delta\theta = \sqrt{2}/N$. When turning on interactions, starting from the coherent state ($\xi_N = 1$) we find a decrease of sensitivity with ξ_N. This is what one expects: interactions seem to spoil the MZ as implied by Fig. 8.5. However, we find that by further enhancing the degree of squeezing, at some point the phase sensitivity drops. For very small ξ_N, it approaches the Heisenberg limit. Thus, we observe here surprisingly a transition for varying number squeezing. We finally find that, even for typical interactions $U_0N = 1$, we stay almost at the Heisenberg limit. When further increasing interactions, we still have distinctly sub-shot noise phase sensitivity. In the examples given above we have seen that the phase sensitivity according to $\Delta\theta = 1/\sqrt{F(\theta)}$ can be fulfilled by a Bayesian phase estimation strategy.

How can we understand this transition? When a number squeezed state is subject to a cold atom beam splitter, components of high atom number imbalance become populated. These states can be very sensitive to phase differences. For example, for the NOON-state

$$|NOON\rangle = (|N\rangle_L|0\rangle_R + |0\rangle_L|N\rangle_R)/\sqrt{2} \quad \rightarrow \quad (|N\rangle_L|0\rangle_R + e^{iN\theta}|0\rangle_L|N\rangle_R)/\sqrt{2} \tag{8.9}$$

the phase shift becomes multiplied by N, which allows for Heisenberg limited sensitivity. At the

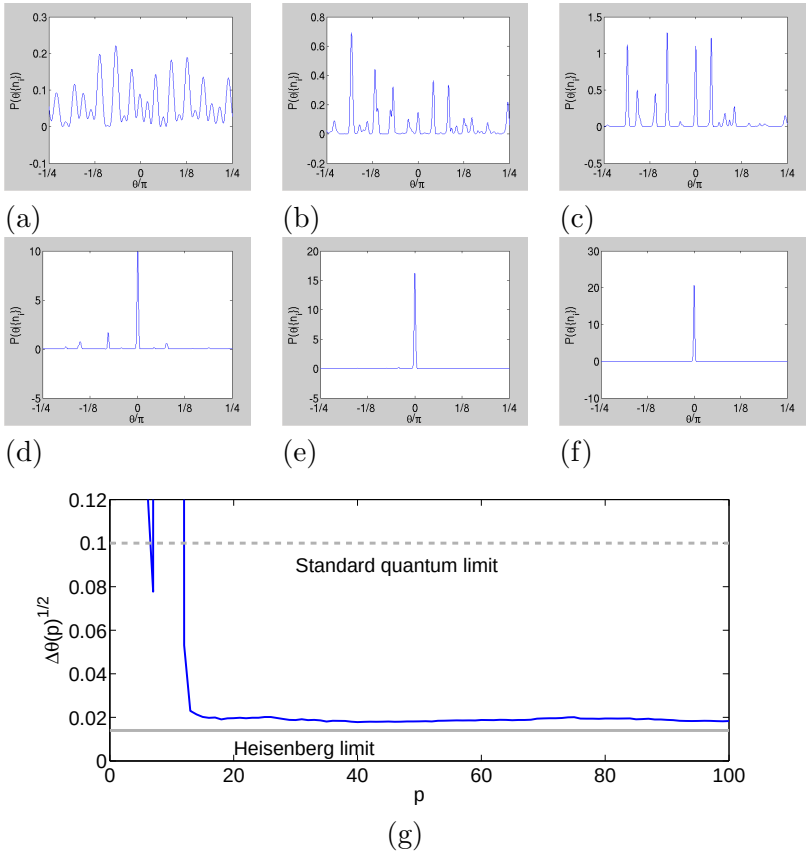

Figure 8.7: Simulation of Bayesian phase estimation. (a-f) We simulate a series of measurement outcomes (at $\theta = 0$) for an initial Fock state ($N = 100$, $U_0 N = 1$) and calculate the inverted Bayesian probability $P(\theta|n_1, ..., n_p)$, which is shown for $p = 1, 4, 7, 10, 13, 16$. After some, say 10 iterations a single peak emerges. (g) The results converge to the Heisenberg limit for the non-interacting MZ $\Delta\theta = 1\sqrt{2}/\sqrt{p}N$ for $p \sim 15$.

same time this state is completely robust to phase diffusion, since it is an eigenstate of $\hat{J}_z^2$. Thus, we believe that, the higher the NOON-component produced during the interferometer sequence, the better the phase sensitivity. However, further work is needed to clarify this. We expect that also $N-1$, $N-2$, etc. will contribute almost equally strong. Therefore in Fig. 8.8 (b) we plot the number fluctuations Δn right after the first beam splitter. Indeed it coincides with the transition of $\Delta\theta$, which happens approximately at those values of ξ_N where the number distribution becomes broad.

We next investigate the scaling of the CFI with N. Results are shown in Fig. 8.8 (c). We find Heisenberg scaling even for very large interactions, the total sensitivity being degraded only by a constant (N-independent) coefficient. From this we conclude, that also for very large interactions we can exploit quantum correlations for interferometry, particularly for large N.

Another very surprising feature is the following: In stark contrast to the ideal MZ, it makes sense to consider smaller than $\pi/2$ tunnel pulses. In Fig. 8.9 we compare $\pi/2$ and $\pi/3$-pulses. The time evolution during the interferometer sequence is shown in (a) and (b) on the Bloch sphere. As expected, the states are strongly twisted around the polar axis. When plotting $\Delta\theta$ versus interaction strength, (c), we find another transition: For $U_0 = 0$, the $\pi/3$ interferometer does not work at all. This becomes strongly changed by interactions, which make the sensitivity decrease again. Compared to the $\pi/2$-interferometer, there are even regions of better performance. However, the biggest advantage of smaller tunnel pulses is to facilitate the practical implementation

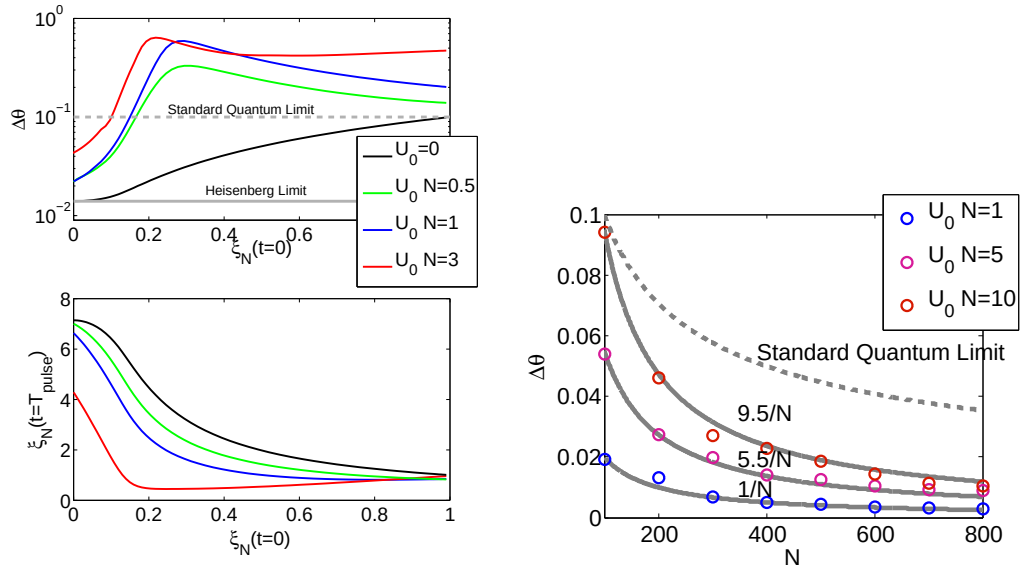

Figure 8.8: (a) Transition of phase sensitivity for different interactions versus initial number squeezing factor $\xi_N(t=0)$, calculated by the classical Fisher information. The extremum is reached approximately at those values of ξ_N, where the NOON - component, and other high N-components are large. In particular, we plot in (b) the number fluctuations after the first beam splitter $\xi_N(t=T_{pulse})$. Parameters are $N=100$, $T_{pulse}=2$ and $T_{phase}=1$. (c) Heisenberg scaling for various interactions, calculated by the classical Fisher information. Even for very large interactions, Heisenberg scaling persists, but with an increasing prefactor α (with $\Delta\theta=\alpha/N$). The non-interacting Heisenberg limit is close to that for $U_0N=1$.

of the interferometer, as will be shown in the next section. As discussed in the previous section, the number fluctuations after the first beam splitter serve as an explanation for the behaviour of the phase sensitivity, see (d). In particular, at around $U_0N=2.5$ it explains the superior performance of $\pi/3$. It is interesting and counterintuitive, that in some situations a smaller pulse leads to larger number fluctuations after the first beam splitter than a larger one. Phase distributions after the first beam splitter are shown in (e) and (f). For a Fock state, $\pi/2$-pulse, and without interactions, the phase is strongly peaked. With increasing interactions, the phase distribution becomes wider. However, as long as a distinct and fine (i.e., of order $1/N$) structures remain, the phase sensitivity is sub-shot noise. The phase distribution becomes washed out for very large interactions. For $\pi/3$-pulses, the phase distribution is very shallow for $U_0=0$, but becomes focused and even narrower than for the $\pi/2$-pulses with increasing interactions at $U_0N=2.5$. These structures in the phase can also be observed on the Bloch spheres in (a) and (b). In (g) $\Delta\theta$ is plotted against the pulse area. It has a wiggling structure and starts to increase slowly when approaching the value 0.5 showing how short the tunnel pulses can be made.

8.2.2 Realistic control

We now switch to an MCTDHB description of the MZ interferometer in presence of interactions. The challenge here is to design controls which achieve

- fast beam splitting operations
- without exciting the condensates.

A general difficulty when recombining condensates is the possibility of unwanted excitations (see Sec. 7), or even soliton creation [78]. This can be avoided by trapping the wave functions in stationary states after each of the beam splitters using optimal control, which is certainly a prerequisite for a successful interferometer performance. Therefore, we optimize trapping of the condensates in stationary states after each beam splitter. At the same time, we have to guarantee the beam splitter operation. This is achieved by requiring the pulse area $\int_0^T \Omega(t)dt$ to reach a desired value, e.g., $\pi/2$. The cost functional then reads

$$J = \frac{\gamma_1}{2}\left(\int_0^T \Omega(t)dt - A_\Omega^{\mathrm{d}}\right)^2 + \frac{\gamma_2}{2}[2 - |\langle\phi_g(T)|\phi_g^d\rangle|^2 - |\langle\phi_e(T)|\phi_e^d\rangle|^2] + \frac{\gamma}{2}\int_0^T (\dot{\lambda})^2 dt\ , \qquad (8.10)$$

where A_Ω^{d}, ϕ_g^d, and ϕ_g^e are the desired pulse areas and orbitals, respectively. We note that we perform the optimization in two steps, i.e., for each beam splitter separately.

Results are shown in Fig. 8.10. Since we find within the generic model that short pulse lengths are important, we use $T_{pulse} = 4$. In addition, we exploit the fact that we can use smaller pulses than $\pi/2$. While trapping works perfectly, the integrated pulse-area goal can be achieved up to 10%, see upper and middle panels. The controls are given by slightly deformed Gaussians. Moderate condensate oscillations are present during the beam splitters, but they are damped out after each of them due to OCT. The time dependence of the tunnel coupling is thereby a little complex, but we are interested only in the area under the pulses. We also show the two-body matrix elements, demonstrating that the dynamics is more complicated than that of a generic two-mode model. Finally, the lower panels show how number squeezing becomes transformed into phase squeezing after the first beam splitter. (a) and (b) show results for $N = 100$, while (c) and (d) for $N = 50$. On the left figures we show results for coherent states with very weak interactions of $U_0N = 0.01$ for comparison (shot noise), on the right pictures we show them for highly squeezed initial states $\xi_N = 0.05$ and typical interactions $U_0N = 1$. The results show a sensitivity close to the Heisenberg limit, see Fig. 8.11. This demonstrates that the MZ with interactions works also within realistic dynamics including the condensates oscillations.

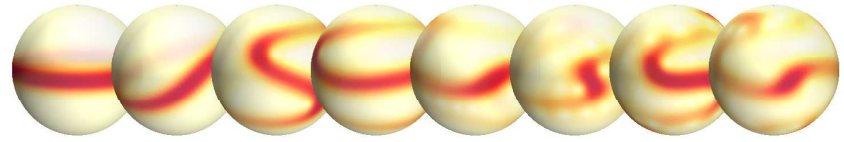

(a)

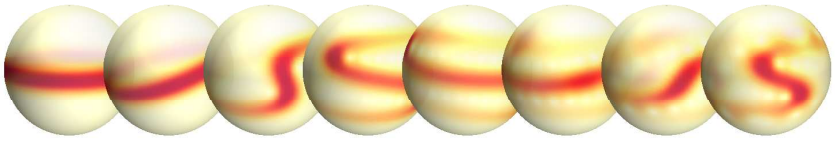

(b)

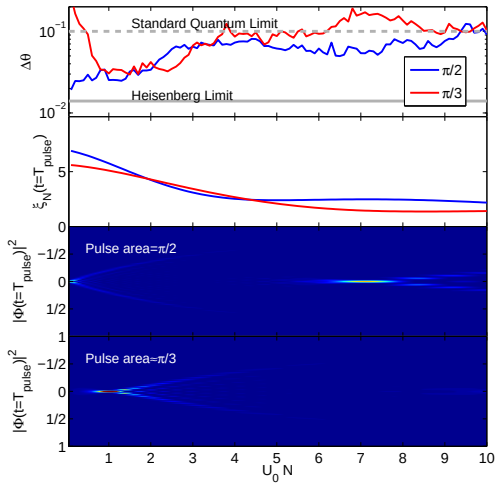

(c-f)

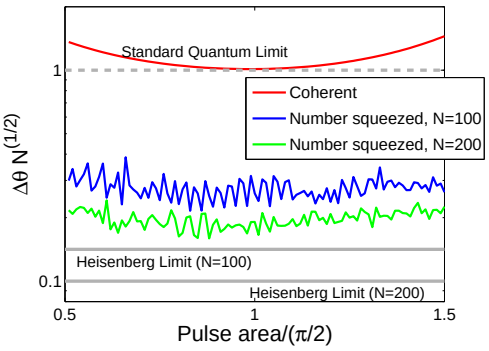

(g)

Figure 8.9: (a) $\pi/2$, (b) $\pi/3$ (approximately) interferometer sequences on the Bloch sphere for interactions $U_0 N = 1$. Input states are Fock states with phase $\theta = 0$. Notably are the fine ($1/N$-sized) structures on the Bloch spheres. (c) Phase sensitivity for $\pi/2$ and $\pi/3$-pulses. In presence of interactions $\pi/3$ pulses can as well give a good sensitivity. (d) Width of the number distribution after the first beam splitter and (e,f) structure in the phase distributions after the first beam splitter helps to explain the value of the phase sensitivity. Parameters are $N = 100$, $T_{pulse} = 2$ and $T_{phase} = 1$. (f) Phase sensitivity wiggles for varying pulse area.

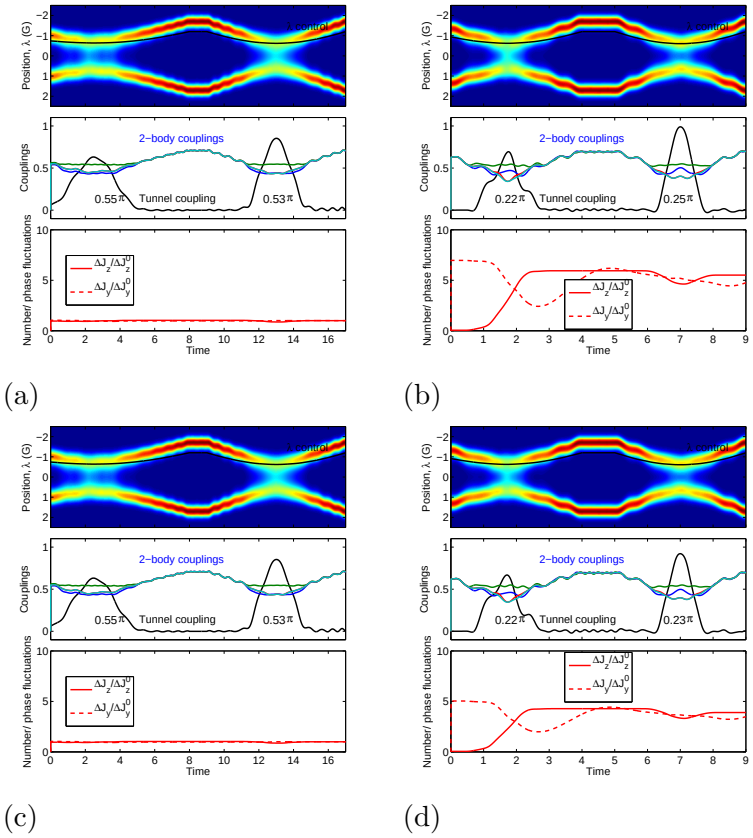

Figure 8.10: Typical realistic control sequences calculated from MCTDHB for $N = 100$ and (a) a coherent state (with interactions $U_0 N = 0.01$) and (b) a highly number squeezed state (with interactions $U_0 N = 1$). The durations of the pulse are $T_{pulse} = 8$ in (a) and $T_{pulse} = 4$ in (b). Upper panels show the control and density, middle panels the tunnel coupling and two-body matrix elements, and the lower panels number and phase squeezing. The controls could be designed such that the pulse area is approximately $\pi/2$ for the coherent state in (a). In presence of interactions it is easier to design controls for smaller pulse length of approximately $\pi/4$.

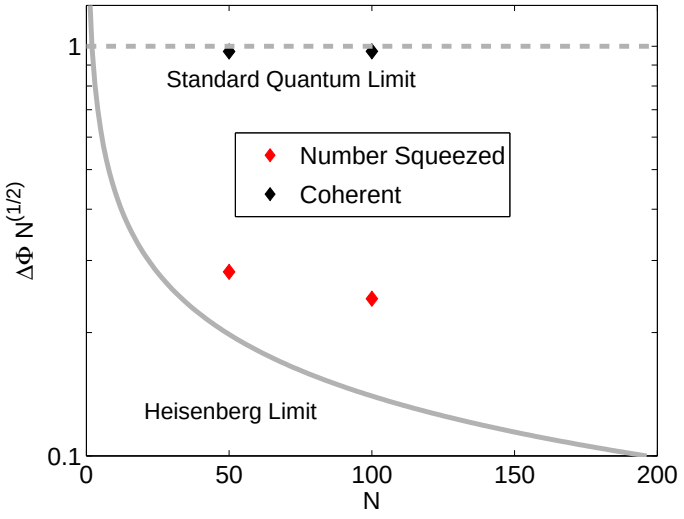

Figure 8.11: Phase sensitivity of realistic controls is close to the Heisenberg limit for highly number squeezed states ($\xi_N = 0.05$). We compare it to coherent states, which give shot noise.

Chapter 9

PAPER: Optimizing number squeezing when splitting a mesoscopic condensate: J. Grond, J. Schmiedmayer, and U. Hohenester, Phys. Rev. A 79, 021603(R) (2009).

Chapter 10

PAPER: Optimizing atom interferometry on atom chips: U. Hohenester, J. Grond, and J. Schmiedmayer, In special issue of Fortschr. Phys. 57, 1121 (2009).

Chapter 11

PAPER: Optimal control of number squeezing in trapped Bose-Einstein condensates: J. Grond, G. von Winckel, J. Schmiedmayer, and U. Hohenester, Phys. Rev. A 80, 053625 (2009).

Chapter 12

PAPER: Atom interferometry with trapped Bose-Einstein condensates: impact of atom–atom interactions: J. Grond, U. Hohenester, I. Mazets, and J. Schmiedmayer, New. J. Phys. 12, 065036 (2010).

Chapter 13

Summary and conclusions

We finally summarize and connect the conclusions from each part of this thesis. The main outcomes are control strategies as well as an analysis of atom interferometers with interacting BECs. The implementation of OCT for MCTDHB allowed us to devise control strategies for the optimal preparation of input states for atom interferometers, as well as optimal interferometer performance. This has to be done using a realistic model which takes into account condensate oscillations and excitations. Knowledge gained from simulations with more than two modes, has allowed us to learn about the effects of excitations in non-equilibrium condensates and their relation to quantum control. We found that the Mach-Zehnder interferometer is very robust against interactions if Bayesian phase estimation is used and our quantum control techniques are employed. We conclude that phase diffusion is practically not a substantial limitation for atom interferometry, which could have significant impact on the realization of trapped external state interferometers.

Optimal control of MCTDHB

OCT has been implemented within MCTDHB, which required to employ elaborate techniques of quantum control like the newly developed H^1 based optimization approach. This tool has been applied in several situations. Strategies for condensate splitting leading to a high number squeezing, one order of magnitude faster than with quasi-adiabatic splitting, could be identified. Preparation of phase squeezed states, as well as the Mach-Zehnder interferometer, require fast tunnel pulses (or cold atom beam splitters), without exciting the condensates.

Many-body dynamics of splitting of non-equilibrium condensates

We learned that condensate oscillations in a double-well induce substantial additional contributions to the number squeezing of $\mathcal{O}(\sqrt{N})$, which are mixed contributions from the condensates and the incoherent excitations. Since this mixing is absent for the ground state of the trap, we could use OCT trapping to damp out these additional contributions to number squeezing. This worked as long as the depletion did not influence the condensate dynamics, which we found to be true for a time scale of several ms. We furthermore learned about the limits of two-mode models and the signatures for a failing of the two-mode model. We think that the splitting ramps we have analyzed are prototypical for many non-adiabatic condensate situations, and number squeezing is a typical observable which depends on higher correlations.

Phase sensitivity of atom interferometers with interacting BECs

We found that a refocusing strategy appreciably helped to counteract the phase diffusion in Time-of-flight interferometers and to prepare phase squeezed states. Furthermore, elongated trap

geometries efficiently reduce phase diffusion.

The Mach-Zehnder interferometer is found to be very robust against interactions, as long as Bayesian phase estimation is used. In particular, we have found a surprising transition: while moderately phase squeezed states give far above shot-noise sensitivity in presence of interactions, highly squeezed states allow for Heisenberg limited interferometry. Even for very large interactions, the sensitivity is only deteriorated by a constant factor independent of N, such that Heisenberg scaling persists.

Bibliography

[1] A. Einstein. Quantentheorie des einatomigen idealen Gases. *Sitzungsber. Preuss. Akad. Wiss.* **Bericht 22**, 261 (1924).

[2] A. Einstein. Quantentheorie des einatomigen idealen Gases. II. *Sitzungsber. Preuss. Akad. Wiss.* **Bericht 1**, 3 (1925).

[3] S. N. Bose. Plancks Gesetz und Lichtquantenhypothese. *Z. Phys.* **26**, 178 (1924).

[4] M. H. Anderson, J. R. Ensher, M. R. Matthews, C. E. Wiemann, and E. A. Cornell. Observation of Bose-Einstein condensation in a dilute atomic vapor. *Science* **269**, 198 (1995).

[5] K. B. Davis, M.-O. Mewes, M. R. Andrews, N. J. van Druten, D. S. Durfee, D. M. Kurn, and W. Ketterle. Bose-Einstein condensation in a gas of sodium atoms. *Phys. Rev. Lett.* **75**, 3969 (1995).

[6] R. Folman, P. Krüger, J. Schmiedmayer, J. Denschlag, and C. Henkel. Microscopic atom optics: from wires to an atom chip. *Adv. At. Mol. Opt. Phy.* **48**, 263 (2002).

[7] D. Cronin, J. Schmiedmayer, and D. E. Pritchard. Optics and interferometry with atoms and molecules. *Rev. Mod. Phys.* **81**, 1051 (2009).

[8] C. M. Caves. Quantum-mechanical noise in an interferometer. *Phys. Rev. D* **23**, 1693 (1981).

[9] M. Kitagawa and M. Ueda. Squeezed spin states. *Phys. Rev. A* **47**, 5138 (1993).

[10] D. J. Wineland, J. J. Bollinger, W. M. Itano, and D. J. Heinzen. Squeezed atomic states and projection noise in spectroscopy. *Phys. Rev. A* **50**, 67 (1994).

[11] J. Estève, C. Gross, A. Weller, S. Giovanazzi, and M. K. Oberthaler. Squeezing and entanglement in a Bose-Einstein condensate. *Nature* **455**, 1216 (2008).

[12] L. Pezzé and A. Smerzi. *Phys. Rev. A* **73**, 011801 (2006).

[13] T. Schumm, S. Hofferberth, L. M. Andersson, S. Wildermuth, S. Groth, I. Bar-Joseph, J. Schmiedmayer, and P. Krüger. Matter-wave interferometry in a double well on an atom chip. *Nat. Phys.* **1**, 57 (2005).

[14] N. N. Bogoliubov. On the theory of superfluidity. *J. Phys. USSR* **11**, 23 (1947).

[15] L. P. Pitaevskii. Vortex lines in an imperfect Bose gas. *Sov. Phys. JETP* **13**, 451 (1961).

[16] E. P. Gross. Structure of a quantized vortex in boson systems. *Il Nuovo Cimento* **20**, 454 (1961).

[17] A. Barone and G. Paterno. *Physics and Application of the Joesphson effect.* John Wiley & Sons (1982).

[18] G. J. Milburn, J. Corney, E. M. Wright, and D. F. Walls. Quantum dynamics of an atomic Bose-Einstein condensate in a double-well potential. *Phys. Rev. A* **55**, 4318 (1997).

[19] O. E. Alon, A. I. Streltsov, and L. S. Cederbaum. The multi-configurational time-dependent Hartree method for bosons: Many-body dynamics of bosonic systems. *Phys. Rev. A* **77**, 033613 (2008).

[20] A. P. Peirce, M. A. Dahleh, and H. Rabitz. Optimal control of quantum-mechanical systems: Existence, numerical application, and applications. *Phys. Rev. A* **37**, 4950 (1988).

[21] H. Rabitz, R. de Vivie-Riedle, M. Motzkus, and K. Kompka. Wither the future of controlling quantum phenomena. *Science* **288**, 824 (2000).

[22] C. M. Tesch and R. de Vivie-Riedle. Quantum computation with vibrationally excited molecules. *Phys. Rev. Lett.* **89**, 157901 (2002).

[23] U. Hohenester, P. K. Rekdal, A. Borzì, and J. Schmiedmayer. Optimal quantum control of Bose-Einstein condensates in magnetic microtraps. *Phys. Rev. A* **75**, 023602 (2007).

[24] J. Fortagh and C. Zimmermann. Magnetic microtraps for ultracold atoms. *Rev. Mod. Phys.* **79**, 235 (2007).

[25] D. E. Pritchard. Cooling neutral atoms in a magnetic trap for precision spectroscopy. *Phys. Rev. Lett.* **51**, 1336 (1983).

[26] J. D. Weinstein and K. G. Libbrecht. Microscopic magnetic traps for neutral atoms. *Phys. Rev. A* **52**, 4004 (1995).

[27] J. Schmiedmayer. A wire trap for neutral atoms. *Appl. Phys. B* **60**, 169 (1995).

[28] J. Reichel and J. H. Thywissen. Using magnetic chip traps to study Tonks-Girardeau quantum gases. *J. Phys. IV* **116**, 265 (2004).

[29] W. Hänsel, P. Hommelhoff, T. W. Hänsch, and J. Reichel. Bose Einstein condensation on a microelectronic chip. *Nature* **413**, 498 (2001).

[30] H. Ott, J. Fortagh, G. Schlotterbeck, A. Grossmann, and C. Zimmermann. Bose Einstein condensation in a surface microtrap. *Phys. Rev. Lett.* **87**, 023401 (2001).

[31] S. Schneider, A. Kasper, C. vom Hagen, M. Bartenstein, B. Engeser, T. Schumm, I. Bar-Joseph, R. Folman, L. Feenstra, and J. Schmiedmayer. Atom chips: Fabrication and thermal properties. *Appl. Phys. Lett.* **85**, 2980 (2004).

[32] I. Lesanovsky, T. Schumm, S. Hofferberth, L. M. Andersson, P. Krüger, and J. Schmiedmayer. Adiabatic radio-frequency potentials for the coherent manipulation of matter waves. *Phys. Rev. A* **73**(3), 033619 (2006).

[33] I. Lesanovsky, S. Hofferberth, J. Schmiedmayer, and P. Schmelcher. Manipulation of ultracold atoms in dressed adiabatic radio-frequency potentials. *Phys. Rev. A* **74**, 033619 (2006).

[34] F. Dalfovo, S. Giorgini, L. P. Pitaevskii, and S. Stringari. Theory of Bose-Einstein condensation in trapped gases. *Rev. Mod. Phys.* **71**, 463 (1999).

[35] A. Leggett. Bose-Einstein condensation in alkali gases: Some fundamental concepts. *Rev. Mod. Phys.* **73**, 307 (2001).

[36] C. J. Pethick and H. Smith. *Bose-Einstein condensation in dilute gases*. Cambridge University Press (2008).

[37] K. Sakmann, A. I. Streltsov, O. E. Alon, and L. S. Cederbaum. Reduced density matrices and coherence of trapped interacting bosons. *Phys. Rev. A* **78**, 023615 (2008).

[38] O. Penrose and L. Onsager. Bose-Einstein condensation and liquid helium. *Phys. Rev.* **104**, 576 (1956).

[39] D. Petrov, D. Gangardt, and G. Shlyapnikov. Low-dimensional trapped gases. *J. Phys. IV* **116**, 5 (2004).

[40] M. Olshanii. Atomic scattering in the presence of an external confinement and a gas of impenetrable Bosons. *Phys. Rev. Lett.* **81**, 938 (1998).

[41] J. Grond, G. von Winckel, J. Schmiedmayer, and U. Hohenester. Optimal control of number squeezing in trapped Bose-Einstein condensates. *Phys. Rev. A* **80**, 053625 (2009).

[42] A. L. Fetter. Nonuniform states of an imperfect bose gas. *Ann. Phys. (N.Y.)* **70**, 67 (1972).

[43] J. Javanainen and M. Y. Ivanov. Splitting a trap containing a Bose-Einstein condensate: Atom number fluctuations. *Phys. Rev. A* **60**, 2351 (1999).

[44] C. Menotti, J. R. Anglin, J. I. Cirac, and P. Zoller. Dynamic splitting of a Bose-Einstein condensate. *Phys. Rev. A* **63**, 023601 (2001).

[45] F. T. Arecchi, H. Thomas, R. Gilmore, and E. Courtens. *Phys. Rev. A* **6**, 2211 (1972).

[46] H.-D. Meyer, F. Gatti, and G. A. Worth, editors. *Multidimensional Quantum Dynamics: MCTDH Theory and Applications*. WILEY-VCH, Weinheim (2009).

[47] H.-D. Meyer, U. Manthe, and L. S. Cederbaum. The multi-configurational time-dependent Hartree approach. *Chem. Phys. Lett.* **165**, 73 (1990).

[48] A. I. Streltsov, O. E. Alon, and L. S. Cederbaum. Role of excited states in the splitting of a trapped interacting Bose-Einstein condensate by a time-dependent barrier. *Phys. Rev. Lett.* **99**, 030402 (2007).

[49] L. Pitaevskii and S. Stringari. Thermal vs quantum decoherence in double well trapped Bose-Einstein condensates. *Phys. Rev. Lett.* **87**, 180402 (2001).

[50] Y. Castin and J. Dalibard. Relative phase of two Bose-Einstein condensates. *Phys. Rev. A* **55**, 4330 (1997).

[51] L. Pezzé, A. Smerzi, G. P. Berman, A. R. Bishop, and L. A. Collins. Nonlinear beam splitter in Bose-Einstein-condensate interferometers. *Phys. Rev. A* **74**, 033610 (2006).

[52] V. Giovannetti, S. Lloyd, and L. Maccone. Quantum-enhanced measurements: Beating the standard quantum limit. *Science* **306**, 1330 (2004).

[53] L. Pezzé and A. Smerzi. Mach-Zehnder interferometry at the Heisenberg limit with coherent and squeezed-vacuum light. *Phys. Rev. Lett.* **100**, 073601 (2008).

[54] L. Pezzé and A. Smerzi. Entanglement, nonlinear dynamics, and the Heisenberg limit. *Phys. Rev. Lett.* **102**, 100401 (2009).

[55] C. W. Helstrom. *Quantum Detection and Estimation Theory.* Academic Press, New York (1976).

[56] A. S. Holevo. *Probabilistic and Statistical Aspects of Quantum Theory.* North-Holland, Amsterdam (1982).

[57] L. Pezzé, A. Smerzi, G. Khoury, J. F. Hodelin, and D. Bouwmeester. Phase detection at the quantum limit with multiphoton Mach-Zehnder interferometry. *Phys. Rev. Lett.* **99**, 223602 (2007).

[58] M. Jääskeläinen, W. Zhang, and P. Meystre. Limits to phase resolution in matter-wave interferometry. *Phys. Rev. A* **70**, 063612 (2004).

[59] J. Chwedeńczuk, F. Piazza, and A. Smerzi. Private communications.

[60] C. Brif, R. Chakrabarti, and H. Rabitz. Control of quantum phenomena: Past, present, and future. Accepted for publication in New J. Phys. (Focus issue: Quantum control), arXiv:0912.5121.

[61] T. Calarco, U. Dorner, P. S. Julienne, C. J. Williams, and P. Zoller. Quantum computations with atoms in optical lattices: Marker qubits and molecular interactions. *Phys. Rev. A* **70**, 012306 (2004).

[62] C. P. Koch, J. P. Palao, R. Kosloff, and F. Masnou-Seeuws. Stabilization of ultracold molecules using optimal control theory. *Phys. Rev. A* **70**, 013402 (2004).

[63] U. Hohenester and G. Stadler. Quantum control of electron-phonon scatterings in artificial atoms. *Phys. Rev. Lett.* **92**, 196801 (2004).

[64] G. von Winckel and A. Borzì. Computational techniques for a quantum control problem with H^1-cost. *Inverse Problems* **24**, 034007 (2008).

[65] D. P. Bertsekas. *Nonlinear Programming.* Athena Scientific, Cambridge, UK (1999).

[66] A. Borzì, G. Stadler, and U. Hohenester. Optimal quantum control in nanostructures: Theory and application to generic three-level system. *Phys. Rev. A* **66**, 053811 (2002).

[67] J. Grond, J. Schmiedmayer, and U. Hohenester. Optimizing number squeezing when splitting a mesoscopic condensate. *Phys. Rev. A* **79**, 021603(R) (2009).

[68] U. Hohenester, J. Grond, and J. Schmiedmayer. Optimizing atom interferometry on atom chips. *In special issue of Fortschr. Phys.* **57**, 1121 (2009).

[69] M. O. Scully and M. S. Zubairy. *Quantum Optics.* Cambridge University Press, Cambridge, UK (1997).

[70] C. K. Law, H. T. Ng, and P. T. Leung. Coherent control of spin squeezing. *Phys. Rev. A* **63**, 055601 (2001).

[71] J. Grond, U. Hohenester, J. Schmiedmayer, and A. Scrinzi. Stability and fragmentation of non-equilibrium Bose-Einstein condensates. In preparation.

[72] A. Eckardt, T. Jinasundra, C. Weiss, and M. Holthaus. Analog of photon-assisted tunneling in a Bose-Einstein condensate. *Phys. Rev. Lett* **95**, 200401 (2005).

[73] J. Grond, U. Hohenester, I. Mazets, and J. Schmiedmayer. Atom interferometry with trapped Bose-Einstein condensates: impact of atom-atom interactions. *New J. Phys.* **12**, 065036 (2010).

[74] C. Chin, R. Grimm, P. Julienne, and E. Tiesinga. Feshbach resonances in ultracold gases. *Rev. Mod. Phys.* **82**, 1225 (2010).

[75] J. Grond, U. Hohenester, J. Schmiedmayer, and A. Smerzi. In preparation.

[76] J. Javanainen and M. Wilkens. Phase and phase diffusion of a split bose-einstein condensate. *Phys. Rev. Lett.* **78**, 4675 (1997).

[77] M. J. Holland and K. Burnett. Interferometric detection of optical phase shifts at the Heisenberg limit. *Phys. Rev. Lett.* **71**, 1355 (1993).

[78] A. Negretti and C. Henkel. Enhanced phase sensitivity and soliton formation in an integrated BEC interferometer. *Journal of Physics B: Atomic, Molecular and Optical Physics* **37**, L385 (2004).

[79] U. Manthe, H.-D. Meyer, and L. S. Cederbaum. Wave-packet dynamics within the multiconfiguration Hartree framework: General aspects and application to NOCl. *J. Chem. Phys.* **97**, 3199 (1992).

[80] V. Thomee. *Galerkin Finite Element Methods for Parabolic Problems.* Springer-Verlag, New York (1997).

[81] J. Nocedal and S. J. Wright. *Numerical Optimization.* Springer, New York, USA (1999).

Appendix A

Derivation of the MCTDHB equations

We derive the MCTDHB equations starting from the action

$$S[\{C_{\vec{n}}(t)\},\{\phi_k(x,t)\}] = \int dt \Bigg\{ \langle\Psi|\big(\hat{H} - i\frac{\partial}{\partial t}\big)|\Psi\rangle - \sum_{i,j=1}^{M} \mu_{kj}(t)[\langle\phi_k|\phi_j\rangle - \delta_{kj}] \Bigg\} , \tag{A.1}$$

using variational calculus. For the variation with respect to the coefficients we use a matrix representation of the expectation values with respect to the permanents $|\vec{n}\rangle$ from Eq. (A.1), which generally reads

$$\langle\Psi|\big(\hat{H} - i\frac{\partial}{\partial t}\big)|\Psi\rangle = \sum_{\vec{n}} C^*_{\vec{n}} \Big[\sum_{\vec{n}'} \langle\vec{n};t|\big(\hat{H} - i\frac{\partial}{\partial t}\big)|\vec{n}';t\rangle C_{\vec{n}'} - i\frac{\partial C_{\vec{n}}}{\partial t} \Big]. \tag{A.2}$$

Defining the matrix elements as $H_{\vec{n}\vec{n}'} = \langle\vec{n};t|\hat{H}|\vec{n}';t\rangle$, the equation obtained from the variation is

$$\frac{\partial S[\{C_{\vec{n}}(t)\},\{\phi_k(x,t)\}]}{\partial C^*_{\vec{n}}(t)} = 0\,, \quad \Longrightarrow \quad i\frac{\partial \mathbf{C}(t)}{\partial t} = \mathcal{H}(t)\mathbf{C}(t)\,. \tag{A.3}$$

Here we exploited a gauge freedom of this framework: the ansatz Eq. (3.32) is invariant to unitary transformation of the orbitals and coefficients [47, 79]. Exploiting this, one can find a gauge such that $\langle\phi_k|\dot{\phi}_j\rangle = 0$ $(k,q = 1,...,M)$, and the time derivative term in Eq. (A.2) vanishes. The explicit form of this matrix involves overlap integrals of two orbitals with the bare Hamiltonian $h_{kq} = \int dx \phi^*_k \hat{h} \phi_q$, and the interaction terms $W_{ksql} = U_0 \int dx \phi^*_k \phi^*_s \phi_q \phi_l$. For $M = 2$ it is similar to the generic two-mode model described in Sec. 3.3, but in contrast all the coupling terms are maintained.

The variation with respect to the orbitals requires to write down the Hamiltonian in second quantized form

$$\hat{H} = \sum_{k,q} b^\dagger_k b_q h_{kq} + \frac{1}{2} \sum_{k,q,s,l} b^\dagger_k b^\dagger_s b_q b_l W_{ksql}\,. \tag{A.4}$$

The expectation value involves then the one- and two-body reduced density matrices $\rho_{kq}(t) = \langle\Psi|b^\dagger_k b_q|\Psi\rangle$ and $\rho_{ksql}(t) = \langle\Psi|b^\dagger_k b^\dagger_s b_q b_l|\Psi\rangle$:

$$\langle\Psi|\big(\hat{H} - i\frac{\partial}{\partial t}\big)|\Psi\rangle = \sum_{k,q=1}^{M} \rho_{kq} \left[h_{kq} - \Big(i\frac{\partial}{\partial t}\Big)_{kq} \right] + \frac{1}{2} \sum_{k,s,q,l=1}^{M} W_{ksql} - i \sum_{\vec{n}} C^*_{\vec{n}} \frac{\partial C_{\vec{n}}}{\partial t}\,. \tag{A.5}$$

Variation yields

$$\frac{\partial S[\{C_{\vec{n}}(t)\},\{\phi_k(x,t)\}]}{\partial \phi_k^*(x,t)} = 0 \quad \Longrightarrow \quad \sum_{q=1}^{M}\left[\rho_{kq}\Big(\hat{h} - i\frac{\partial}{\partial t}\Big) + \sum_{s,l=1}^{M}\rho_{ksql}\phi_s^*\phi_l\right]\phi_q = \sum_{j=1}^{M}\mu_{kj}\phi_j \quad \text{(A.6)}$$

The Lagrange multipliers μ_{kj} can be eliminated by using the orthonormality property of the orbitals. The final equation for the orbitals reads then

$$i\dot{\phi}_j = \hat{\mathbf{P}}[\hat{h}\phi_j + U_0 \sum_{k,s,q,l=1}^{M}\{\rho(t)\}_{jk}^{-1}\rho_{ksql}\phi_s^*\phi_l\phi_q] \,, \quad \text{(A.7)}$$

where we introduced a projector $\hat{\mathbf{P}} = 1 - \sum_{i=1}^{M}|\phi_i\rangle\langle\phi_i|$, which carries out integration over space. We again used the particular choice of gauge $\langle\phi_k|\dot{\phi}_j\rangle = 0$, where the change of the orbitals is orthogonal to all the orbitals. This property is then obviously fulfilled by Eq. (A.7). This feature makes the time propagation particularly stable.

Appendix B

Numerical implementation

B.1 Time-stepping scheme for MCTDHB(2)

We use an implicit time-stepping scheme, which is particularly well suited for OCT applications since it strictly preserves the norm. This is crucial since the value of the cost functional might decrease due to mistakes in the norm, which leads to wrong optimization results. We employ a **Modified Crank-Nicolson method** (MCN) [80] to solve an initial value problem $i\dot{y} = f(y,t)$, for which a time step reads

$$\frac{y^{n+1}-y^n}{\Delta t} = -if\left(\frac{y^{n+1}+y^n}{2}, \frac{t^{n+1}+t^n}{2}\right) + \mathcal{O}(\Delta t^3)\,. \tag{B.1}$$

This can be seen as follows: Generally, we have a unitary (nonlinear) problem which has the form $f(y,t) = H(y,t)y$, where $H(y,t)$ is self-adjoint ('Hamiltonian'). This holds in particular when f is the right hand side of the MCTDHB equations (3.36) and (3.38), and y stands for

$$y = \begin{pmatrix} \phi_g \\ \phi_e \\ \mathbf{C} \end{pmatrix}, \tag{B.2}$$

with an inner product given by $\langle y|y'\rangle = \int dx \phi_g^* \phi_g' + \int dx \phi_e^* \phi_e' + \mathbf{C}^\dagger \mathbf{C}'$. Then, Eq. (B.1) can be rewritten as

$$y^{n+1} = \frac{1 - i\frac{\Delta t}{2} H\left(\frac{y^{n+1}+y^n}{2}, \frac{t^{n+1}+t^n}{2}\right)}{1 + i\frac{\Delta t}{2} H\left(\frac{y^{n+1}+y^n}{2}, \frac{t^{n+1}+t^n}{2}\right)} y^n\,, \tag{B.3}$$

where the operator which transforms y^n to y^{n+1} is obviously unitary. Note that MCN differs from the standard CN by taking averages at times t^n and t^{n+1} of the arguments of f, instead of the averages of the function values like. This guarantees unitarity for nonlinear and time-dependent problems. Eq. (B.1) constitutes a nonlinear equation $g(y) = 0$ (g is differentiable), which can be solved iteratively for y using **Newton's method**. For a reasonable initial guess y^0, one calculates a better solution y^1 from the equation

$$g'(y^k)[y^{k+1} - y^k] = -g(y^k)\,. \tag{B.4}$$

In this fashion, y^k ($k = 1, 2, ...$) converge quadratically to the solution y for successive iterations. g' is a Fréchet derivative given by $g'(y)\Delta y := \delta g_y(y, \Delta y)$, which is a linear functional of the difference between the iterative solutions $\Delta y := y^{k+1} - y^k$.

For the MCN time step we have to solve the equation $g(y) = y - y^0 - \Delta t f(\frac{y+y_0}{2}, \frac{t+t_0}{2})$. In this case, y^0 and y stand for the old $y^0 := y^n$ and the current solution $y := y^k$ for the new (unknown) time step y^{n+1}, respectively. The Newton's

$$\Delta y + i\Delta t\, \delta f_y(\bar{y}, \bar{t}; \Delta y) = 2(y^0 - \bar{y}) - i\Delta t f(\bar{y}, \bar{t})\,, \tag{B.5}$$

where $\bar{y} = \frac{y+y^0}{2}$ and $\bar{t} = \frac{t+t^0}{2}$. We use as initial guess y^0, a time step according to Eq. (B.3) but with exclusively evaluating f at the old time step ($y^{n+1} \to y^n$). For MCTDHB(2), Eq. (B.5) has a structure

$$\Delta y + \frac{i\Delta t}{2}\Big[A\Delta y + B\Delta y^* + \sum_{i=1}^{k}\langle v_1^{(i)}|\Delta y\rangle u_1^{(i)} + \sum_{i=1}^{k}\langle \Delta y|v_2^{(i)}\rangle u_2^{(i)} + \sum_{i=1}^{k} Re\langle v_3^{(i)}|\Delta y\rangle u_3^{(i)}\Big] = b\,. \tag{B.6}$$

The involved matrices A, B (size determined by the spatial grid, $n \times n$) and vectors $v_l^{(i)}$ and $u_l^{(i)}$ ($l = 1, 2, 3$, $i = 1, 2, ..., k$) with size n are given in Sec. B.3. In Eq. (B.6) the expression in square brackets corresponds to the functional derivative $\delta f_y(y, \bar{t}; \Delta y)$, the factor $1/2$ in front of it appearing due to the argument $\bar{y}$.

In Eq. (B.6) A and B are sparse matrices , which can be efficiently inverted. The matrices $u_1^{(i)}\langle v_1^{(i)}|\cdot$ instead are low-rank non-sparse matrices. Efficient inversion can be achieved by the Sherman-Morrison-Woodbury (SMW) formula [81]. To give an example, we consider first only the terms which involve Δy, and write the low rank matrices as

$$\tilde{U}\tilde{V}|\Delta y\rangle = \frac{i\Delta t}{2}\Delta y \sum_{i=1}^{k_1}\langle v_1^{(i)}|\Delta y\rangle u_1^{(i)}\,, \tag{B.7}$$

where $\tilde{U}$ contains the $u_1^{(i)}$ as columns, multiplied by $\frac{i\Delta t}{2}$, and $\tilde{V}$ contains $(v_1^{(i)})^*$ as rows. The dimensions of these matrices are $n \times k$ and $k \times n$, respectively. We further define $\tilde{A} := \Delta y + \frac{i\Delta t}{2}A$. Eq. (B.6) can then be solved efficiently for Δy by

$$\Delta y = (\tilde{A} + \tilde{U}\tilde{V})^{-1}b = \Big(\tilde{A}^{-1} - \tilde{A}^{-1}\tilde{U}(1 + \tilde{V}\tilde{A}^{-1}\tilde{U})^{-1}\tilde{V}\tilde{A}^{-1}\Big)b\,. \tag{B.8}$$

In order to include the terms in Eq. (B.6) which involve Δy^*, we need complex extensions to the SMW formula. This can be achieved using the matrix representation of complex numbers

$$\Delta y = \Delta y_r + i\Delta y_i \;\to\; \begin{pmatrix} \Delta y_r & -\Delta y_i \\ \Delta y_i & \Delta y_r \end{pmatrix}. \tag{B.9}$$

A matrix vector multiplication can be written as

$$\begin{pmatrix} A_r & -A_i \\ A_i & A_r \end{pmatrix}\begin{pmatrix} \Delta y_r \\ \Delta y_i \end{pmatrix}, \tag{B.10}$$

and complex conjugation is achieved by transposition, or in vector notation by

$$\begin{pmatrix} \Delta y_r \\ -\Delta y_i \end{pmatrix} = \begin{pmatrix} 1 & 0 \\ 0 & -1 \end{pmatrix}\begin{pmatrix} \Delta y_r \\ \Delta y_i \end{pmatrix}. \tag{B.11}$$

We rewrite Eq. (B.6) using this representation, and define matrices U_l and V_l, which contain the corresponding vectors $v_l^{(i)}$ and $u_l^{(i)}$ as columns:

$$\begin{pmatrix} \Delta y_r \\ \Delta y_i \end{pmatrix} + \frac{i\Delta t}{2}\Bigg[\begin{pmatrix} A_r & -A_i \\ A_i & A_r \end{pmatrix} + \begin{pmatrix} B_r & B_i \\ B_i & -B_r \end{pmatrix} + \begin{pmatrix} U_{1,r} & -U_{1,i} \\ U_{1,i} & U_{1,r} \end{pmatrix}\begin{pmatrix} V_{1,r}^T & V_{1,i}^T \\ -V_{1,i}^T & V_{1,r}^T \end{pmatrix}$$
$$+\begin{pmatrix} U_{2,r} & -U_{2,i} \\ U_{2,i} & U_{2,r} \end{pmatrix}\begin{pmatrix} V_{2,r}^T & V_{2,i}^T \\ V_{2,i}^T & -V_{2,r}^T \end{pmatrix} + \begin{pmatrix} U_{3,r} \\ U_{3,i} \end{pmatrix}\begin{pmatrix} V_{3,r}^T & V_{3,i}^T \end{pmatrix}\Bigg]\begin{pmatrix} \Delta y_r \\ \Delta y_i \end{pmatrix} = \begin{pmatrix} b_r \\ b_i \end{pmatrix}. \tag{B.12}$$

This system, which contains matrices of size $2n \times 2n$, can be exactly written in the form Eq. (B.8) and thus can be solved efficiently for Δy using the SMW-formula. As a stopping criterion for the Newton's equation we typically use $|y^{k+1} - y^k| < 10^{-5}$.

B.2 OCT of MCTDHB(2)

In this section we discuss the gradient and backward (adjoint) equation for MCTDHB(2). The procedure for the derivation of the optimal control system is described in Chap. 5. The Lagrange function reads

$$\begin{aligned} &L(\phi_g, \phi_e, \mathbf{C}, \tilde{\phi}_g, \tilde{\phi}_e, \tilde{\mathbf{C}}, \lambda) = J(\phi_g, \phi_e, \mathbf{C}, \lambda) + \\ &\sum_k Re\langle \tilde{\phi}_k, i\dot{\phi}_k - \hat{\mathbf{P}}\big[\hat{h}\phi_k + U_0\{\rho\}^{-1}_{kk} \sum_{s,q,l}{}' \rho_{ksql}\phi^*_s\phi_q\phi_l\big]\rangle \\ &+Re\langle \tilde{\mathbf{C}}, i\dot{\mathbf{C}} - \big(-\Omega\hat{J}_x + \frac{1}{2}\sum_{k,q,l,m}{}' \hat{a}^\dagger_k\hat{a}^\dagger_q\hat{a}_l\hat{a}_m W_{kqlm}\big)\mathbf{C}\rangle\,, \end{aligned} \tag{B.13}$$

with adjoint variables $\tilde{\phi}_g$, $\tilde{\phi}_e$, and $\tilde{\mathbf{C}}$.

We consider a cost functional containing all control goals relevant for our work: the squeezing and the trapping goal (see Chap. 6, Eq.), the phase squeezing goal (see Chap. 8.1, Eq. (8.7)), and the pulse area goal (see Chap. 8.2, Eq. (8.10)). These special cases can be recovered by choosing appropriate γ coefficients:

$$\begin{aligned} J(\phi_g, \phi_e, \mathbf{C}, \lambda) &= \frac{\gamma_1}{2}[2 - |\langle\phi_g(T)|\phi^d_g\rangle|^2 - |\langle\phi_e(T)|\phi^d_e\rangle|^2] + \frac{\gamma_2}{2}\langle\mathbf{C}(T)|\hat{\hat{J}}^2_z|\mathbf{C}(T)\rangle \\ &+\frac{\gamma_3}{2}\Big(\Delta J^d_y - \langle\mathbf{C}(T)|\hat{\hat{J}}^2_y|\mathbf{C}(T)\rangle\Big)^2 + \frac{\gamma_4}{2}\left(\int_0^T \Omega(t)dt - A^{\mathrm{d}}_\Omega\right)^2 + \frac{\gamma}{2}\int_0^T \big[\dot{\lambda}(t)\big]^2 dt\,. \end{aligned} \tag{B.14}$$

Hereby, we used pseudospin operators for MCTDHB which are defined as

$$\hat{\hat{J}}_x = \hat{J}_x\,, \quad \hat{\hat{J}}_z = d\hat{a}^\dagger_g\hat{a}_e + d^*\hat{a}^\dagger_e\hat{a}_g\,, \hat{\hat{J}}_y = id\hat{a}^\dagger_g\hat{a}_e - d^*\hat{a}^\dagger_e\hat{a}_g\,, \tag{B.15}$$

with

$$d = \left(\int_{-\infty}^0 dx\phi^*_g[x]\phi_e[x] - \int_0^\infty dx\phi^*_g[x]\phi_e[x]\right)/2\,. \tag{B.16}$$

B.2.1 Gradient

The gradient for the Lagrangian Eq. (B.13) reads

$$\begin{aligned} \nabla\hat{J} \;=\; &-\gamma\ddot{\lambda} - \sum_k Re\langle\tilde{\phi}_k|\frac{\partial V_\lambda}{\partial\lambda}|\phi_k\rangle + Re\sum_{q,k}\langle\tilde{\phi}_q|\phi_k\rangle\langle\phi_k|\frac{\partial V_\lambda}{\partial\lambda}|\phi_q\rangle \\ &-Re\langle\tilde{\mathbf{C}}|\hat{J}_x|\mathbf{C}\rangle\sum_k(-1)^k\langle\phi^*_k|\frac{\partial V_\lambda}{\partial\lambda}|\phi_k\rangle\,. \end{aligned} \tag{B.17}$$

B.2.2 Backward equations

We derive the backward equations Eq. (5.2) for MCTDHB(2).

Terminal conditions

The terminal conditions are given by

$$i\tilde{\phi}_k(T) = -\gamma_1\langle\phi_k^d|\phi_k(T)\rangle\phi_k^d + \gamma_2\langle\mathbf{C}(T)|\{\hat{\tilde{J}}_z, \hat{a}_k^\dagger\hat{a}_q\}|\mathbf{C}(T)\rangle\frac{\Theta(-x)-\Theta(x)}{2}\phi_q(T)\,, \tag{B.18}$$
$$+\gamma_3 i(-1)^k 2\Big(\Delta J_y^d - \langle\mathbf{C}(T)|\hat{\tilde{J}}_y^2|\mathbf{C}(T)\rangle\Big)\langle\mathbf{C}(T)|\{\hat{\tilde{J}}_y, \hat{a}_k^\dagger\hat{a}_q\}|\mathbf{C}(T)\rangle\frac{\Theta(-x)-\Theta(x)}{2}\phi_q(T)\,,$$

with $k \neq q$, and

$$i|\tilde{\mathbf{C}}(T)\rangle = \gamma_2\hat{\tilde{J}}_z^2|\mathbf{C}(T)\rangle + \gamma_3 2\Big(\Delta J_y^d - \langle\mathbf{C}(T)|\hat{\tilde{J}}_y^2|\mathbf{C}(T)\rangle\Big)\hat{\tilde{J}}_y^2|\mathbf{C}(T)\rangle\,. \tag{B.19}$$

Equations of motion

We write the MCTDHB(2) equations as $i\dot{y} = f(y,t)$, similar to Sec. B.1. Whenever the cost functional $J(y,\lambda)$ depends only on the wave function at the final time $y(T)$, the Frèchet derivative of L with respect to y reads

$$\delta L_y = -\frac{i}{2}[\langle\dot{\tilde{y}}|\delta y\rangle + \langle\delta y|\dot{\tilde{y}}\rangle] - \int dt Re\langle\tilde{y}|\delta f_y(y,t;\delta y)\rangle + \int dt\Big[\langle\delta y|\frac{\partial\tilde{J}}{\partial y^*}\rangle + \text{c.c.}\Big]\,. \tag{B.20}$$

This expressions depends on the functional derivative $\delta f_y(y,t;\delta y)$ with respect to the test function δy. It is a linear functional of δy given by Eq. (B.6). Inserted in Eq. (B.20), it has the following structure:

$$\delta L_y = -\frac{i}{2}\langle\delta y|\dot{\tilde{y}}\rangle - \frac{1}{2}\int dt\langle\delta y|\cdot\rangle + \text{c.c.}\,. \tag{B.21}$$

The equation for the adjoint variable $\tilde{y}$ reads in terms of the expressions introduced in Sec. B.1 (evaluated at t)

$$i\dot{\tilde{y}} = -[(A^\dagger + C)\tilde{y} + B\tilde{y}^* + \sum_{i=1}^k\langle u_1^{(i)}|\tilde{y}\rangle v_1^{(i)} + \sum_{i=1}^k\langle\tilde{y}|u_2^{(i)}\rangle v_2^{(i)} + \sum_{i=1}^k Re\langle u_3^{(i)}|\tilde{y}\rangle v_3^{(i)}]\,. \tag{B.22}$$

The matrix C is a contribution due to the cost functional J

$$C = 2\gamma_4\left[\int_0^T\Omega(t)dt - A_\Omega^{\mathrm{d}}\right]\begin{pmatrix}\hat{h} & 0 & 0\\ 0 & -\hat{h} & 0\\ 0 & 0 & 0\end{pmatrix}. \tag{B.23}$$

The right hand side is a linear functional of $\tilde{y}$, and we use MCN to solve it. We can take the values of y from the forward equations since we use constant time steps, see Sec. B.1. The new time step is then given by

$$\tilde{y}^{n+1} - \frac{i\Delta t}{2}\Big[(A^\dagger + C)\tilde{y}^{n+1} + B\big(\tilde{y}^{n+1}\big)^* + \sum_{i=1}^k\langle u_1^{(i)}|\tilde{y}^{n+1}\rangle v_1^{(i)} + \sum_{i=1}^k\langle\tilde{y}^{n+1}|u_2^{(i)}\rangle v_2^{(i)}$$
$$+\sum_{i=1}^k Re\langle u_3^{(i)}|\tilde{y}^{n+1}\rangle v_3^{(i)}\Big] = \tilde{b}\,, \tag{B.24}$$

with

$$\tilde{b} = \tilde{y}^n + \frac{i\Delta t}{2}\Big[(A^\dagger + C)\tilde{y}^n + B(\tilde{y}^n)^* + \sum_{i=1}^k\langle u_1^{(i)}|\tilde{y}^n\rangle v_1^{(i)} + \sum_{i=1}^k\langle\tilde{y}^n|u_2^{(i)}\rangle v_2^{(i)} + \sum_{i=1}^k Re\langle u_3^{(i)}|\tilde{y}^n\rangle v_3^{(i)}\Big]\,, \tag{B.25}$$

evaluated at $\bar{t}$. Eq. (B.24) is solved for $\tilde{y}^{n+1}$ using the complex extensions of the SMW formula, and is obtained from Eq. (B.12) with the replacements

$$A \to A^\dagger + C\,, \quad U_l \leftrightarrow V_l\,, \quad \Delta t \to -\Delta t\,. \tag{B.26}$$

Since the optimality system is highly complex, it is very efficient to employ the following criterion to check the numerical implementation. Taking Eq. (5.11), we can evaluate the left hand side by finite differences at the point λ for the test function $\delta\lambda$, while the right hand side is evaluated taking the numerically calculated gradient $\nabla\hat{J}$. If it converges at several points λ,

$$\lim_{\epsilon\to 0}([J(\lambda+\epsilon\delta\lambda) - J(\lambda-\epsilon\delta\lambda)]/(2\epsilon) = (\nabla\hat{J}_X, \delta\lambda)_X\,, \tag{B.27}$$

where X is the actual function space, the gradient is of reasonable numerical quality. We observed that the mismatch between left and right hand sides can be made as small as $10^{-4} - 10^{-3}$. Whenever this holds, we found the optimization to proceed until convergence.

B.3 Expressions for the involved matrices and vectors

We give the matrices A and B and vectors $v_l^{(i)}$ and $u_l^{(i)}$ used above. In the following, a bar denotes mean value between old and new time step. The MCTDHB(2) orbitals are denoted as ϕ_1 and ϕ_2. A bar denotes mean value of old and new time steps (or the iterative approximate solution to it in case of the Newton's equations). The sparse matrices are given by (with "0" having either dimensions of the orbitals, or the state vector, according to the context)

$$A = \begin{pmatrix} \hat{H}_{11} & \hat{H}_{12} & 0 \\ \hat{H}_{21} & \hat{H}_{22} & 0 \\ 0 & 0 & \mathbf{H}(\bar{t}, \bar{\phi}_1, \bar{\phi}_2) \end{pmatrix}, \quad \text{and} \quad B = \begin{pmatrix} \tilde{H}_{11} & \tilde{H}_{12} & 0 \\ \tilde{H}_{21} & \tilde{H}_{22} & 0 \\ 0 & 0 & 0 \end{pmatrix}, \tag{B.28}$$

where $\mathbf{H}$ is the two-mode Hamiltonian from Chap. A (see Eq. (A.3)). The vectors are given as

$v_l^{(i)}$	$i=1$	$i=2$	$i=3$	$i=4$
$l=1$	$\breve{H}_{11}^\dagger\bar{\phi}_1$ $\breve{H}_{12}^\dagger\bar{\phi}_1$ 0	$\breve{H}_{11}^\dagger\bar{\phi}_2$ $\breve{H}_{12}^\dagger\bar{\phi}_2$ 0	$\breve{H}_{21}^\dagger\bar{\phi}_1$ $\breve{H}_{22}^\dagger\bar{\phi}_1$ 0	$\breve{H}_{21}^\dagger\bar{\phi}_2$ $\breve{H}_{22}^\dagger\bar{\phi}_2$ 0
$l=2$	$L_1 + \tilde{H}_{11}\bar{\phi}_1^*$ $\tilde{H}_{12}\bar{\phi}_1^*$ 0	$\tilde{H}_{11}\bar{\phi}_2^*$ $L_1 + \tilde{H}_{12}\bar{\phi}_2^*$ 0	$L_2 + \tilde{H}_{21}\bar{\phi}_1^*$ $\tilde{H}_{22}\bar{\phi}_1^*$ 0	$\tilde{H}_{21}\bar{\phi}_2^*$ $L_2 + \tilde{H}_{22}\bar{\phi}_2^*$ 0
$l=3$	0 0 $2K_1\bar{\mathbf{C}}$	0 0 $2K_2\bar{\mathbf{C}}$	0 0 $2K_4\bar{\mathbf{C}}$	0 0 $2K_5\bar{\mathbf{C}}$

$v_l^{(i)}$	$i=5$	$i=6$	$i=7$	$i=8$
$l=1$	$\begin{matrix}0\\2\bar{\phi}_1^2\bar{\phi}_2^*\\0\end{matrix}$	$\begin{matrix}2\bar{\phi}_2^2\bar{\phi}_1^*\\0\\0\end{matrix}$	$\begin{matrix}0\\0\\K_3^\dagger\bar{\mathbf{C}}\end{matrix}$	$\begin{matrix}0\\0\\K_6^\dagger\bar{\mathbf{C}}\end{matrix}$
$l=2$	$\begin{matrix}2\bar{\phi}_2^2\bar{\phi}_1^*\\0\\0\end{matrix}$	$\begin{matrix}0\\2\bar{\phi}_1^2\bar{\phi}_2^*\\0\end{matrix}$	$\begin{matrix}0\\0\\K_3\bar{\mathbf{C}}\end{matrix}$	$\begin{matrix}0\\0\\K_6\bar{\mathbf{C}}\end{matrix}$
$l=3$	$\begin{matrix}2\hat{h}(x,\bar{t})\bar{\phi}_1\\-2\hat{h}(x,\bar{t})\bar{\phi}_2\\0\end{matrix}$	$\begin{matrix}4\lvert\bar{\phi}_1\rvert^2\bar{\phi}_1\\0\\0\end{matrix}$	$\begin{matrix}4\lvert\bar{\phi}_2\rvert^2\bar{\phi}_1\\4\lvert\bar{\phi}_1\rvert^2\bar{\phi}_2\\0\end{matrix}$	$\begin{matrix}0\\4\lvert\bar{\phi}_2\rvert^2\bar{\phi}_2\\0\end{matrix}$

$u_l^{(i)}$	$i=1$	$i=2$	$i=3$	$i=4$
$l=1,2$	$\begin{matrix}-\bar{\phi}_1\\0\\0\end{matrix}$	$\begin{matrix}-\bar{\phi}_2\\0\\0\end{matrix}$	$\begin{matrix}0\\-\bar{\phi}_1\\0\end{matrix}$	$\begin{matrix}0\\-\bar{\phi}_2\\0\end{matrix}$
$l=3$	$\begin{matrix}\tilde{\phi}_1\\0\\0\end{matrix}$	$\begin{matrix}\tilde{\phi}_2\\0\\0\end{matrix}$	$\begin{matrix}0\\\tilde{\phi}_4\\0\end{matrix}$	$\begin{matrix}0\\\tilde{\phi}_5\\0\end{matrix}$

$u_l^{(i)}$	$i=5$	$i=6$	$i=7$	$i=8$
$l=1,2$	$\begin{matrix}0\\0\\(U_0/2)\hat{a}_1^{\dagger,2}\hat{a}_2^2\bar{\mathbf{C}}\end{matrix}$	$\begin{matrix}0\\0\\(U_0/2)\hat{a}_2^{\dagger,2}\hat{a}_1^2\bar{\mathbf{C}}\end{matrix}$	$\begin{matrix}\tilde{\phi}_3\\0\\0\end{matrix}$	$\begin{matrix}0\\\tilde{\phi}_6\\0\end{matrix}$
$l=3$	$\begin{matrix}0\\0\\\hat{J}_x\bar{\mathbf{C}}\end{matrix}$	$\begin{matrix}0\\0\\(U_0/2)\hat{a}_1^{\dagger,2}\hat{a}_1^2\bar{\mathbf{C}}\end{matrix}$	$\begin{matrix}0\\0\\(U_0/2)\hat{a}_1^\dagger a_2^\dagger\hat{a}_1\hat{a}_2\bar{\mathbf{C}}\end{matrix}$	$\begin{matrix}0\\0\\(U_0/2)\hat{a}_2^{\dagger,2}\hat{a}_2^2\bar{\mathbf{C}}\end{matrix}$

Hereby, the columns denote the corresponding vectors and we omitted the brackets. We use the following definitions:

$\hat{H}_{ij}$	$\breve{H}_{ij} - (\bar{\phi}_j, L_i)1$
$\breve{H}_{ii}$	$\hat{h}(x,\bar{t}) + 2\bar{g}_1^{(i)}\lvert\bar{\phi}_i\rvert^2 + 2\bar{g}_2^{(i)}\lvert\bar{\phi}_j\rvert^2$, and $i \neq j$
$\breve{H}_{ij}$	$\bar{g}_2^i\bar{\phi}_{(i)}\bar{\phi}_j{}^* + 2\bar{g}_3^{(i)}\bar{\phi}_j\bar{\phi}_i{}^*$
L_i	$\hat{h}(x,\bar{t})\bar{\phi}_i + (\bar{g}_1^{(i)}\lvert\bar{\phi}_i\rvert^2 + 2\bar{g}_2^{(i)}\lvert\bar{\phi}_j\rvert^2)\bar{\phi}_i + \bar{g}_3^i\bar{\phi}_i^*\bar{\phi}_j^2$
$\tilde{H}_{ii}$	$\bar{g}_1^{(i)}\bar{\phi}_i^2 + \bar{g}_3^{(i)}\bar{\phi}_j^2$, and $i \neq j$
$\tilde{H}_{ij}$	$2\bar{g}_2^{(i)}\bar{\phi}_i\bar{\phi}_j$

where $i = 1, 2$, $j = 1, 2$. We further have

$\tilde{\phi}_1$	$\tilde{\phi}_2$	$\tilde{\phi}_3$	$\tilde{\phi}_4$	$\tilde{\phi}_5$	$\tilde{\phi}_6$
$\hat{\bar{\mathbf{P}}}\lvert\bar{\phi}_1\rvert^2\bar{\phi}_1$	$\hat{\bar{\mathbf{P}}}\lvert\bar{\phi}_2\rvert^2\bar{\phi}_1$	$\hat{\bar{\mathbf{P}}}\bar{\phi}_2^2\bar{\phi}_1^*$	$\hat{\bar{\mathbf{P}}}\lvert\bar{\phi}_2\rvert^2\bar{\phi}_2$	$\hat{\bar{\mathbf{P}}}\lvert\bar{\phi}_1\rvert^2\bar{\phi}_2$	$\hat{\bar{\mathbf{P}}}\bar{\phi}_1^2\bar{\phi}_2^*$

$\hat{\bar{\mathbf{P}}}$ denotes the projector with respect to the mean orbitals $\bar{\phi}_1$ and $\bar{\phi}_2$.

K_1	$(U_0\hat{a}_1^{\dagger,2}\hat{a}_1^2 - \hat{a}_1^\dagger\hat{a}_1\bar{g}_1^{(1)})/\bar{\rho}_{11}$
K_2	$(2U_0\hat{a}_1^\dagger\hat{a}_2^\dagger a_1 a_2 - \hat{a}_1^\dagger\hat{a}_1\bar{g}_2^{(1)})/\bar{\rho}_{11}$
K_3	$(U_0\hat{a}_1^{\dagger,2}\hat{a}_2^2 - \hat{a}_1^\dagger\hat{a}_1\bar{g}_3^{(1)})/\bar{\rho}_{11}$
K_4	$(U_0\hat{a}_2^{\dagger,2}\hat{a}_2^2 - \hat{a}_2^\dagger\hat{a}_2\bar{g}_1^{(2)})/\bar{\rho}_{22}$
K_5	$(2U_0\hat{a}_1^\dagger\hat{a}_2^\dagger a_1 a_2 - \hat{a}_2^\dagger\hat{a}_2\bar{g}_2^{(2)})/\bar{\rho}_{22}$
K_6	$(U_0\hat{a}_2^{\dagger,2}\hat{a}_1^2 - \hat{a}_2^\dagger\hat{a}_2\bar{g}_3^{(2)})/\bar{\rho}_{22}$

depends on the densities (evaluated at $\bar{\mathbf{C}}$), as well as on the coefficients

$$\begin{aligned}
&\bar{g}_1^{(1)} = U_0\big(\bar{\rho}_{11}\big)^{-1}\bar{\rho}_{1111}\,, \quad \bar{g}_2^{(1)} = U_0\big(\bar{\rho}_{11}\big)^{-1}\bar{\rho}_{1212}\,, \quad \bar{g}_3^{(1)} = U_0\big(\bar{\rho}_{11}\big)^{-1}\bar{\rho}_{1122}\,,\\
&\bar{g}_1^{(2)} = U_0\big(\bar{\rho}_{22}\big)^{-1}\bar{\rho}_{2222}\,, \quad \bar{g}_2^{(2)} = U_0\big(\bar{\rho}_{22}\big)^{-1}\bar{\rho}_{1212}\,, \quad \bar{g}_3^{(2)} = U_0\big(\bar{\rho}_{22}\big)^{-1}\bar{\rho}_{2211}\,.
\end{aligned} \tag{B.29}$$

We finally have

$$b = \begin{pmatrix} 2(\phi_1^0 - \bar{\phi}_1) - i\Delta t\hat{\bar{\mathbf{P}}}L_1 \\ 2(\phi_2^0 - \bar{\phi}_2) - i\Delta t\hat{\bar{\mathbf{P}}}L_2 \\ 2(\mathbf{C}^0 - \bar{\mathbf{C}}) - i\Delta t\mathbf{H}(\bar{t}, \bar{\phi}_1, \bar{\phi}_2)\bar{\mathbf{C}} \end{pmatrix}. \tag{B.30}$$

Acknowledgements

I am grateful to my supervisor Ulrich Hohenester for all I could learn from him during the last three years. His physical intuition has been very helpful in many difficult situations. Essential input to this work is due to Jörg Schmiedmayer. I thank him for providing the link of this work to experiments. At many visits at the Atominstitut I experienced great hospitality and very stimulating discussions. I thank Greg von Winckel and Armin Scrinzi for very fruitful collaborations. I wish to thank Augusto Smerzi for facilitating research stays at the INO-CNR BEC center in Trento, and for the warm hospitality. Furthermore, I would like to thank Thorsten Schumm, Ofir Alon, Alexej Streltsov, Igor Mazets, Jan Chwedeńczuk, and Francesco Piazza for most helpful discussions. Special thank goes to Anna for her love and support in busy times.